BRNO UNIVERSITY OF TECHNOLOGY
VYSOKÉ UČENÍ TECHNICKÉ V BRNĚ

FACULTY OF ELECTRICAL ENGINEERING AND COMMUNICATION
FAKULTA ELEKTROTECHNIKY
A KOMUNIKAČNÍCH TECHNOLOGIÍ

DEPARTMENT OF BIOMEDICAL ENGINEERING
ÚSTAV BIOMEDICÍNSKÉHO INŽENÝRSTVÍ

ANALYSIS OF ITERATIVELY RECONSTRUCTED CT DATA: NOVEL METHODS FOR MEASURING IMAGE QUALITY
ANALÝZA ITERATIVNĚ REKONSTRUOVANÝCH CT DAT: NOVÉ METODY PRO MĚŘENÍ OBRAZOVÉ KVALITY

DOCTORAL THESIS
DIZERTAČNÍ PRÁCE

AUTHOR
AUTOR PRÁCE

Ing. Petr Walek

SUPERVISOR
ŠKOLITEL

prof. Ing. Jiří Jan, CSc.

BRNO 2017

ABSTRACT

The collective dose from medical radiation has been sharply increasing as well as availability of CT scanners and increasing number of indicated pathologies. Hence, reduction of applied dose is a topical theme nowadays. A great progress has been made by introduction of novel iterative methods for reconstruction of image data from measured projections. A new interest and need for CT image quality measurement have been simultaneously reported. Quality of iteratively reconstructed data was so far quantitatively measured in phantom scans or in small regions of interest in real patient data. However, the character of iteratively reconstructed data suggest that those approaches are no longer sufficient and they need to be revised or replaced by a new ones. Design of novel CT image quality parameters which will respect specifics of iteratively reconstructed data and will be fully automatically computed directly from real patient data is the main objective of this thesis.

KEYWORDS

X-ray CT imaging, image quality, iterative reconstruction, noise power spectrum.

ABSTRAKT

Se zvyšující se dostupností medicínského CT vyšetření a s rostoucím počtem patologických stavů, pro které je indikováno, se redukce pacientské dávky ionizujícího záření stává stále aktuálnějším tématem. Výrazný pokrok v tomto odvětví představují nové metody rekonstrukce obrazů z projekcí, tzv. moderní iterativní rekonstrukční metody. Zároveň se zavedením těchto metod vzrostla potřeba pro měření obrazové kvality. Kvalita iterativně rekonstruovaných dat byla doposud kvantitativně hodnocena pouze na fantomových datech nebo na malých oblastech zájmu v reálných pacientských datech. Charakter iterativně rekonstruovaných dat však naznačuje, že tyto přístupy nadále nejsou dostatečné a je nutné je nahradit přístupy novými. Hlavním cílem této dizertační práce je navrhnout nové přístupy k měření kvality CT obrazových dat, které budou respektovat specifika iterativně rekonstruovaných obrazů a budou počítána plně automaticky přímo z reálných pacientských dat.

KLÍČOVÁ SLOVA

Rentgenová výpočetní tomografie, obrazová kvalita, iterativní rekonstrukce, šumové výkonové spektrum.

WALEK, Petr *Analysis of iteratively reconstructed CT data: novel methods for measuring image quality*: doctoral thesis. Brno: Brno University of Technology, Faculty of Electrical Engineering and Communication, Department of Biomedical Engineering, 2017. 120 p. Supervised by prof. Ing. Jiří Jan, CSc.

PROHLÁŠENÍ

Prohlašuji, že svou doktorskou práci na téma „Analysis of iteratively reconstructed CT data: novel methods for measuring image quality“ jsem vypracoval samostatně pod vedením vedoucího doktorské práce a s použitím odborné literatury a dalších informačních zdrojů, které jsou všechny citovány v práci a uvedeny v seznamu literatury na konci práce.

Jako autor uvedené doktorské práce dále prohlašuji, že v souvislosti s vytvořením této doktorské práce jsem neporušil autorská práva třetích osob, zejména jsem nezasáhl nedovoleným způsobem do cizích autorských práv osobnostních a/nebo majetkových a jsem si plně vědom následků porušení ustanovení § 11 a následujících autorského zákona č. 121/2000 Sb., o právu autorském, o právech souvisejících s právem autorským a o změně některých zákonů (autorský zákon), ve znění pozdějších předpisů, včetně možných trestněprávních důsledků vyplývajících z ustanovení části druhé, hlavy VI. díl 4 Trestního zákoníku č. 40/2009 Sb.

Brno ....

(podpis autora)

PODĚKOVÁNÍ

V první řadě patří mé poděkování školiteli Jiřímu Janovi, za vedení, odborné rady a řadu podnětů k mé práci. Dále bych rád poděkoval Petru Ouředníčkovi za rady a podněty jak z oblasti medicínské, tak technické. Zejména pak za poskytnutí možnosti pracovat s prototypy obou rekonstruktorů. Poděkování patří také celému osazenstvu CT oddělení Dětské nemocnice v Brně, za toleranci a poskytnutí možnosti sbírat data při rutinním provozu, zejména pak Tomáši Jatelovi, Ivě Červinkové, Igoru Jírovi a Jarmile Skotákové. Na závěr bych chtěl poděkovat rodině, přátelům, kolegům z UBMI a hlavně své manželce Petře za neustálou podporu a nekonečnou trpělivost. Speciální poděkování patří mému synovi Viktorovi, který odložil růst svých prvních zubů do doby, než bude má dizertační práce hotová.
Díky moc! Bez Váší pomoci by tato práce nemohla vzniknout.

Brno ....

(podpis autora)

TABLE OF CONTENTS

LIST OF FIGURES

LIST OF TABLES

LIST OF ABBREVIATIONS

CT X-ray computed tomography

ALARA As low as reasonably achievable

iDose^4 Iterative reconstruction technique developed by Philips healthcare

FBP Filtered back projection

IMR Iterative reconstruction technique developed by Philips healthcare

NPS Noise power spectrum

HU Hounsfield units

PSF Points spread function

MTF Modulation transformation function

ASIR Adaptive statistical iterative reconstruction developed by GE Healthcare

IRIS Image reconstruction in image space developed by Siemens

SAFIRE Sinogram affirmed iterative re- construction developed by Siemens

ADMIRE Advanced modeled iterative reconstruction developed by Siemens

AIDR Adaptive iterative dose reduction developed by Toshiba

MBIR Model-based iterative reconstruction developed by GE Healthcare

ID30 iDose^4 reconstruction method with level 30

ID50 iDose^4 reconstruction method with level 50

ID70 iDose^4 reconstruction method with level 70

L1BR Body routine level 1 IMR reconstruction method

L2BR Body routine level 2 IMR reconstruction method

L2BSP Body sharp plus level 2 IMR reconstruction method

SE Structuring element

POC Phase only correlation

GDD Gradient optimization with adaptive step size

CRS Controlled random search global optimization

DFT Discrete Fourier transform

CWT Continuous wavelet transform

ROI Region of interest

CoG Center of gravity

SIE Segmentation introduced error

SAW Spatially adaptive windowing function

MAT Medial axis transform

MSLL Maximum side lobe level

INTRODUCTION

The collective dose from medical radiation has been sharply increasing. As of 2009, there had been a sevenfold increase as compared to 1980 (according to the United States' National Council on Radiation Protection and Measurements). This trend has also been recorded in the Czech Republic, albeit not as markedly as in the U.S. Irradiation of the population from computed tomography (CT) examinations is increasing and comprises approximately 30% of the radiation burden from all radiodiagnostic methods [14]. The average dose from medical irradiation in the Czech Republic is 1 mili-Sievert (mSv) per year [127], which can be considered a high value in comparison with the annual dose received from natural sources (2.5 mSv).

In order to be compliant with the ALARA (as low as reasonably achievable) principle, each of the major CT manufacturers have focused their research on as large radiation dose reduction as possible. As a result of this increased effort, many new strategies for reducing radiation dose have been introduced, for example tube current modulation (in both angular and longitudinal directions), elimination of overranging effect, dual energy scanning, bowtie filtering and replacement of filtered back projection (FBP) by modern iterative algorithms for reconstruction of image data from measured set of projections [72], [31]. Among a range of mentioned dose reduction methods the iterative reconstruction takes an exceptional position by producing high quality images, even when drastic radiation dose reduction (up to 70%) is applied [22]. Such a dose reduction is allowed by inclusion of photon counting statistics and models of acquisition process into a reconstruction.

Introduction of novel iterative reconstruction methods attracted new attention to measurement of CT image quality which is needed for their comparison with FBP. Many studies dealing with problem of image quality evaluation of iteratively reconstructed images have been proposed recently. These studies are targeted either to assessment of image quality in small regions of interest in real patient data [69] or to evaluation of images acquired by scanning of phantoms [77]. Both approaches are suboptimal even for data reconstructed by FBP. The former approach utilizes information only from very spatially limited range of a data and the phantom approach analyzes noise properties in homogeneous regions of artificial images and there is difficulty to relate obtained results to clinical practice. Moreover, novel iterative reconstruction methods are generally nonlinear which, for example, causes that noise in iteratively reconstructed data is, according to [101] and [102], object dependent (i.e. its characteristics depend on density of imaged tissue). This effect can not be observed in data reconstructed by FBP. Evaluation of noise properties in homogeneous parts of water filled phantom is, hence, unable to capture whole complexity of noise in real patient data reconstructed by iterative methods. The main objective

this thesis is, thus, to design novel fully automatic approaches for measuring image quality which will be more convenient for iteratively reconstructed data.

Research presented in this thesis results from cooperation among Philips Healthcare, Brno Faculty Hospital, Children's Hospital and Department of Biomedical Engineering, Brno University of Technology. As already mentioned, all main CT vendors, including Philips Healthcare company, introduces their own algorithms for modern iterative reconstruction. Two iterative reconstruction methods were developed by Philips company; first statistical iterative method is called iDose^4 and second model based iterative reconstruction is called IMR. Prototypes of both reconstructors were lend to the Children's Hospital for long time data acquisition and early (prior to introduction of both methods to the market) image quality evaluation. The data acquisition undertaken during aforementioned cooperation, as well as objective and subjective evaluation of image quality, can be divided into two stages. In the first stage (within this thesis called "The iDose^4 project") a prototype of iDose^4 were available and a large set of 207 scans were acquired (detailed description of acquired data set can be found in Sec. 2). Quality of the acquired data were evaluated both subjectively (results of subjective medical evaluation were published in [50]) and objectively as described in this thesis.

According to information provided by the vendor, iDose^4 significantly reduces image artifacts and noise, which results in possibility to reduce applied dose up to 80% with image quality comparable with the quality of full dose FBP reconstruction. A standard deviation of image noise, as its basic measure, is used for initial comparison of iteratively and by FBP reconstructed data in Sec. 4.2. Based on phantom measurements, it is also declared that iDose^4 do not significantly alter noise texture (which is determined by noise frequency properties) and, thus, preserves natural look and feel of conventionally (i.e. by FBP) reconstructed images (radiologists are used to diagnose from images with FBP-like noise). In order to examine whether this positive attribute of iDose^4 applies also to real patient data, a methodology for estimation of noise frequency properties from real patient data and moreover from separate tissues is proposed. The second proposed image quality measurement, thus, compares frequency properties of noise in images reconstructed by FBP and iDose^4 and evaluates noise spectral shifts introduced by iterative reconstruction. The proposed methodology allows also comparison of frequency properties of noise which is typical for diverse tissues.

A data preprocessing necessary for "The iDose^4 project" is described in Sec. 3.1 and Sec. 3.2. Evaluation of noise in real patient data is problematic especially due to inability to fully automatically distinguish between anatomical structures and image noise patterns as it is possible in homogeneous parts of scanned phantoms. However, this problem is solved by subtraction of differently reconstructed data (the

fact that iDose^4 method influences only artifacts and image noise whereas anatomical structures remains mostly untouched is utilized) and by a method for determination of regions of dominant radiological noise in images resulting from the subtraction presented in Sec. 4.1. Spectral properties of radiological CT noise are routinely evaluated by one-dimensional noise power spectrum (1D NPS) calculated from square noise matrices. In order to be able to calculate 1D NPS in separate tissues its computation is adapted so that it can be estimated from non-square regions which inevitably increase errors caused by spectral leakage. A novel method for spectral leakage reduction in image data utilizing two-dimensional spatially adaptive weighting functions is, also, proposed in Sec. 4.3.4.1.

A prototype of IMR reconstructor was tested during the second phase within this thesis called "The IMR project". Again, a large set of patient data was acquired and their quality were evaluated objectively and also subjectively. Results of subjective medical evaluation of image quality were published in [14].

In contrast to iDose^4, IMR method is targeted not only to noise and artifact reduction, but is also able to improve spatial resolution and low-contrast resolution. Fidelity of anatomical structures reconstruction, thus, should be improved with respect to a data reconstructed by iDose^4 and FBP. An objective image quality assessment is, hence, targeted to evaluation of quality of anatomical structures reconstruction in real patient data. Anatomical structures in real patient data are not a priori known (as e.g. in phantoms for measuring of spatial resolution), evaluation of quality of their reconstruction is, thus, problematic due to lack of gold standard. Considering theoretical density of air in CT scans as -1000 Hounsfield units (HU), an exception may be represented by air filled structured like e.g. airways. The proposed criterion of quality of anatomical structures reconstruction is based on analysis of airways density. The closer the densities of airways are to the theoretical value the more quality the reconstruction is. 31 data sets acquired from thoracic body part were selected for this study and necessary lung and airways segmentation were performed which is described in Sec. 3.3. CT data reconstructed by diverse methods from a single set of projections are perfectly aligned and their direct comparison is not problematic. Problems arises when scans with different dose reduction (acquired immediately in succession, but there is always displacement e.g. by respiratory movements) have to be compared. Methods dealing with registration of CT lung data are, of course, available however an interpolation necessary for geometrical transforms may negatively influence results of the image quality assessment. A method which utilizes registration and allows comparison of corresponding airways voxels in both scans is proposed in Sec. 5.1. Results of data analyzes of the both stages are summarized in Sec. 6 and are discussed in Sec. 7

1 CURRENT STATE IN CT RECONSTRUCTION TECHNIQUES AND IMAGE QUALITY MEASUREMENT

The main goal of this thesis is to evaluate quality of data reconstructed by modern iterative methods not only in scanned phantoms (which is a standard approach), but in real patient data. The methods for CT image reconstruction (including modern iterative approaches) are briefly presented in Sec. 1.1. Parameters which represent crucial factors for determining CT image quality are described in Sec. 1.2 and standard approaches for measurement of those parameters in Sec. 1.3. An increased effort in measurement of CT image quality could have been recorded in literature (especially in terms of quality comparison of iteratively and by filtered back projection reconstructed data). The most interesting results are summarized in Sec. 1.4, where is also explained why must the methods for evaluation of CT image quality be revisited after introduction of iterative reconstruction methods.

1.1 Methods for reconstruction of CT tomographic images

As a CT scanner do not provide image data itself, a set of measured projections is given instead, it can be said that it provides Radon transform of an imaged object [48]. Algorithms for an image data reconstruction from a set of measured projections are, thus, an inevitable part of CT data acquisition.

Several different methods for CT image reconstruction methods have been used since their introduction to a clinical practice. Pure iterative reconstruction methods were used in the first CT scanners when low amount of data (128×128 reconstruction matrices) were acquired and relatively high computational requirements of iterative method were not critical. However, they started being impractical after introduction of fast high resolution CT scanners and were replaced by filtered back projection method. Thanks to rapid development of computational capacities in a last decade, algorithms for iterative reconstruction have re-emerged in CT imaging this time with possibilities to produce high quality images by incorporating various physical models into a reconstruction process [7].

A brief description of the aforementioned CT reconstruction methods is given; information sources of this chapter are [7], [10], [117] and [48]. Presented methods are divided, accordingly with [7], into filtered back projection and iterative methods, whereas iterative methods may be further divided into pure iterative methods

(without any modeling), statistical iterative methods (models of photons counting statistics are incorporated) and model based methods (which respects model of acquisition process). So far, each available modern iterative reconstruction is vendor specific and is produced as "black box" with none or very low amount of information about used algorithms. Description of the novel iterative reconstruction methods it thus limited to the amount of publicly available information.

Filtered back projection is an analytic method based on back projection (i.e. "smearing" one-dimensional projection over entire reconstruction matrix at the identical angle at which the projection was acquired). Each projection must be, prior to back projection, filtered by one-dimensional finite impulse response filter with frequency response $|\omega|$, where ω stands for spatial frequency, or its windowed versions (Shepp-Logan or Hamming). FBP is well known reconstruction method utilized in CT imaging for a long time, further details and formalisms are, thus, omitted.

In contrast to FBP, where a single reconstruction step is used, iterative methods use a repetitive approach whereas a better quality data should be provided in each repetition. Iterative reconstructions are based on algebraic expression of data acquisition process. Discretization of imaged scene is assumed, which is expressed as a set of samples $f_{i,k}$. Measured projections are, as well as projection angles, also discretized and individual samples are represented by detector responses. Projection samples in discrete environment are than, according to [48], given by

$$p_m = \sum_{n}^{N} w_{m,n} f_n \tag{1.1}$$

where $w_{m,n}$ is a weight given by an intersection of n-th voxel with m-th stripe connecting X-ray source with a detector area. Acquisition of complete set of projections is than described by a set of linear equations

$$\mathbf{Wf} = \mathbf{p}, \tag{1.2}$$

where $\mathbf{W}$ is a system matrix which describes acquisition geometry, $\mathbf{p}$ represents measured projections reformatted to a vector and $\mathbf{f}$ elements of image matrix reformatted to a vector. Using this algebraic expression, data can be reconstructed by solving a set of linear equations. Solution by standard methods would be, due to size of $\mathbf{W}$, extremely time consuming; moreover $\mathbf{W}$ is near-singular (i.e. some equations are close to linear dependence) and such systems are sensitive to errors on right hand side where a vector of measured projections (naturally burden by noise) is. Iterative procedures, such as Kaczmarz' method, are often used. Each equation in Eq. 1.2 represents a hyperplane in N-dimensional space of $\mathbf{f}$. In the ideal case, those hyperplanes are intersecting in a proper solution of reconstructed image and Kaczmarz' method iteratively seeks the intersection point. Kaczmarz' method have

an interpretation in terms of re-projection improvement. As **W** describes acquisition geometry, it can be also used to derive projection vector from an approximate solution in each repetition of an iterative process. The correction in each iteration is than calculated as a difference between projection of the object estimate and really measured projection. Each iteration step is, hence, composed of three major steps; a forward projection of an approximate solution provides estimate of projection, which is than compared with really measured projection producing correction term. Correction term is further modified in accordance with contained model and finally back projected on an object estimate. The iteration process may be initialized either by empty reconstruction matrix, matrix of constant gray level or by FBP reconstruction and finished when a predefined number of iterations is achieved or when update of a current object estimate is sufficiently small.

Difference among iterative methods (which influences quality of finally reconstructed data) lies in complexity of an incorporated model. Statistical methods incorporate counting statistics of detected photons as Poisson distributed. Model based methods, besides the counting statistics, incorporate models of an acquisition process. Models of acquisition process may be composed of many physical effects such as e.g. size of X-ray tube focal spot, size of detectors (which enables to simulate process of forward projection more precisely), polychromatic character of X-ray energy spectrum, X-ray tube anode heel effect, Compton and Rayleigh scattering or prior object information to exclude unrealistic results of reconstruction.

Described image reconstruction method iterates in raw data domain, however also methods which iterates in image data domain (denoising algorithms with preservation of spatial resolution using prior information about proton statistics are used) can be considered iterative reconstructions. Some methods (including iDose^4) iterate in both raw and image domains.

1.2 Quality of CT Images

Quality of CT images depends, as in majority of imaging tasks, on four fundamental factors: contrast, spatial resolution, image noise and artifacts. Combination of those factors determines visibility of details in CT scans and, thus, influences ability to set a correct medical diagnosis. The main advantage of CT scanners is ability to visualize low contrast structures, which is limited primarily by noise. CT noise is the crucial factor which influence image quality and is inevitably associated with radiation dose; the higher the radiation dose is, the lower magnitude of image noise is and detectability of low contrast objects is improved [30], [84]. The four factors fundamental for CT image quality will be briefly described in following chapters.

1.2.1 Noise in CT imaging

Provided that a perfectly homogeneous real world environment (such as phantom filled by water) is scanned, Hounsfield units in the resulting image will not be uniform but rather fluctuating around mean value of HU typical for water. Such random fluctuations are called CT radiological noise. CT radiological noise may origin as a result of simultaneous effect of quantum noise, structure noise, and electronic noise. Generally, it can be assumed that quantum noise is a dominant component of radiological noise in CT images. Quantum noise is proportional to a total count of X-ray photons contributing to the image creation. Statistical fluctuations of quantum noise are described by a Poisson distribution; a quantum noise level is, hence, given by $1/\sqrt{N}$ where N is a count of measured X-ray photons. Level of random variations caused by radiological noise can be, in the process of image formation, influenced by many factors which can affect the count of photons contributing to creation of each image voxel. According to [30] examples of those factors are X-ray tube current and voltage, rotation time of X-ray tube and slice thickness.

Authors in [96] showed that CT radiological noise is spatially correlated (i.e. random variations in one location is not independent on random variations in other locations). The spatial correlations are introduced by the reconstruction process, whereas noise in the detectors is assumed to be white. Spatial correlations may be evaluated either by autocorrelation function or, in accordance with Wiener-Khintchin theorem, noise power spectrum. Nonzero spatial correlations of radiological CT noise means that noise power spectrum is not uniform (uncorrelated white noise have uniform power spectrum). Shape of noise power spectrum envelope is an important image quality parameter as low frequency components of noise power spectral density, as shown in [37], influence detectability of wide area low contrast objects.

1.2.2 Artifacts in CT imaging

Artifacts may be, according to [30], defined as any structure that is seen on an image but is not representative of the actual anatomy. CT artifacts are able to obscure or, on the other hand, simulate pathology. CT artifact is a wide term which covers several different artifact types with different cause and impact to quality of final CT image. Most types of CT artifacts can be, according to their effect in image data, divided into three groups: shading artifact, streak artifact and ring artifact. Artifacts falling into a certain group may be caused by a different effects (e.g. streaking artifact may be caused by a presence of metal or by insufficient X-ray intensity). The most common types of CT artifacts are briefly described in following; the information contained in [30], [10], [6] and [124] is used in this summary.

Shading artifact: Shading artifact is mostly manifested as dark streaks between two high attenuating objects (typically bones or iodinated contrast). The major cause of shading artifact is beam hardening effect. As X-ray energy spectrum is not monochromatic (i.e. X-ray beam is composed of photons with range of energies), passing through attenuating object, low energy components are more attenuated than high energy ones. Mean beam energy increases which may result to different type of interactions with scanned object (a photoelectric effect is dominant at low and Compton scatter at high energies). Compton scatter changes photons directions, they, thus may be detected by a different detector than the one on a direct path. For highly attenuated X-ray beams (between two dense objects), beam hardening effect and Compton scatter cause (in some detectors) detection of more photons than expected, which results in dark streaks.

Ring artifact: If any of detectors is defective of mis-calibrated, it gives constantly erroneous signal resulting in circular artifact centered at a center of rotation.

Streak artifact: Streak artifact is manifested as periodically repeating lighter and darker streaks, which are able to seriously decrease image quality. Streak artifact may arise from many reasons, all of them are somehow connected with inconsistent detector measurements (i.e. discrepancies among HU in reconstructed CT images and a true tissue attenuation coefficients).

The main factor causing the inconsistencies is photon starvation, which may occur when X-ray beam passes highly attenuating structures such as shoulders producing noisy projections in the direction of high attenuation. In such cases, the reconstruction process tend to greatly magnify the noise which results in streaking artifact.

Inconsistency due to partial volume effect is caused by divergent character of X-ray beam. Identical structures are sampled twice during a full 360° scan. Thanks to cone-shaped X-ray beam, a small dense structure (i.e. bone edge) located out of rotation center may be partially present in a measurement and completely missed in the opposite one.

Patient's motion causes blurring or doubling of image edges as well as long range streaks, again, due to inconsistency of measurements.

Very severe streak artifacts are caused by presence of metal objects with density beyond the range that can be handled by the computer. Presence of the metal object cause beam hardening, partial volume effect and also Compton scatter. Hypothetically, if majority of photons on a direct path are stopped by the metal object, only scattered photons are detected, this produces measurements with poor signal to noise ratio which results in severe streak artifacts.

1.2.3 Spatial resolution of CT images

Spatial resolution is, according to [30], defined as ability to distinguish small closely spaced objects. Size and spacing of X-ray detectors as well as X-ray tube focal spot size are crucial factors affecting spatial resolution. Moreover, spatial resolution may be influenced by movement of an imaged object, size of reconstruction matrix and voxel size. Spatial resolution can also be influenced by a reconstruction algorithm e.g. by a choice of reconstruction filter type used in FBP algorithm.

1.2.4 CT image contrast

Contrast in CT images depends on differences in absorption of X-rays in different tissues types, which results in differences in intensity of X-rays interacting with the detectors. CT image contrast is represented by CT contrast scale; the measured attenuation coefficients are transformed into CT numbers (in Hounsfiend units [HU]) according to

$$\text{CT numbers} = 1000 \times \frac{\mu_p - \mu_w}{\mu_w} \qquad [HU], \tag{1.3}$$

where μ_p and μ_w are attenuation coefficients for a given tissue and water, respectively [30].

1.3 Measuring of CT image quality

CT image quality (in terms of aforementioned image quality parameters) have to be somehow measured if quality of data, e.g. acquired by different scanners or reconstructed by diverse methods, have to be compared. Measuring image quality in terms of spatial resolution and image contrast are often performed by scanning and evaluation of test objects (mostly specific phantoms dedicated for measurement of image quality).

Achievable spatial resolution is practically evaluated by parameters PSF (Point Spread Function) or its spectral domain counterpart MTF (Modulation Transformation Function). Modulation transformation function express ability to transfer contrast of individual spatial frequencies from real world to a reconstructed CT image. Calculation of MTF is possible either by evaluation of scanned phantom which contains group of testing metal strips with several widths and spacings, such as in [32], or by scans of thin wire (model of Dirac delta function) situated in center of gantry rotation which produce measurement of PSF.

Contrast resolution is evaluated by so called contrast-detail diagram which is graphical representation of dependence of limit recognizable contrast on a size of

imaged detail. Such diagrams are often measured using Rose-Burger phantom containing objects (circles or squares) situated in regular arrays of different contrast and sizes. Evaluation of Rose-Burger phantom scans are usually objective whereas observer defines lowest visible contrast at different sizes [70]. Due to many different types of CT image artifacts, their evaluation is, ordinarily, only subjective.

CT image quality in terms of image noise is often evaluated on scans of homogeneous (usually water filled) phantoms, where, thanks to a phantom's homogeneity, present fluctuations are supposed being results of radiological noise. Methods for measurement of radiological CT noise are well elaborated in the various literature sources and several basic approaches, which will be further utilized in this dissertation are described in following sections.

1.3.1 Standard deviation of radiological noise

Standard deviation calculated according to

$$\sigma = \sqrt{\frac{1}{N}\sum_{i=1}^{N}(x_i - \mu)^2}, \tag{1.4}$$

where N is count of evaluated voxels, x represents density of individual voxels and μ is mean calculated over considered spatial range, is a measure of magnitude of the fluctuations caused by radiological CT noise.

1.3.2 Radial 1D noise power spectrum

Even though standard deviation is a valuable measure of statistical noise in CT images, it provides information only about average magnitude of image noise. Noise frequency distribution is, however, very important parameter for detectability of low contrast objects and also for human perception. Information about noise frequency distribution may be obtained by computation of noise power spectrum (NPS) which utilizes Fourier transform to determine degree of randomness of radiological noise present at each discrete spatial frequency. Theoretical framework of NPS as well as its different analytical expressions were established in early works such as [96], [37], [21], [54]. Current approaches for NPS estimation are based on practical noise measurements, rather than on analytical expressions which would be very complicated for modern CT scanners. NPS may be calculated either by taking Fourier transform of autocorrelation function or taking Fourier transform of noise data and squaring absolute value of the result.

A latter frequency domain based direct digital method for computation of NPS presented in [98] and [121] and expressed as

$$\mathbf{S}(f_x, f_y) = \frac{b_x b_y}{L_x L_y} \cdot \left\langle \left| DFT_{2D} \left\{ \mathbf{D}(x,y) - \mathbf{D_{filt}}(x,y) \right\} \right|^2 \right\rangle \tag{1.5}$$

is used in this thesis. Each slice of a 3D noise matrix, which is considered to be one realization of a stochastic field (i.e. stochastic image), is denoted as $\mathbf{D}(x,y)$ and must be locally zero mean detrended prior to computation of NPS; hence subtraction of image filtered by a low pass Gaussian filter $\mathbf{D_{filt}}(x,y)$ is performed. The purpose of this operation is, according to [54], reduction of variations which are constant from realization to realization (e.g. insufficiently corrected beam hardening artifact). The individual power spectrum of a noise realization is computed by squaring absolute value of 2D Fourier transform of the detrended noise realization. As individual noise power spectra suffer from large fluctuations among realizations, power spectrum of the stochastic field (i.e. the process generating random noise) must be computed as mean value of individual noise power spectra (outlined by $\langle \circ \rangle$ operator). Normalization by sampling periods b_x, b_y and image sizes L_y, L_x in directions x and y, respectively, must be done to enable comparison of power spectra of different stochastic fields. 2D NPS computed according to Eq. 1.5 is a comprehensive descriptor of noise frequency distribution; nevertheless, it is complicated to evaluate or extract some descriptive parameters from it. Providing that 2D NPS is rotationally symmetric, spectral distribution can be expressed by radial one-dimensional noise power spectrum without any loss of information [8]. The radial 1D noise power spectrum is computed by angular averaging of 2D noise power spectrum and therefore is a function of the absolute spatial frequency

$$\omega = \sqrt{\omega_x^2 + \omega_y^2}. \tag{1.6}$$

Noise power spectrum is often used as a quality measure of CT imaging systems, such as in [11], [8], and represents base for further more complex CT image quality measurements such as noise equivalent quanta.

1.3.3 Noise equivalent quanta

Noise equivalent quanta is, according to [11] defined as the effective number of photons per unit length of the detector. Provided than noise power spectrum is expressed in attenuation coefficients, noise equivalent quanta is given by equation taken from [63]

$$NEQ(f) = \pi |f| \frac{MTF^2(f)}{NPS(f)}, \tag{1.7}$$

where f denotes absolute spatial frequency according to Eq. 1.6.

As stated in [11], noise power spectrum is a comprehensive evaluation of influence of reconstruction method to noise properties, whereas noise equivalent quanta describes influence of acquisition parameters. Hence, noise power spectrum has been chosen as a main parameter for evaluation of image quality in this thesis.

1.4 Specifics of quality measurement of iteratively reconstructed images

Introduction of iterative reconstruction methods attracted new attention and need for CT image quality measurement. A very large number of publications have been published since introduction of the modern iterative CT reconstructions which are dealing either with quality comparison among iteratively and by FBP reconstructed data, among model based and statistical iterative methods or among iterative methods provided by different vendors. As this thesis is primarily focused on development of novel methods for image quality assessment, published methodologies which are used for the quality evaluations are summarized rather than the results. Only findings which are immediately related to this thesis are mentioned.

Methodologies of published methods may be divided into two main groups; an evaluation of artificial phantoms images and an evaluation of real patient data. Typically, an evaluation in real patient data is objective and subjective, whereas an objective measurement is conducted in a relatively small subset of data (i.e. a region of interest manually selected inside an evaluated anatomical structure), where standard deviation of noise, signal to noise or contrast to noise ratios are measured. Using this approach, different iterative reconstruction methods have been compared with FBP method including ASIR (Adaptive Statistical Iterative Reconstruction developed by GE Healthcare) e.g in [69], [61], [95]; IRIS (Image Reconstruction in Image Space developed by Siemens) e.g in [87]; SAFIRE (Sinogram Affirmed Iterative Reconstruction developed by Siemens) e.g in [118], [81]; ADMIRE (Advanced Modeled Iterative Reconstruction developed by Siemens) e.g. in [33] [41]; AIDR (Adaptive Iterative Dose Reduction developed by Toshiba) e.g in [26], [52], iDose^4 (developed by Philips Healthcare) e.g in [43], [65], [4], [45] and MBIR (Model-Based Iterative Reconstruction developed by GE Healthcare) e.g. in [20]. Results of almost every such performed comparison shows that quality of iteratively reconstructed data is superior compared quality of by FBP reconstructed data.

Another approaches for image quality evaluations in real patient data are based on assessment of fidelity of anatomical structures (mostly structures located in lungs such as nodules or airways) reconstruction. Interactive measurement of bronchial lumen and wall area serve as quality measures for comparison of FBP and iDose^4

reconstructions in [75] (no statistically significant differences have been found for this specific image quality measure). Similarly, quality of CT lung scans reconstructed by FBP, ASIR and MBIR were compared by means of airways wall thickness in [17], whereas significant differences were, this time, found. Authors in [106] measured influence of an iterative method to performance of automatic algorithm for detection of pulmonary nodules (its sensitivity increased about 6.3% while FBP was replaced by SAFIRE). Porcine heart-lung explants mounted into dedicated thoracic phantom were scanned and reconstructed by FBP and SAFIRE in [62]. The maximum number of automatically detected airways segments, The most peripheral airways segment and airways wall thickness were used to compare both reconstructions. No relevant influence of iterative reconstruction was found.

A second group of approaches for iterative reconstruction methods performance measurements are based on evaluation of imaged phantoms. Compared to evaluation of a real patient data, advantage of phantom based approaches is that imaged scene is a priori known. This significantly ease their evaluation which may be, potentially, fully automated. One option is offered by anthropomorphic phantoms which are specially developed in order to simulate human tissues whereas density and locations of tissues of interest are known.

A phantom of vascular models with three different wall thicknesses was used in [107]. A quality parameter based on measurement of attenuation in center of vascular wall was used to compare quality of MBIR and FBP. Phantoms simulating chest and upper abdomen in [93] and liver in [71] were subjected to subjective quality evaluation. Dependence of a spatial resolution on contrast and dose levels was examined on thoracic section of a specialized pediatric phantom in [64]. Significant dependence were found in data reconstructed by MBIR whereas not in by FBP reconstructed data.

Various phantoms specialized on measurement of spatial resolution, noise, signal and contrast to noise ratios, CT numbers linearity and accuracy can be used for image quality evaluation of iteratively reconstructed data and for comparison with conventionally reconstructed ones such as in [29], [44].

This thesis is partly focused on evaluation of frequency shift of noise power spectra in iteratively reconstructed data (compared to noise power spectra in by FBP reconstructed data) in real patient data. Published findings resulting from similar analyzes performed on homogeneous phantoms are, thus, presented. Shift of a center of gravity of 1D NPS in iteratively reconstructed data towards lower spatial frequencies was reported in [29] for data reconstructed by IRIS method, in [69] and [90] for data reconstructed by ASIR method and in [100] for data reconstructed by ADMIRE method. On the other hand, noise data reconstructed by iDose^4 shows, according to results published in [24], nearly identical spectral properties as the noise

data reconstructed by FBP. This result was supported by [68] where six iterative methods were compared and the lowest modulation of noise power spectra were observed in data reconstructed by iDose^4.

Modern iterative reconstruction algorithms are nonlinear systems which are much more complicated than FBP method. Hence, some traditional (i.e. developed to evaluate quality of FBP reconstructed data) may not be further sufficient and needs to be revised. Authors in [101] showed on a set of homogeneous and textured phantoms that noise in iteratively reconstructed data is object dependent (i.e. its level is dependent on a density of imaged object) whereas this dependence can not be observed in conventionally reconstructed data. Identical results were later presented in [102] where scans of anthropomorphic phantoms were evaluated. Though still routinely used for image quality evaluation, noise power spectra calculated from homogeneous phantoms may not further be a proper representative of noise frequency properties in actual patient scans (for nonlinear reconstruction algorithms).

2 DESCRIPTION OF ACQUIRED DATA SETS

As already mentioned, data acquisition can be divided into two phases, whereas Philips Briliance 64-channel CT scanner was always used.

207 scans were acquired in the first phase, when a prototype of iDose^4 method was tested. Data were acquired from three main body parts (head, abdominal and thoracic) according to standard scanning protocols. 42 scans were acquired from head body part without reduction of applied dose and reconstructed by standard FBP algorithm and iDose^4 method with levels 30 (abbreviated as ID30), 50 (abbreviated as ID50) and 70 (abbreviated as ID70). iDose level defines percentage strength of iterative reconstruction in reduction of quantum noise. In the rest of cases (14 brain scans, 79 scans of thoracic body part and 72 scans of abdomen), each patient was scanned twice with doses reduced to 25 % and 75 % of regular dose according to a scanning protocol (dose reduction was performed by corresponding reduction of X-ray tube current). Each scan was, this time, reconstructed by FBP, ID30 and ID80. Patients' ages ranged from 1 month to 60 years; mean patients' age was 16.8 years. A set of 33 brain scans (nine scans were excluded because of inconsistent reconstructions) without dose reduction were selected for objective image quality evaluation.

A prototype of IMR (Iterative Model Reconstruction) was tested in the second phase. 50 native and post-contrast CT examinations of neck (2×), thorax (31×) and abdomen (17×) areas was performed with 80% dose. In 32 studies, this was followed by a series with the X-ray tube current reduced to a value ranging around 20% of the original value. Besides reduction of X-ray tube current, standard protocols were followed. CT scans were reconstructed using FBP, iDose^4 with level 5 (labeling of iDose^4 levels was different from the previously used prototype) and IMR with four different preselected levels (Body Routine Level 1 abbreviated as L1BR, Body Routine Level 2 abbreviated as L2BR and Body Sharp Plus Level 2 abbreviated as L2BSP). Acquired image studies was divided into three groups (Young - 10 studies, Preadolescent - 25 studies, Adult - 15 studies). The average ages in the individual groups were 4.45 months, 5.9 years, and 29.4 years, respectively. Patients' ages ranged from 0.5 month to 48 years.

3 DATA PREPROCESSING

An extensive preprocessing, which makes the real patient data quality assessment possible, was needed and is described in this section. Preprocessing necessary for the iDose[4] project can be divided into two main parts. Elimination of stair-step errors caused by defect of gantry tilt correction during the data acquisition, which is described in Sec. 3.1, is the first preprocessing step. A second step, necessary for evaluation of noise properties in diverse tissues, is segmentation of basic tissues in head CT data. The segmentation approach based on graph-cuts is presented in Sec. 3.2. Skull segmentation turns out to be problematic especially due to complicated structure of a cranial base with very weak cortical bone parts and densities of trabecular bone parts similar to densities of soft tissue. Several studies dealing with bones segmentation in CT images were published which mostly uses combinations or cascades of diverse image processing approaches. Some of the most interesting approaches are briefly described. A multi-step approach utilizing cascade of region growing method with locally adaptive threshold followed by boundary adjustment based on morphological operations and analysis of density profile perpendicular to the cortical bone part, was published in [53]. An iterative edge tracking method based on estimation and correction of seed points positions was published in [123]. An adaptive thresholding is used in [126]; five variants of active contour models are compared in [109]; approaches which uses registration of bone models are used in [119] and [104] and genetic algorithms are utilized in [49]. Approaches specialized to a segmentation of a skull in CT images were also recently published [28], [46], but none of them is specialized to a segmentation of a cranial base.

The proposed method for a skull segmentation (including a cranial base) is based on graph-cut algorithm similarly as in [59]. Graph-cut segmentation is followed by analysis of bones contours which results in detection and correction of mis-segmented cortical bones parts, see Sec. 3.2.1. Detection of mis-segmented bones locations is inspired by a method published in [114] where contour shape descriptors are used for validation of segmentation in CT image sequences. The last step, described in Sec. 3.2.2, is filling of closed objects which may represent either trabecular bone part or soft tissue (i.e. brain tissue surrounded by skull). A method which enables to distinguish between those two tissues types is, thus, proposed. Though filling of closed objects is used in several aforementioned publications (e.g. in [53]), this problem has not been addressed in any of them.

In order to be able to assess quality of different reconstruction methods via evaluation of quality of airways reconstruction (which is a main goal of the IMR project), the airways must be firstly segmented. Many methods dealing with problem of airways segmentation in CT data have been published so far. An online

challenge EXACT'09 was also organized in 2009, where ten fully automatic and five interactive airways segmentation methods were quantitatively compared and results were published in [67]. Quantitative comparison of the algorithms was based on evaluation of several parameters such as a count of detected branches, overall length of detected airways tree, leakage volume and false positive rate. Among methods participating in EXACT'09 the best results were obtained using approaches based on gradient vector flow, morphological-aggregative approach, tube detection filter and three variants of region growing (adaptive cylinder constrained region growing, adaptive region growing with histogram correction and centricity-based region growing). Besides segmentation approaches participating EXACT'09 other methods dealing with this problem were also published, the most interesting ones are briefly presented.

A method published in [91] is based on iterative thresholding (with gradually decreasing threshold) followed by a modeling of segmented anatomical structures by marching cube algorithm. Geometry of obtained models is subsequently evaluated by principal curvature calculation and regions which do not have tubular shape are removed. However, due to local curvature perturbations of some airways regions, false negative detections occur, which are subsequently corrected by a procedure called "puzzle game". A 3D region growing which utilizes information from a trained airways appearance model and vessel orientation similarity (a geometrical relation between airways and vessels are used) is presented in [66]. A method which selects and by fuzzy connectivity segments small cylindrical regions of interest and immediately analyzes segmentation result in order to prevent leaks to lung parenchyma is described in [110]. The method presented in [34] is composed of raw airways segmentation using region growing in 3D space, which if followed by four stages targeted to adding of thin peripheral airways (namely localization of airways cross-section locations, airways segments definitions, connection of the detected segments and global graph partitioning). Two airways enhancement methods were simultaneously used in [120] (gray-scale morphological reconstruction and multi-scale vesselness enhancement), which were than segmented using fuzzy connectedness method. Hessian analysis for enhancement of tube-like structures followed by an adaptive multi-scale cavity enhancement filter is used in [74]. A support vector machine is, subsequently, utilized to suppress false positive regions and final segmentation is obtained by a graph-cut method. A convolutional neural network based approach for leak detection have also been recently published in [15].

3.1 Data driven gantry tilt correction

During the iDose[4] prototype testing, it was found that the originally acquired CT images suffered from very severe errors, which were apparent after the three-dimensional reformation to sagittal plane. These errors are caused by the defect of gantry tilt correction during tilted multi-section scanning and are reflected as mutual misplacements of data sub-volumes. The width of misplaced sub-volumes (i.e. the count of its axial slices) corresponds to the number of slices acquired during a single gantry revolution and the magnitude of shift between sub-volumes is connected to the degree of gantry tilt. This specific kind of error is called stair-step error; it should not be confused with stair-step artifact appearing around the edges of anatomical structures when scanning with wide collimations and non-overlapping reconstruction intervals are used [6].

Image quality (in terms of image noise content and fidelity of anatomical structures reconstruction) is not affected, and data can be fully recovered (when neglecting interpolation errors) by precise registration of sub-volumes. The stair-step error may harm (or even make impossible) further data processing or noise analyzes. Therefore, a large set of a quite unique data might become lost. A sufficiently fast data driven[1] method for gantry tilt correction is thus needed.

Correction of stair-step error can be divided into two separate problems while the first is the detection of number of slices acquired on a single gantry revolution, which is described in Sec. 3.1.1 and the second, described in Sec. 3.1.2, is registration of misplaced sub-volumes. The term inter-slice variability is introduced and its measure, represented by the vector of Euclidean distance similarities between consecutive slices, is established. A mathematical morphology based method for the separation of peaks in the one-dimensional signal, which reflects the peaks' "significance", is also presented.

3.1.1 Detection of misplaced sub-volume's borders

The correction of stair-step error will be demonstrated on two testing images, scanned with a high (Fig. 3.1a) and low (Fig. 3.1b) degree of gantry tilt. A signal resulting from the calculation of Euclidean distance similarity measure Eq. 3.1 [48] between consecutive axial slices is used for the detection of misplaced sub-volume borders.

[1] Without any information about the width and magnitude of shift of sub-volumes, those parameters must be derived directly from image data.

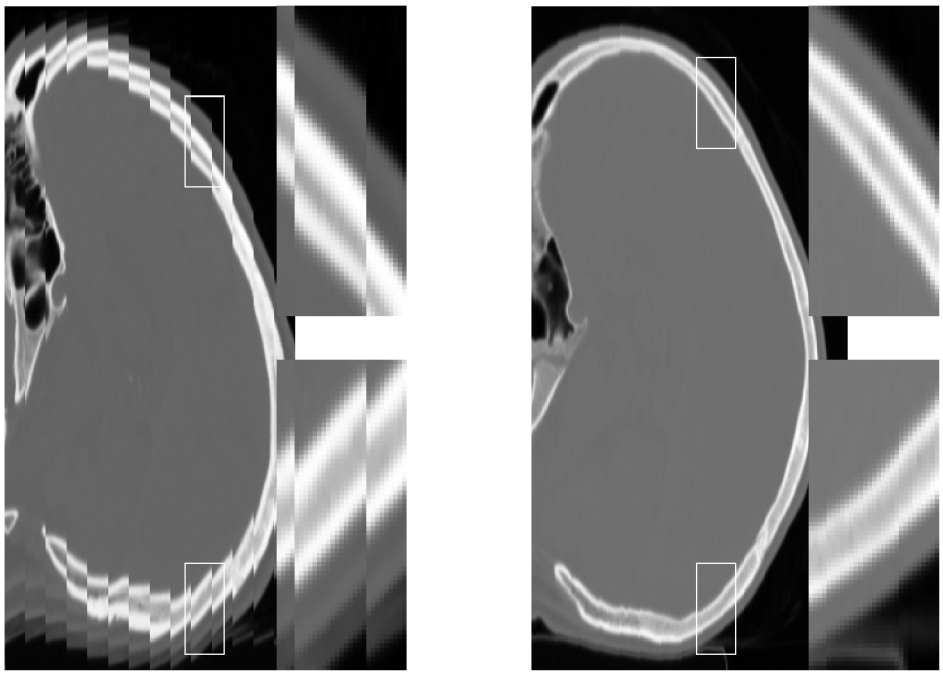

(a) (b)

Obr. 3.1: Demonstration of stair-step error on sagittal slices of two brain images (with magnified sections): (a) Brain scanned with a high degree of gantry tilt, (b) brain scanned with a low degree of gantry tilt.

The resulting function is called inter-slice variability (IV).

$$IV(\mathbf{a}, \mathbf{b}) = \sqrt{\sum_{i=0}^{N} (a_i - b_i)^2}. \tag{3.1}$$

Variables $\mathbf{a}$ and $\mathbf{b}$ in Eq. 3.1 mean pixel intensities rearranged to vectors and N is a count of pixels in the compared images. IV curves corresponding to the testing images Fig. 3.1a and Fig. 3.1b are depicted in Fig. 3.3b and Fig. 3.3c. The shift of sub-volumes is reflected as a sudden change of similarity between bordering slices that produces a sharp peak in IV function. The height of a peak depends on the amount of shift between the sub-volumes and thus on the degree of gantry tilt.

Detection of misplaced sub-volume borders is obviously an easy task in cases when the degree of gantry tilt is relatively high, like in Fig. 3.3b. On the contrary, when the gantry tilt is low, the magnitude of peaks caused by the shift of sub-volumes is comparable with the height of some peaks caused by anatomical variability[2], which makes its detection much more challenging. The problem is demonstrated on two

[2]The term "anatomical variability" is understood to be a degree of dissimilarity between consecutive slices caused by changes inherent to human anatomy.

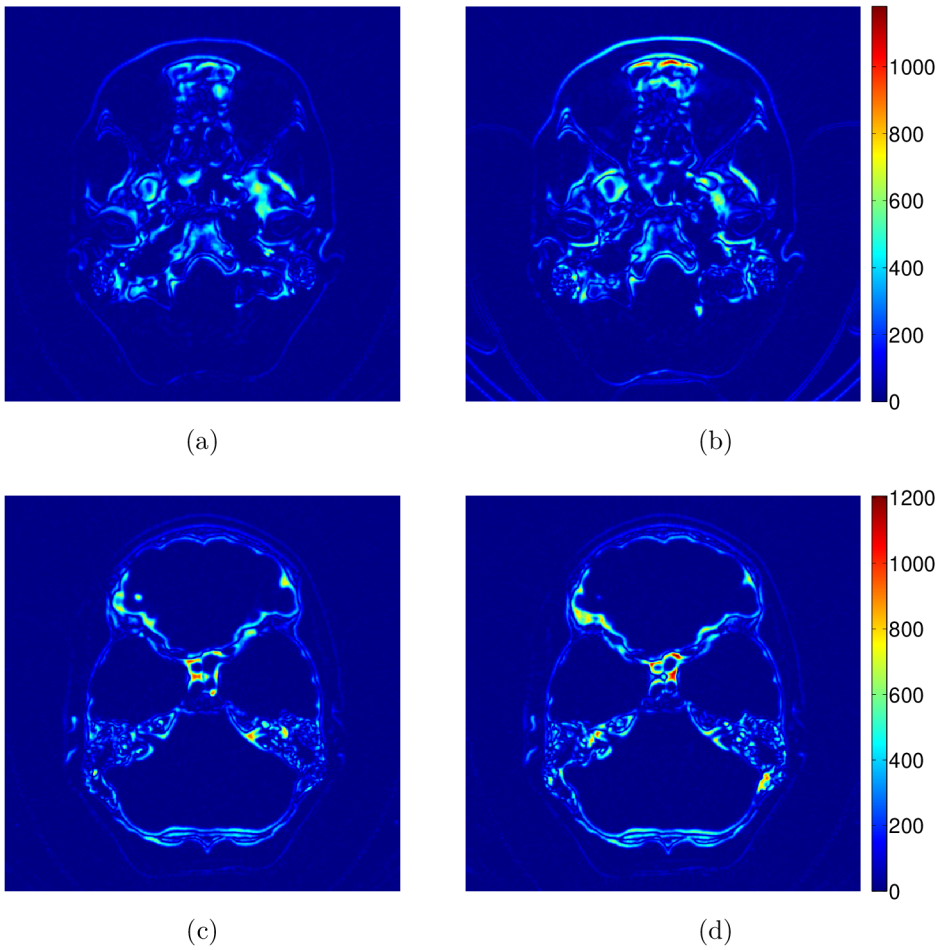

Obr. 3.2: Exploration of the source of two peaks in inter-slice variability function with similar heights. Images show the absolute values of differences between consecutive slices of data in Fig. 3.1b that are forming edges of peaks between the 15^{th} (a) and 16^{th} (b), 40^{th} (c) and 41^{st} (d) elements. Dissimilarities forming the peak between the 15^{th} and 16^{th} elements are caused by a combination of anatomical variability and a slight horizontal shift (see the higher values of differences at the borders of the head and patient's table in (b)); on the contrary, dissimilarities forming the peak between the 40^{th} and 41^{st} elements are caused only by anatomical variability.

manually selected pairs of elements of IV curve Fig. 3.3c (15^{th}, 16^{th} and 40^{th}, 41^{st}), which form the edges of two peaks with comparable heights. In order to reveal the source of the peaks' creation, absolute values of differences between consecutive slices are visualized in Fig. 3.2. The parameters of creation of the individual subimages are summarized in Tab. 3.1. Here, the parameters, for example in the first row, express that Fig. 3.2a represents the absolute value of difference between slices 14 and 15 of the original data, and their Euclidean distance similarity $(1, 79.10^9)$

creates the 15^{th} element of IV function.

Tab. 3.1: Specification of the parameters of individual sub-images of Fig. 3.2.

Figure no.	Slice no.	Element of IV no.	Euclid dist.
Fig. 3.2a	14 and 15	15^{th}	$1.79 \cdot 10^9$
Fig. 3.2b	15 and 16	16^{th}	$2.65 \cdot 10^9$
Fig. 3.2c	39 and 40	40^{th}	$2.38 \cdot 10^9$
Fig. 3.2d	40 and 41	41^{st}	$1.69 \cdot 10^9$

Comparing sub-images of Fig. 3.2, it is evident that a sudden change in the IV function between the 40^{th} and 41^{st} elements is only caused by anatomical changes between slices 39, 40 and 41. On the contrary, a sudden change situated between the 15^{th} and 16^{th} elements is caused by a combination of a slight horizontal shift between slices 15 and 16 (notice the high values of differences situated around the borders of the patient table in Fig. 3.2b, whereas patient table is completely subtracted in other images) and anatomical variability.

The detection of misplaced sub-volumes' borders is divided into three main steps. Firstly, peaks (both caused by anatomical variability and sub-volumes shift) are separated from the IV curve using gray-scale mathematical morphology (Sec. 3.1.1.1). Secondly, the curve remaining after the peaks' separation representing slow trends is processed and the head area with low anatomical variability is detected (Sec. 3.1.1.2). Peaks in the area of low anatomical variability are predominantly caused by a shift of sub-volumes and their subsequent final detection is less complicated (Sec. 3.1.1.3). Considering a constant width of sub-volumes (the number of slices acquired in a single gantry revolution does not change during a particular CT scanning), it is sufficient to detect the sub-volume borders only in this area.

3.1.1.1 Mathematical morphology based peaks separation

IV curves may be intuitively divided into two parts: the first presented by peaks and second presented by slow trend representing anatomical variability inherent to human head. In order to separate these two components a one-dimensional morphological opening and top hats transform are used. Morphological operations are very popular and widely used tool in processing and analysis of binary and gray-scale images. What we propose here is usage of generalized morphological operations to separate peaks and rest of a given function.

Generalized[3] morphological opening is based on combination of two basic morphological operations: erosion $\mathbf{E}_H(x)$ Eq. 3.2 and dilatation $\mathbf{D}_H(x)$ Eq. 3.3 [99].

[3]Generalized morphological operations are exploited to processing of gray-scale images and they

$$y_{i,k} = \mathbf{E}_H(x)|_{\mathbf{x}} = \min_{\mathbf{h}\in H} x\left(\mathbf{x}+\mathbf{h}\right). \tag{3.2}$$

$$y_{i,k} = \mathbf{D}_H(x)|_{\mathbf{x}} = \max_{\mathbf{h}\in H} x\left(\mathbf{x}+\mathbf{h}\right). \tag{3.3}$$

Each pixel i, k of eroded/dilated image y can be expressed as a minimum/maximum of input image's (x) pixels covered by a structuring element (SE) H centered at $\mathbf{x}$. Operation of generalized morphological opening $\mathbf{O}_H(x)$ is cascade of erosion and subsequent dilatation with reflected structuring element $\hat{H}$.

$$\mathbf{O}_H(x) = \mathbf{D}_{\hat{H}}[\mathbf{E}_H(x)]. \tag{3.4}$$

The last morphological operation used in the presented approach is Top Hats transform

$$\mathbf{T}_H(x) = x - \mathbf{O}_H(x) \tag{3.5}$$

defined as a subtraction of a result of opening operation and original image x.

Functionality and properties of peak separation based on morphological opening will be demonstrated on testing function Fig. 3.3a which is sum of four Pearson type VII functions

$$f\left(x\right) = a\left[1+\left(\frac{x-\lambda}{\alpha}\right)^2\right]^{-m}, \tag{3.6}$$

where parameters λ and a determine location of peak maximum (position on x axis and height of a peak, respectively) while m and α affect its shape (rate at which functions tail falls and full width at half maximum, respectively) [35]. The shape parameters allow to control kurtosis of finally generated Pearson VII function which makes it suitable for testing of peak separation algorithm as it is possible to generate peaks with different widths.

Generalized morphological operations are based on set representation of gray-scale images [48] which is of course applicable to one-dimensional signals. Area under given curve may thus be thus perceived as a plane filled by a set of discrete points. Opened set $\mathbf{O}_H(X)$ may be alternatively expressed as union of structural elements H at positions $\mathbf{x}$ where they are entirely fitting the set X

$$\mathbf{O}_H(X) = \bigcup_{\mathbf{x}} \left\{H_{\mathbf{x}} | H_{\mathbf{x}} \subseteq X\right\}. \tag{3.7}$$

Opening of the function with linear (1D) SE oriented parallelly with x axis will thus cut off its narrow parts which are mostly represented by peaks. Vector of separated peaks can be subsequently calculated as top hats transform of original function

are generalization of basic form of mathematical morphology used to work only with binary data. *IV* functions are not binary, thus only generalized morphological operations are used.

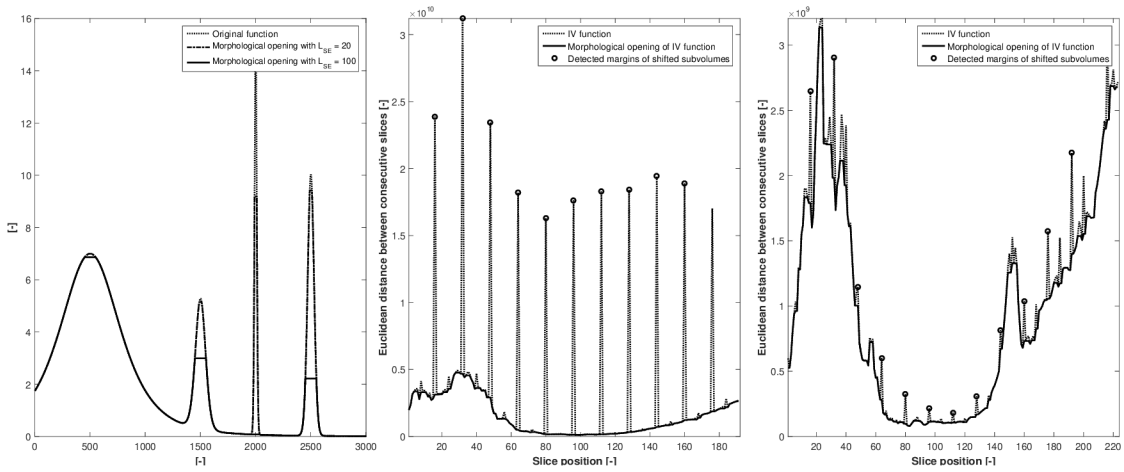

(a) (b) (c)

Obr. 3.3: Demonstration of the peak separation method based on mathematical morphology: (a) Testing function created as a sum of four Pearson's VII functions (dotted line) and two of its openings with lengths of linear structuring element 20 (dash-dotted line) and 100 (solid line), (b) IV function of Fig. 3.1a (dotted line) and its opening (solid line), (c) IV function of Fig. 3.1b (dotted line) and its opening (solid line). Finally detected borders of misplaced sub-volumes are labeled by circles in (b) and (c).

according to Eq. 3.5. The presented approach allows control of the maximal width of separated peak by adjustment of a linear SE length. This property is demonstrated in Fig. 3.3a, where the original function is plotted by the dotted line and is overlaid by two of its openings with SE of different lengths L_{SE} (dash-dotted line plot for $L_{SE} = 20$ and solid line plot for $L_{SE} = 100$). It is obvious that the opening with longer SE is able to separate wider peaks, and the height of such separated peaks can serve as a measure of peak "significance" (considering that only narrow and high peaks are significant). A structuring element with $L_{SE} = 3$ is chosen for the separation of peaks from IV curves. The results of separation of the two exemplary IV curves can be seen in Fig. 3.3b and Fig. 3.3c, where the separated slow trend is visualized by the solid line and the separated peaks are the result of differences between the original dotted line and the slow trend.

3.1.1.2 Determination of head area with low anatomical variability

Morphological openings of IV functions (solid lines in Fig. 3.3b and Fig. 3.3c) can be intuitively divided into three parts according to their height and degree of constancy. In part I, concerning slices from approximately 0 to 60 in Fig. 3.3c, the inter-slice

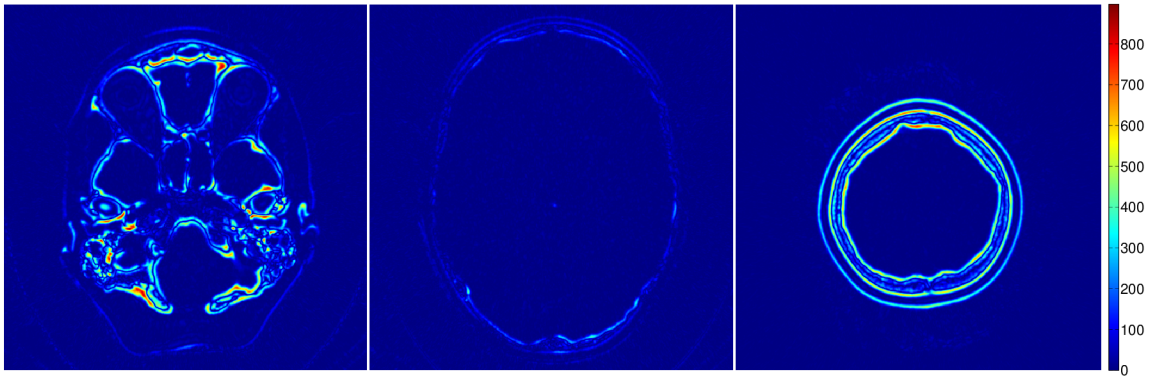

(a) (b) (c)

Obr. 3.4: Absolute values of differences between consecutive slices, demonstrating anatomical variability in three parts of the human head divided according to the degree of anatomical variability: (a) Part I - area of cranial base, difference between slices 25 and 26, (b) Part II - middle part of the human head, difference between slices 100 and 101, and (c) part III - section near to the parietal bone, difference between slices 175 and 176.

variability is high and highly variable, which is the result of the high anatomical variability of the cranial base. In part II, slices from approx. 60 to 140 with low and steady values, reflect a high similarity between consecutive slices in the middle part of the human head (i.e. slices intersecting the frontal and occipital bones above the cranial base). Part III, from approx. 140 to the last slice, is, again, characterized by high and highly variable values resulting from the reduction of head area size in the slices approaching the end of the parietal bone. Images showing absolute values of differences between the consecutive axial slices belonging to the mentioned head parts, which demonstrate the sources of inter-slice variability, can be seen in Fig. 3.4.

Part II of IV functions is characterised by the lowest and nearly constant values of inter-slice variability, which are features used for its detection. Detection is performed on opened versions of IV function, which is, in order to emphasise its inconstancy, firstly differentiated:

$$D = IV * \Big(-1, 1\Big) . \tag{3.8}$$

The result is plotted by a solid line in Fig. 3.5a. The local standard deviation of the

differentiated curve is calculated in a sliding window 21 samples long, according to:

$$\sigma_{LOC}(x) = \sqrt{\frac{1}{N} \sum_{i=-intN/2}^{N/2} (D_{(x+i)} - \mu_x)^2}, \tag{3.9}$$

$$\text{where} \qquad \mu_x = \frac{1}{N} \sum_{i=-intN/2}^{N/2} D_{(x+i)} \tag{3.10}$$

and N is the sliding window length. The resulting function σ_{LOC} (depicted as a dash-dotted line in Fig. 3.5a) is proportional to the local inconsistency in IV function and thus has the lowest values in the second part of the IV curve. The absolute value of difference of the σ_{LOC} curve is calculated:

$$AD = \left| \sigma_{LOC} * \left(-1, 1\right) \right|, \tag{3.11}$$

(depicted as a dashed line in Fig. 3.5a) and transferred to a binary function:

$$L(x) = \begin{cases} 1 & \text{if } AD(x) > \min\left(\sigma_{LOC}\right) \cdot 1.5 \\ 0 & \text{otherwise} \end{cases}, \tag{3.12}$$

which contains ones in the locations where absolute values of changes in local inconsistency σ_{LOC} are relatively low compared to its minimal value (empirically set at 1.5). A labeling algorithm [38] is used to assign a unique label to each continuous group of ones in $L(x)$, which produces a vector of labels $L_{LAB}(x)$, see Fig. 3.5b. The binary function $Q(x)$ defining position of the minimal value in IV function

$$Q(x) = \begin{cases} 1 & \text{if } IV(x) = \min(IV) \\ 0 & \text{otherwise} \end{cases}, \tag{3.13}$$

is used for creating another binary function $P(x)$, in which ones correspond to the labeled area of low inconsistency containing the minimal value of IV function:

$$P(x) = \begin{cases} 1 & \text{if } L_{LAB}(x) = L_{LAB}(Q = 1) \\ 0 & \text{otherwise} \end{cases}. \tag{3.14}$$

This is the searched second part of the IV curve with a low anatomical variability (see the dotted line in Fig. 3.5a).

3.1.1.3 Detection of volume acquired on a single gantry rotation

The finally detected head part with low anatomical variability is subsequently used to crop IV function, and the detection of the widths of misplaced sub-volumes is performed only within this part. A top-hats transform of IV function with separated peaks is used (see the dotted curve in Fig. 3.5c). Even though peaks are

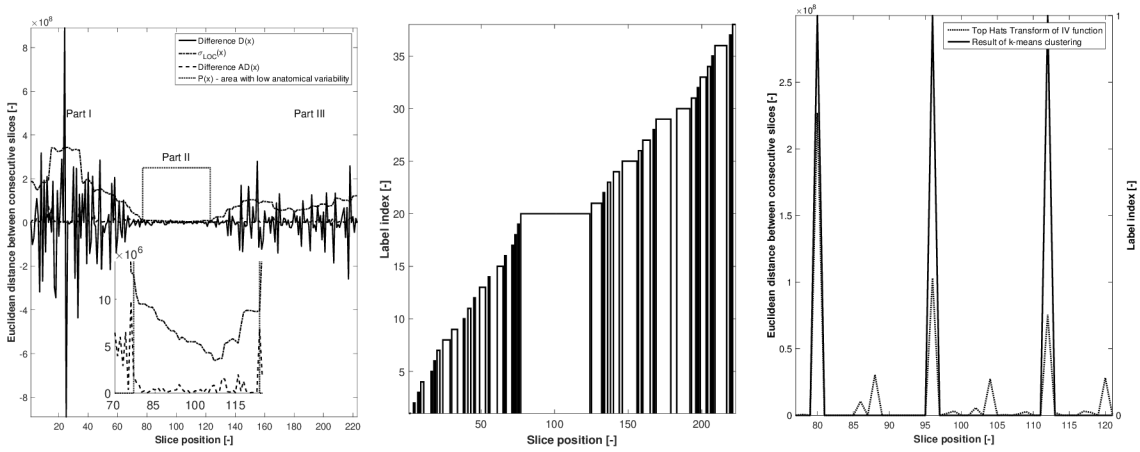

(a) (b) (c)

Obr. 3.5: Process of detection of head section with low anatomical variability and detection of sub-volumes width: (a) stages of processing of opened IV curve: — $D_{(x)}$: difference of opened IV curve; $\cdot - \cdot$ σ_{LOC}: local standard deviation of $D_{(x)}$; $--$ $AD_{(x)}$: difference of σ_{LOC}; $\cdots$ $P_{(x)}$: logical function (scaled in this plot) delimiting searched area of head with low inter-slice anatomical variability, (b) labelled logical function $L(x)$, (c) $\cdots$ top-hats transform of IV in area with low anatomical variability, — result of k-means clustering (detected peaks caused by shift of sub-volumes).

separated only in part II of IV function with low anatomical variability, its top-hats transform contains both types of peaks (caused by anatomical variability and shift of sub-volumes). Although peaks caused by a shift of sub-volumes generally have higher magnitudes, it is impossible to set a reliable threshold which would be able to separate them. Therefore, a K-means clustering algorithm [40] with two clusters initialized by the maximum and minimum of the input function is used instead, and it turns out to be a very reliable solution. The result of clustering, i.e. detected peaks caused predominantly by a shift of sub-volumes, can be seen in Fig. 3.5c (plotted by the solid line). The number of slices acquired on a single gantry rotation is finally calculated as a mode of distances between neighboring detected peaks, and the borders of shifted sub-volumes are thus known (see the circles in Fig. 3.3b and Fig. 3.3c).

3.1.2 Registration of misplaced sub-volumes

Once the borders of misplaced sub-volumes are known, their registration is performed in two steps. Raw shift estimation is provided by a phase correlation method (POC) with sub-pixel precision which is in detail described in Sec. 3.1.3. This is

further refined by the method based on optimization of Euclidean distance similarity criterion (Eq. 3.1) using a gradient method with adaptive step size.

Prior to the computation of normalized cross spectra needed for phase correlation based shift estimation, spectral leakage is reduced by the application of 2D Hann window [39] to both images in the original domain. The images to be registered are naturally burdened by noise. As the head CT data typically have a majority of energy concentrated to the low-frequency parts of spectra, the high frequency components may thus have lower signal to noise ratios (see experiment described in Sec. 3.1.3 with result visualized in Fig. 3.7f). In such cases, normalized cross spectra can be, according to [108], modified by a low pass function. In the presented solution, normalized cross spectra are weighted by rectangular low-pass function given by Eq. 3.25 with $U = V = 100px$. U and V are heuristically selected (based on visual inspection) such that low-pass function roughly corresponds to the spectral area where frequency components have a high signal to noise ratio. The shift is estimated with sub-pixel precision by the fitting of analytical function Eq. 3.26 to a phase correlation matrix. A Levenberg-Marquardt [79] optimization of Euclidean distance similarity criterion between the analytical model and POC function calculated in 3×3 window centered on the position of maximal peak is used.

Phase correlation assumes that the images to be registered are identical, which is not exactly the case in the registration of consecutive slices of CT data. The results may thus be imprecise, especially in the part of the head near to the end of the parietal bone (the third head part according to Sec. 3.1.1.2), where the head area is small while the area of surrounding air, with a low signal to noise ratio, is large. Providing that shift estimation based on phase correlation is burdened by severe errors only in Part III, imprecise estimations can be corrected by the calculation of median in the elongated window:

$$E(k) = median\{E(1, \ldots, k-1), POC_k\}, \tag{3.15}$$

where k is the index of actually estimated shift between sub-volumes, E is the vector of estimated shifts between sub-volumes and POC_k is the k-th shift actually estimated by the phase correlation method.

The result of the described pre-registration is subsequently used as initialization for a final, precise and efficient registration. The Gradient method with adaptive step size (GDD) [56], [57] is used with optimal solution searched according to the iterative scheme:

$$\boldsymbol{\mu}_{k+1} = \boldsymbol{\mu}_k - \gamma_k \boldsymbol{g}_k, \tag{3.16}$$

where $\boldsymbol{\mu}$ is the optimized parameter vector, k an iteration count, $\boldsymbol{g}_k$ is the gradient of cost function in k-th iteration and γ_k is the decaying function determining step

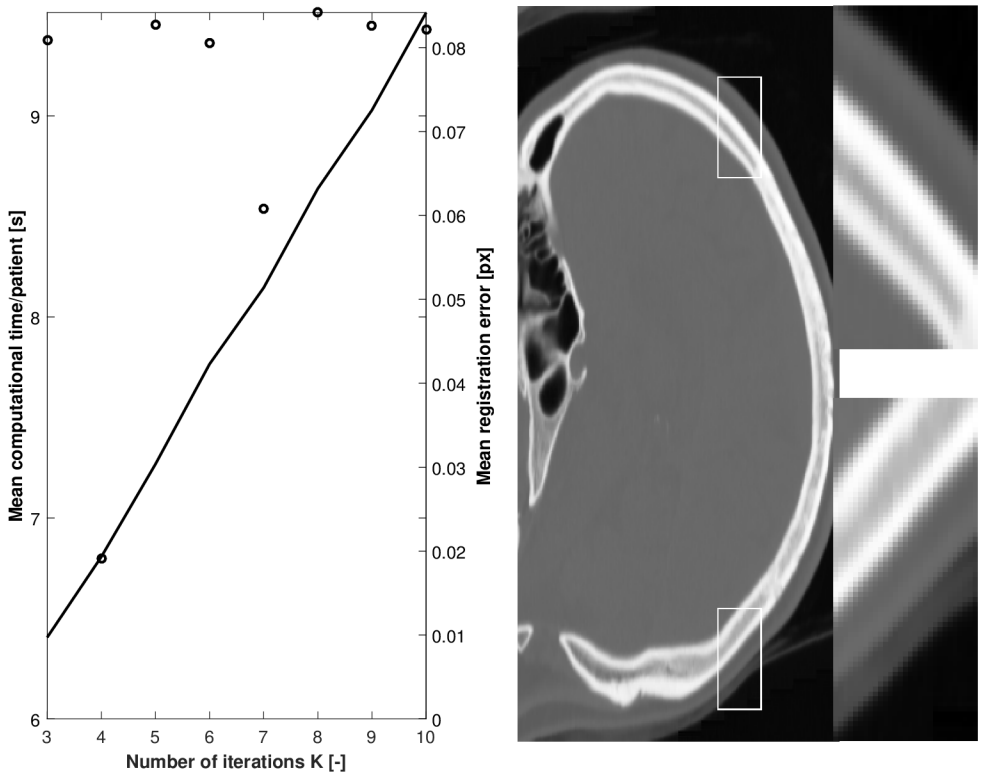

(a) (b)

Obr. 3.6: Results of GDD parameters optimization and example of final stair-step error correction: (a) plot of mean registration errors calculated from results of GDD algorithm with optimized parameters as a function of number of iterations (circles) and mean computational time per patient as a function of number of iterations (solid line), (b) final stair step-error correction of Fig. 3.1a.

size,

$$\gamma_k \equiv \gamma(k) = a/\left(k + A\right)^{\alpha} \tag{3.17}$$

with constants a, A and α generally recommended to be selected from intervals $a > 0$, $A \geqslant 1$ and $0 < \alpha \leqslant 1$, [56], [57]. Those parameters are optimized for the given problem so that a reasonable balance between registration precision and computational cost is achieved.

Thanks to the fact that the presented registration problem is one-dimensional (though concerning 3D data) and the cost functions always have a single distinct minimum, their optimum can always be simply and precisely found by exhaustive search. The registration results from the exhaustive search were verified by a medical expert and were then considered to be optimal registrations (gold standard), which

should be, as closely as possible, achieved by the proposed method. Knowing the optimal solution, it is possible to evaluate the precision of obtained registrations for individual a, A and α settings.

A controlled random search global optimization (CRS) [89] in three dimensional space formed by the parameters a, A and α has been chosen. The cost function is the Euclidean distance between the vector of shifts calculated by the exhaustive search (i.e the aforementioned gold standard) for the whole set of misplaced sub-volumes (409 sub-volumes in data from 33 patients) and equally formed vector of shifts estimated by GDD algorithm with current settings of parameters a, A and α. The searched area for CRS optimization is a priori limited by conditions a, $\alpha \in \langle 0, 15\rangle$; $A \in \langle 1, 15\rangle$; a population of 30 candidate solutions is used and simplex reflection heuristics is chosen. The optimization is stopped when the coefficients of variation (ratios of the standard deviations to the means) of candidate solutions costs are below the experimentally found predefined threshold of 0.001 (i.e. when candidate solutions have approximately equal costs).

The aforementioned optimization of GDD parameters was performed for K values from the interval $\langle 3, 10\rangle$. The mean registration errors with the GDD parameters optimized for individual values of K are depicted in Fig. 3.6a together with the mean computational time per patient. The number of iterations $K = 4$ was finally chosen as the mean registration error was lowest while the mean computational time was the second lowest. An example of final stair-step correction of Fig. 3.1a can be seen in Fig. 3.6b.

The proposed method is able to correctly detect the borders of sub-volumes in 100% of cases. The precision of registration is evaluated as the mean of absolute values of differences between the results of the compared methods and the vector of shifts optimized by exhaustive search and validated by a medical expert. The precision of registration is on a considered data set $0.019 \pm 0.026vx$. Computational requirements of the proposed correction method have been measured on a standard workstation with 2× Intel Xeon CPU @2,53 GHz, 48 GB of RAM, when using MATLAB® R2015b. The mean computational time per patient is $6.81 \pm 0.82s$, for the whole correction procedure including final geometric transform of whole volume of brain CT scan. Such low computational time is ensured by shifting data using a frequency domain approach and by the optimization of registration parameters in such a way that the optimum is found in a number of iterations, which is a certain compromise between registration precision and computational requirements.

3.1.3 Phase correlation shift estimation

Consider two discrete images $f_1(x, y)$ and $f_2(x, y)$ and denote 2D discrete Fourier transform (DFT_{2D}) of the two images as $F_1(u, v)$ and $F_2(u, v)$, respectively, as a product of amplitude $|F_n(u, v)|$ and phase part $\arg(F_n(u, v))$ (an image index should be substituted for n). Suppose that image $f_2(x, y)$ is shifted version of image $f_1(x, y)$ by an integer displacement (x_0, y_0)

$$f_2(x, y) = f_1(x - x_0, y - y_0). \tag{3.18}$$

According to the Fourier shift property, Eq. 3.18 can be transferred to frequency domain as

$$F_2(u, v) = F_1(u, v)e^{-j2\pi(ux_0+vy_0)}, \tag{3.19}$$

which means that shift of an image in original domain is in frequency domain reflected as a linear phase shift with a slope proportional to amount of shift; only a phase part of spectrum is thus affected. Calculating normalized cross spectrum [94]

$$P(u, v) = \frac{F_2(u, v)F_1^*(u, v)}{|F_2(u, v)F_1(u, v)|} \tag{3.20}$$

where * means complex conjugate, substituting Eq. 3.19 and simplifying the result

$$\begin{aligned} P(u, v) &= \frac{F_2(u, v)F_1^*(u, v)}{|F_2(u, v)F_1(u, v)|} = \\ &= \frac{|F_1(u, v)|e^{j\arg(F_1(u,v))}e^{-j2\pi(ux_0+vy_0)}|F_1(u, v)|e^{-j\arg(F_1(u,v))}}{||F_1(u, v)|e^{j\arg(F_1(u,v))}e^{-j2\pi(ux_0+vy_0)}|F_1(u, v)|e^{j\arg(F_1(u,v))}|} = \\ &= \frac{|F_1|^2e^{-j2\pi(ux_0+vy_0)}}{|F_1|^2} = \\ &= e^{-j2\pi(ux_0+vy_0)}, \end{aligned} \tag{3.21}$$

a spectrum with unite amplitude and linear phase part, introduced by shift between images in original domain, is obtained. This spectrum is equal to a spectrum of unite impulse shifted about (x_0, y_0) with respect to the origin of the coordinate system. Inverse 2D discrete Fourier transform (DFT_{2D}^{-1})

$$p(x, y) = DFT_{2D}^{-1}\{P(u, v)\} = DFT_{2D}^{-1}\left\{e^{-j2\pi(ux_0+vy_0)}\right\} = \delta(x_0, y_0), \tag{3.22}$$

will, thus, result to an accordingly shifted unite impulse and produce a phase correlation function $p(x, y)$. Desired displacement between images can be identified as position of the maximum in $p(x, y)$ data array.

Phase correlation based displacement estimation method assumes that images to be registered are identical, which may introduce errors or inaccuracies in practical applications where this condition is often violated (e.g. by noise). Even in cases when

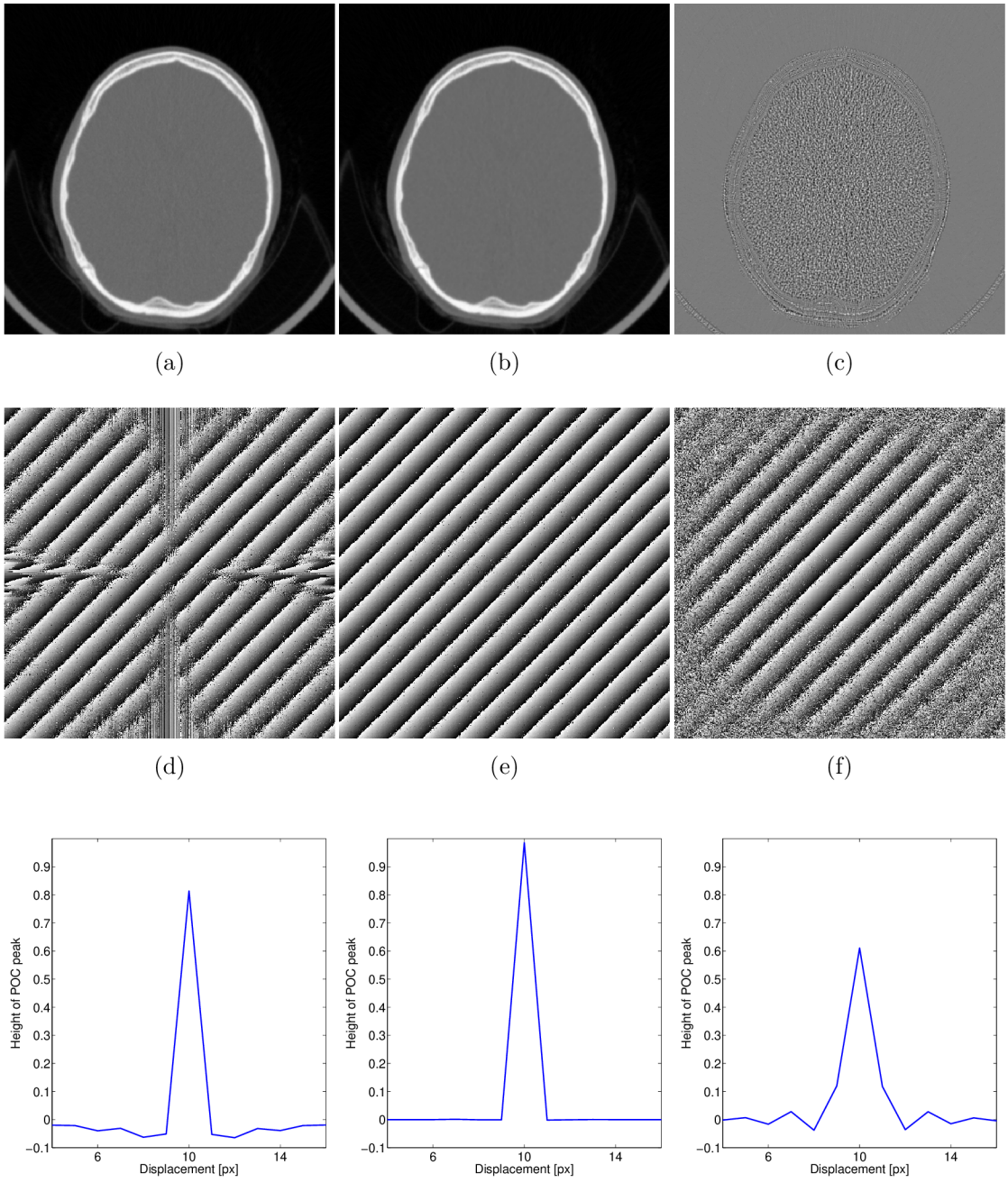

Obr. 3.7: Demonstration of practical aspects of phase correlation alignment method: (a) Slice of head CT data reconstructed by FBP, (b) Slice of head CT data reconstructed by iDose[4], (c) difference of (a) and (b); phase part of normalized cross spectrum of: (d) FBP reconstructed image and its version shifted about $(x_0, y_0) = (10, 10)$, (e) FBP reconstructed image and its version shifted about $(x_0, y_0) = (10, 10)$ when both images are weighted by 2D Hann window, (f) FBP image and iDose[4] reconstructed image shifted about $(x_0, y_0) = (10, 10)$; (g - i) cross-sections of phase correlation function taken through its maximal peak, plots are corresponding to cross spectra above.

moving image is only a shifted version of a base image, the exact unite impulse may not arise in their phase correlation function due to bordering effect imposed by periodicity of DFT. DFT periodicity enforces creation of artificial edges on image margins (assuming that pixel intensities are different on opposite image borders) which are sources of artificial frequency components. Shifting the image, pixels with different values appear on margins of the shifted image, bordering effect and artificial frequency components are, hence, changed. Spectra of registered images are no longer identical and inaccuracies are introduced to their cross spectrum, see $\arg(P(u,v))$ in Fig. 3.7d calculated between Fig. 3.7a and its version shifted by $(10,10)px$. Negative effect of DFT periodicity can be reduced by applying 2D weighting function; e.g. 2D Hann window

$$w(x,y) = 0.5\left(1-\cos\left(\frac{2\pi x}{X-1}\right)\right) \times 0.5\left(1-\cos\left(\frac{2\pi y}{Y-1}\right)\right)^{\top}, \tag{3.23}$$

defined as a cross product of two one-dimensional Hann windows where X, Y are image sizes in x, y directions. Improvement of precision of cross spectrum calculation, after a Hann windowing function is applied, is evident from comparison of Fig. 3.7d and Fig. 3.7e. The maximal peak in phase correlation function is also more pronounced (peak height is closer to unity and values outside of the peak are closer to zero) using 2D Hann window (compare Fig. 3.7g and Fig. 3.7h).

Image noise is another aspect of real life images which is able to complicate registration using phase correlation method. Normalized cross spectrum of real images with different noise realizations[4] can be seen in Fig. 3.7f. Natural images have typically majority of energy concentrated to low frequency components and thus high frequency components may have lower signal to noise ratio (providing that image noise have uniform spectrum). This effect is demonstrated in Fig. 3.7f where a typical linear phase shift[5] is highly violated on higher frequencies which also negatively influence height of phase correlation peak in Fig. 3.7i.

3.1.3.1 Extension to sub-pixel precision

Considering two identical images displaced by an integer shift, a phase correlation matrix contains, according to [23], 2D Dirichlet function sampled exactly in the maximum of main lobe and otherwise only when 2D Dirichlet function crosses the zero. The phase correlation matrix, thus, contains a single peak determining the

[4]Identical data with different noise realizations are simulated by a couple of CT scans of identical scene reconstructed from single raw data by two methods with different ability to suppress image noise, see Fig. 3.7a and Fig. 3.7b; level of noise contained in the two images is thus different which is demonstrated by their subtraction in Fig. 3.7c.

[5]Discontinuities are caused by wrapping around π and $-\pi$.

shift (so-called coherent peak) and also some incoherent peaks may occur resulting from e.g. bordering effect or noise. On the contrary, in case of the sub-pixel displacement, phase correlation matrix contains 2D Dirichlet function sampled in locations depending on amount of sub-pixel shift. Hence, a phase correlation matrix contains a compact group of several coherent peaks which may be used for sub-pixel shift estimation.

Several approaches for phase correlation based sub-pixel shift estimation have been proposed in both original and frequency domain among which an approach originally presented in [108] and extended in [83] is used in this thesis. Shape of a phase correlation peak can be, according to [108], modeled by

$$p(x,y) \cong \frac{\alpha}{XY} \frac{\sin\{\pi(x+x_0)\}}{\sin\{\frac{\pi}{X}(x+x_0)\}} \frac{\sin\{\pi(y+y_0)\}}{\sin\{\frac{\pi}{Y}(y+y_0)\}}, \tag{3.24}$$

where α determines maximum height in a group of coherent peaks. Model function is subsequently fitted to a phase correlation matrix producing optimal estimation of sub-pixel shift vector (x_0, y_0). As already mentioned, image noise may negatively influence process of phase correlation based shift estimation especially when sub-pixel precision is needed. Robustness with respect to image noise can be, according to [108], improved by an application of low-pass function to a normalized cross spectrum prior to computation of phase correlation matrix. Application of a low-pass function naturally influences shape of a coherent phase correlation peak. After application of rectangular weighting function defined by

$$H_1(u,v) = \begin{cases} 1 & |u| \leqslant U, |v| \leqslant V \\ 0 & \text{otherwise} \end{cases}, \tag{3.25}$$

where U, V are integers satisfying $0 \leqslant U \leqslant X/2$ and $0 \leqslant V \leqslant Y/2$, shape of a phase correlation peak will be, according to [108], changed to

$$p(x,y) \cong \frac{\alpha}{XY} \frac{\sin\{\frac{U}{X}\pi(x+x_0)\}}{\sin\{\frac{\pi}{X}(x+x_0)\}} \frac{\sin\{\frac{V}{Y}\pi(y+y_0)\}}{\sin\{\frac{\pi}{Y}(y+y_0)\}}. \tag{3.26}$$

3.2 Segmentation of basic tissues in CT head data

Acquired data contain also unimportant structures, such as surrounding air and patient table, which must be removed prior to applying the segmentation method. Thresholding with by Otsu method [85] determined threshold, which optimally distinguish between objects and background is initially used. Providing that the largest connected binary segment represents human head (it is always true for our data set), other foreground structures are removed by binary area opening [99]. The last step is addition of structures from background (typically paranasal sinuses) to the final

segmentation. With respect to continuity of human body, organs filled by air must be surrounded by tissue, hence, the addition can be performed by filling based on morphological reconstruction [99].

To be able to assess noise properties separately in basic tissues of a human head (typically soft tissue, bones, adipose tissue and air filled structures like paranasal sinuses or internal auditories) an automatic and reliable segmentation algorithm is needed. Typical gray-scale histogram of human head CT scan contains three significant peaks which represent air filled tissue, soft tissue and adipose tissue. The peaks and thus corresponding tissues could be easily separated by a thresholding like in [113] and [112]. Disadvantage of thresholding is its high sensitivity to noise which leads to many misclassified voxels [113]; segmentation method utilizing graph-cuts [12] is used instead as it incorporates information not only about intensity of voxel to be classified but also about intensities of neighboring voxels. Graph-cut based segmentation is, hence, much less sensitive to noise (for detailed description of grap-cut based segmentation algorithm see Sec. 3.2.3).

The method requires prior knowledge in form of interactive labeling of voxels subsets taken from segmented background and object which are subsequently used for computation of corresponding intensity distributions $Pr\left(I|\mathcal{O}\right)$ and $Pr\left(I|\mathcal{B}\right)$ in Eq. 3.35. Thanks to the fact that positions of peaks representing tissues in histogram of CT head scan are not significantly varying among individuals (partly thanks to consistency of scanning parameters and partly thanks to the fact, that tissues of human head are not changing significantly with patient age, weight and sex), therefore, in this case, it is sufficient to set the intensity distributions as a cumulative distribution functions of normal distribution with heuristically determined means (set with respect to locations of the tissue peaks) and standard deviations. Setting of graph cut based segmentation of CT head scans is summarized in Tab. 3.2 where μ represent mean value whereas σ_A and σ_B standard deviations of ascending and descending parts of normal distribution; λ is parameter from Eq. 3.34 and σ from Eq. 3.37.

Tab. 3.2: Settings of parameters of graph cut based segmentation of basic tissues in a head CT scans. μ, σ_A and σ_B are parameters of Gaussian curves representing intensity distributions Eq. 3.35; λ is parameter from Eq. 3.34 and σ from Eq. 3.37.

	μ	σ_A	σ_B	λ	σ
Air filled structures	-270 HU	700 HU	700 HU	0.001	10 HU
Adipose tissue	-20 HU	40 HU	40 HU	10	2 HU
Bones	270 HU	80 HU	200 HU	0.1	4 HU

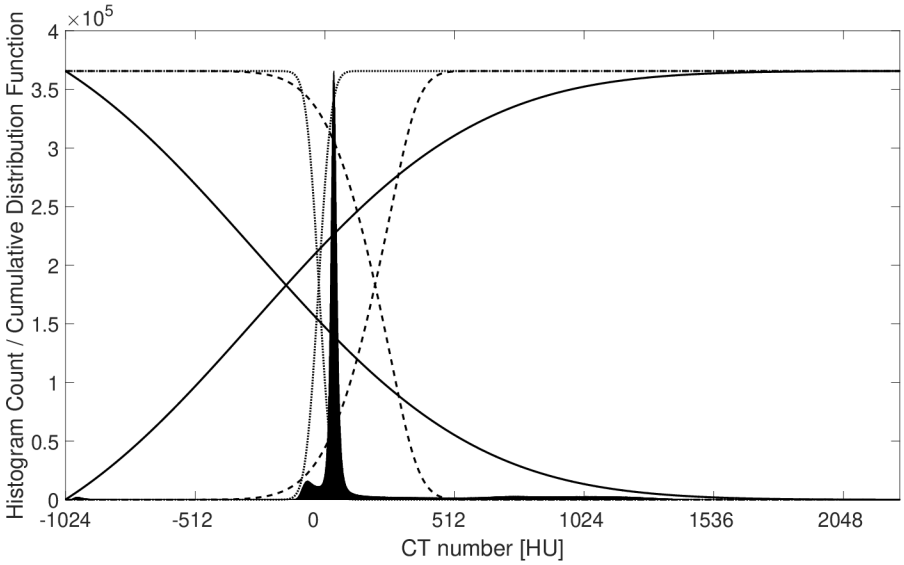

Obr. 3.8: Gray-scale histogram of typical CT head scan plotted as a bar graph. Prior knowledge for graph cut based segmentation in form of cumulative distribution functions representing probability of membership of individual voxels to object $Pr\left(I|\mathcal{O}\right)$ or background $Pr\left(I|\mathcal{B}\right)$ for air filled tissues (solid lines; —), adipose tissue (dotted lines; $\cdots$) and bones (dashed lines; $- - -$). The curves are scaled by the maximal value of the histogram in this plot.

Greatest standard deviations σ_A and σ_B are set for segmentation of air filled structures as they contain also septa among individual paranasal sinuses with higher densities (similar to densities of soft and adipose tissue), as can be seen in Fig. 3.9a and Fig. 3.9b where paranasal sinuses are finally segmented. This setting ensures that relatively small differences between $Pr\left(I|\mathcal{O}\right)$ and $Pr\left(I|\mathcal{B}\right)$ are assigned to densities of septa (see solid lines in Fig. 3.8) which can, thus, be highly affected by a boundary term in Eq. 3.37 and correctly labeled as a part of paranasal sinuses. Parameters λ and σ are, in this case, also set to emphasize boundary term. Example of graph-cut based segmentation of basic tissues, demonstrated on a single slice of CT data Fig. 3.9a, can be seen in Fig. 3.9. Segmentation of adipose and air filled structures is satisfactory whereas segmentation of bones contains obviously many misclassified voxels.

Skull segmentation is more challenging problem partially due to very complex structure of cranial base with thin cortical bone parts and partially due to overlapped densities of inner parts of bones (trabecular bones) and soft tissue; as can be seen in histograms of manually selected parts of both tissues in Fig. 3.10. Asymmetrical normal distribution (with different σ_A and σ_B) is used (see dashed line in Fig. 3.8) in graph-cut based skull segmentation. A greater σ value is used for densities typical

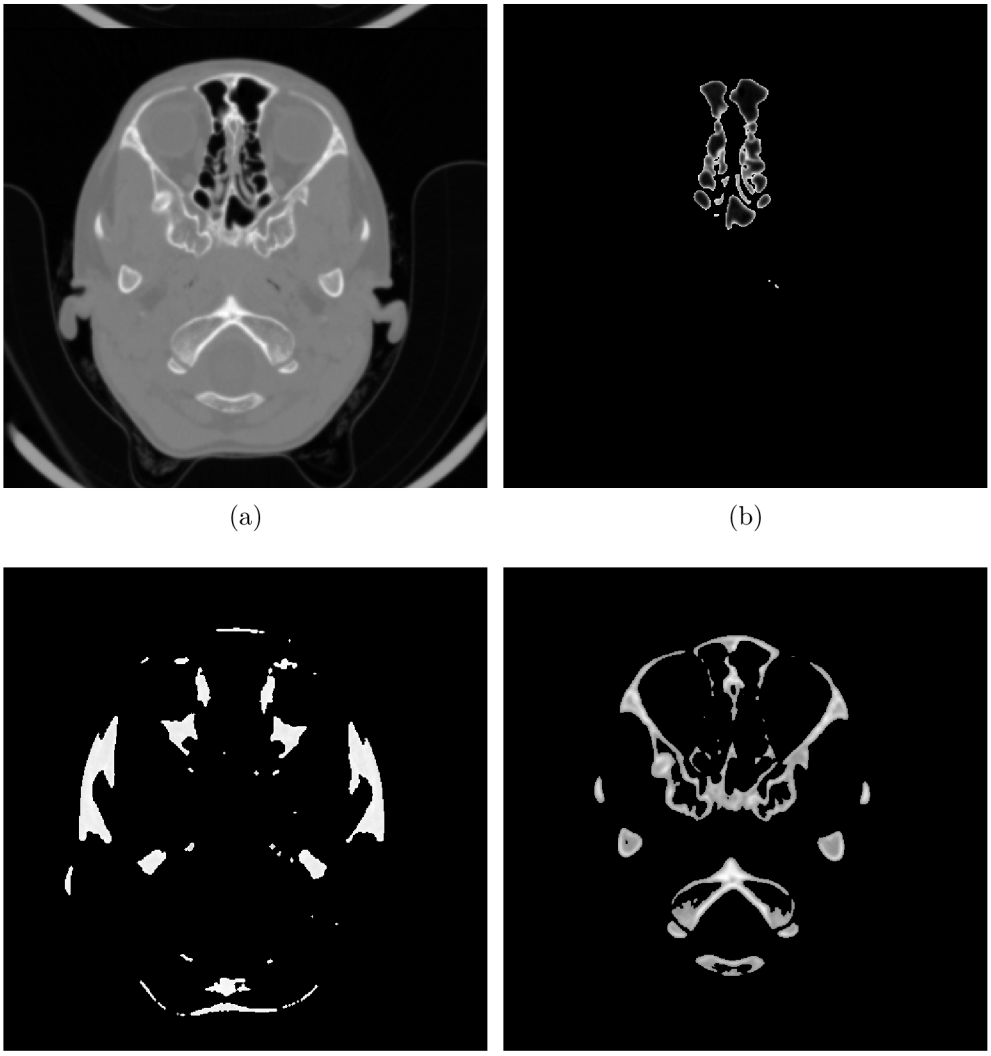

(a) (b)

(c) (d)

Obr. 3.9: Example of result of graph-cut based segmentation of basic tissues: (a) slice of original data; (b) segmented air filled tissue; (c) segmented adipose tissue, (d) segmented bones.

to soft tissue which can, thus, be more easily influenced by a boundary term and classified as a trabecular bone part or a weak cortical bone. Lower σ used for densities typical for bones prevents incorrect classification of soft tissue as a bone in locations where bones are very close to each other.

Even though graph-cut based bones segmentation results are much better than those produced by thresholding, some parts of cortical bones are missing as well as large areas of trabecular bones parts. Those imperfections are corrected in two steps; missing parts of cortical bones are, firstly, added to the segmentation using analysis of segmented contour as described in Sec. 3.2.1. In the second step, so called

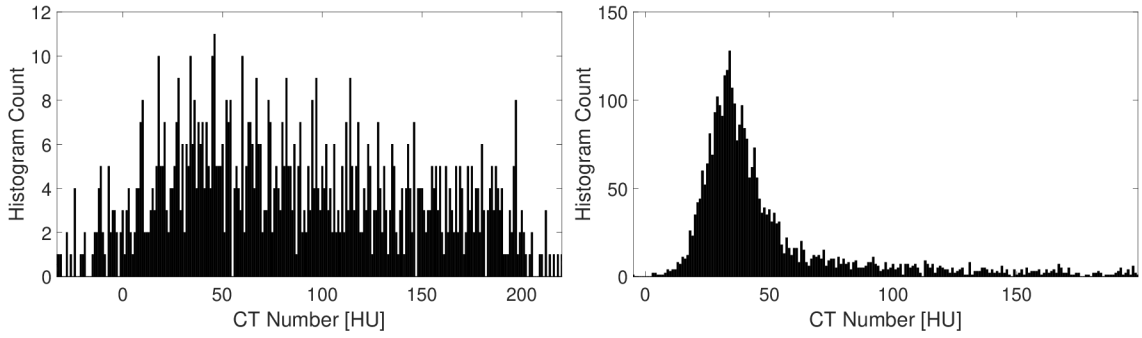

(a) (b)

Obr. 3.10: Typical histograms of manually selected parts of trabecular bone (a) and soft tissue (b).

holes (i.e. areas of zeros fully surrounded by ones in a binary segmentation mask), which may represent either trabecular bone or soft tissue, are classified in Sec. 3.2.2 utilizing differences of shape of their local histograms.

3.2.1 Correction of mis-segmented cortical bones parts

The presented correction of mis-segmented parts of cortical bones can be divided into two main steps; points on a contour which are considered to be candidates for locations where segmented bone is incorrectly disconnected are, firstly, detected using analysis of contour shape. A pair of candidates connected by a Canny edge [13] is, in the second step, considered to be points of mis-segmented bone and the contour is corrected by adding a part of Canny edge delimited by the candidates.

Interior pixels (active pixels with all neighboring pixels also active) of a segmented binary object are firstly removed; remaining active pixels, thus, represent object contour. A contour of exemplary bones from Fig. 3.9d is depicted by white color in Fig. 3.12a. A bone contour is transformed to two vectors x and y of spatial coordinates by boundary tracking algorithm, see Fig. 3.11a where only contour of the largest object is depicted. Functions which transfer those vectors to a one-dimensional signals are called shape signatures. A cumulative angular function [125] have been chosen among many routinely used shape signatures to describe contour of segmented bones. Tangent angles $\Theta(n)$ of a boundary represented by vectors x and y given by

$$\Theta(n) = \arctan\left(\frac{y(n) - y(n-\omega)}{x(n) - x(n-\omega)}\right), \tag{3.27}$$

where ω is a window necessary for calculation of the tangent, are a good indication of changes in boundary's shape. In order to decrease sensitivity to gentle contour variations, tangent angle for a particular contour pixel is computed as a mean of

tangent angles computed in eleven elements long window ω centered around n. $\Theta(n)$ may generally contain discontinuities caused by wrapping around 2π, cumulative angular function [125]

$$\varphi(n) = (\Theta(n) - \Theta(0)) \mod (2\pi), \tag{3.28}$$

defined as difference between tangent angle at actual n and the starting position. Cumulative angular function of an exemplary contour is depicted in Fig. 3.11b by dashed line. Locations, in which segmentation of cortical bone is falsely interrupted, are characteristic by a steep change in $\varphi(n)$. In order to emphasize steep changes a cumulative angular function is filtered by a heuristically selected biorthogonal 1.5 wavelet with scale 10, result of filtering is depicted in Fig. 3.11b by solid line. Thresholding with an adaptive threshold, set as 0.5 times standard deviation of filtered cumulative angular function (the threshold is depicted by dotted line in Fig. 3.11b), is used to detect mis-segmented cortical bones candidates, whereas only a maximum of a peak above a threshold is considered. Examples of detections of mis-segmented cortical bone candidates can be seen in Fig. 3.12a depicted by red color.

As stated before, edges detected by Canny edge detector [13], see example in Fig. 3.12b, are used to correct mis-segmented parts of cortical bones. The previously detected mis-segmented bone candidates need not necessarily be located on Canny edges, they are, thus, moved to be parts of Canny edges. Canny edges contained in 7×7 sub-image centered at detected mis-segmented bone candidate location are taken into account. An unique label is assigned to the pixel of Canny edge which is closest to the mis-segmented bone candidate location. A set of labeled pixels located on Canny edges corresponding to mis-segmented bone candidate locations is obtained. Each such labeled pixel serves as a starting point for Canny edges tracing. If there is another labeled pixel found during the edge tracing (which means that the Canny edge is connecting two mis-segmented bone candidates), a corresponding edge segment delineated by a starting point and found labeled pixel is added to bones segmentation. Exemplary results of correction of mis-segmented cortical bone parts can be seen in Fig. 3.12c and Fig. 3.13a.

3.2.2 Classification of soft tissue and trabecular bones

Contours of cortical bones are fully closed after the proposed correction and areas of mis-classified trabecular bones are now represented by areas of zeros fully surrounded by ones called “holes”. Holes may represent either trabecular bone or soft tissue and they, therefore, have to be classified into the two groups. As already mentioned, densities of soft tissue and trabecular bones are partially overlapping, however their

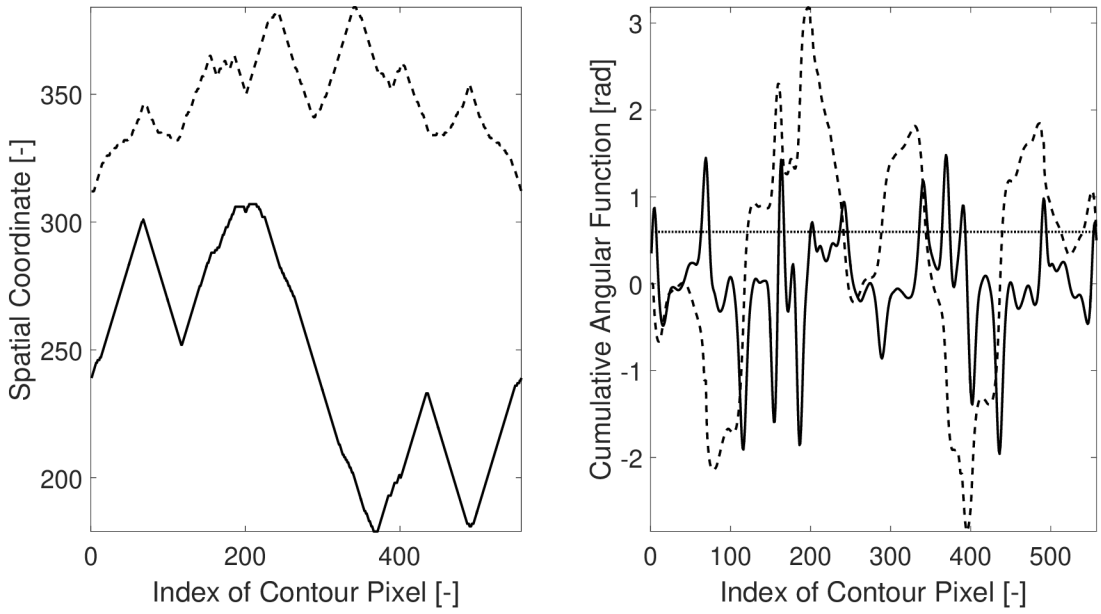

(a) (b)

Obr. 3.11: Example of detection of mis-segmented cortical bones candidates: (a) contour of segmented binary object (the largest one in Fig. 3.12a) transformed to two vectors of x (solid line; —) and y (dashed line; − − −) coordinates, (b) corresponding cumulative angular function (dashed line; − − −), result of filtering by biorthogonal 1.5 wavelet (solid line; —); threshold for determination of candidates for mis-segmented bones locations (dotted line; $\cdots$).

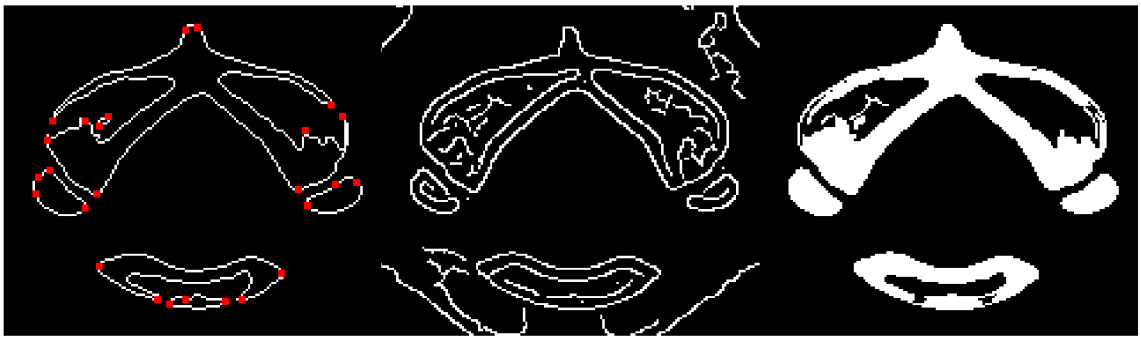

(a) (b) (c)

Obr. 3.12: Correction of mis-segmented cortical bones parts by Canny edges: (a) Contour of one segmented bone from Fig. 3.9d with detected candidates for mis-segmented bones parts depicted by red color. (b) Result of Canny edge detection. (c) Finally corrected cortical bone segmentation.

histograms substantially differ in their shapes. Histograms of trabecular bones parts are, in comparison with soft tissue ones, skewed towards higher values and distribution of Hounsfield units, approximated by a histogram, is much more similar to even distribution, see Fig. 3.10. The differences in shape of the histograms are quantified by four parameters: entropy (Eq. 3.29), ratio of mean value of HU in a hole and position of maximum of a soft tissue peak (reliably represented by the position of the maximum in the histogram of whole head scan $H_{\max}$) (Eq. 3.30), skewness (Eq. 3.31) and kurtosis (Eq. 3.32).

$$S = -\frac{1}{N}\sum_{i=0}^{n-1} x_i \log(x_i), \qquad (3.29)$$

$$C = \frac{\mu}{H_{\max}} \qquad (3.30)$$

$$\gamma_1 = \frac{\frac{1}{N}\sum_{i=0}^{n-1}(i-\mu)^3}{\left[\frac{1}{N}\sum_{i=0}^{n-1}(x_i i)^2 - \mu^2\right]^{\frac{3}{2}}}, \qquad (3.31)$$

$$\gamma_2 = \frac{\frac{1}{N}\sum_{i=0}^{n-1}(i-\mu)^4}{\left[\frac{1}{N}\sum_{i=0}^{n-1}(x_i i)^2 - \mu^2\right]^{2}} - 3. \qquad (3.32)$$

In each of the equations (3.29 - 3.32) N means sum of all counts in bins (i.e. number of pixels in a hole), μ is a mean value of a histogram, i is a bin mark and x_i means count in the bin marked as i.

Each hole is, thus, characterized by a vector of parameters 3.29 - 3.32. A feed-forward neural network [47] trained by Levenberg-Marquardt back propagation algorithm [36] is used to classify them into two groups (trabecular bone and soft tissue). A set of 300 exemplary vectors manually classified by a medical expert is used to the net training whereas 70% of exemplary vectors are used for training, 15% for validation and 15% for testing. 8420 different net architectures were trained (number of hidden layers varied from 1 to 3 and number of neurons in layers from 1 to 20) hundred times and mean performance of each architecture (represented by mean Pearson correlation coefficient Eq. 3.33 measured on the testing set) was calculated. Architecture with the best performance, with 3 hidden layers and 20, 8 and 18 neurons in corresponding layers, is finally used.

In order to improve precision of neural network classification, holes are merged in 3D space and final vectors of the parameters for neural network classification are computed from three-dimensional objects (i.e. from bigger amount of voxels producing their more accurate descriptions). 3D space holes merging is based on the following procedure. Parameter vectors of holes, spatially overlapping between neighboring slices (independently of the direction), are compared using Pearson

correlation coefficient

$$r(\mathbf{a},\mathbf{b}) = \frac{\sum_{i=0}^{N}(a_i-\bar{a})(b_i-\bar{b})}{\sqrt{\sum_{i=0}^{N}(a_i-\bar{a})^2}\sqrt{\sum_{i=0}^{N}(b_i-\bar{b})^2}}, \tag{3.33}$$

which measures degree of linear dependence between vectors **a** and **b** in a length of N, where $\bar{a}$ and $\bar{b}$ are mean values of corresponding vectors. Overlapping holes, with Pearson correlation coefficient greater than 0.95, are considered to be representations of identical tissue and are merged (i.e. their unique labels are set to an identical integer value). This way, a set of volumes of either soft tissue or trabecular bone are obtained and enters the neural network classifier.

A single-pixel lines remaining in the bone segmentation after the trabecular bones adding, i.e. Canny edges falsely added to a bones segmentation, are removed using morphological opening with single-pixel structural element. Example of final bones segmentation can be seen in Fig. 3.13b. Segmentation of remaining tissue type (i.e. soft tissue) is carried out as a binary complement to segmentation of the bones, air filled and adipose tissue, see example in Fig. 3.13c.

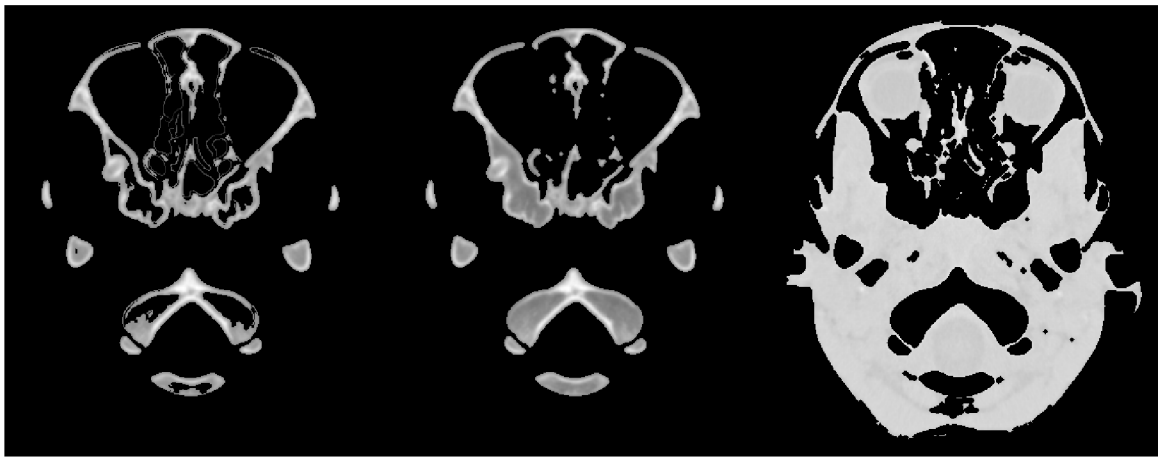

(a) (b) (c)

Obr. 3.13: Example of correction of mis-segmented bones parts remaining after graph-cut based segmentation; example of segmentation of soft tissue: (a) example of correction of mis-segmented cortical bone parts remaining after graph-cut based segmentation Fig. 3.9d, (b) example of a final bones segmentation after adding recognized trabecular bone parts, (c) example of segmentation of soft tissue.

3.2.3 Graph cuts based segmentation

A method for globally optimal image segmentation utilizing graph cuts proposed in [12] uses representation of an image as a undirected graph $\mathcal{G} = \langle \mathcal{V}, \mathcal{E} \rangle$ with set of nodes $\mathcal{V}$ and set of edges $\mathcal{E}$. The nodes of a graph are represented by image voxels connected with their neighbors by edges called n-links, and also by two special (terminal) nodes S (source) and T (sink). Source and sink are connected with each node represented by voxel by so called t-links. All graph edges are assigned by a weight w_e. An s-t cut is a subset of edges $C \subset \mathcal{E}$ which fully separate both terminal nodes with cost equal to sum of costs of separated edges. The s-t cut with minimal cost, which defines the desired segmentation, balances boundary (represented by sum of separated n-links) and region (represented by sum of separated t-links) properties of the segmentation.

Denote set of image elements as $\mathcal{P}$; an arbitrary chosen neighboring system, represented by a set of all pairs $\{p, q\}$ of neighboring elements, as $\mathcal{N}$ and a binary vector $A(A_1, \ldots, A_p, \ldots, A_{|\mathcal{P}|})$ which defines assignment of each image element to an object or background. Segmentation energy minimized by s-t cut

$$E(A) = \lambda \cdot R(A) + B(A) \tag{3.34}$$

is a combination of a region $R(A)$ and a boundary $B(A)$ term weighted by non-negative coefficient λ which determines the importance of both terms. Region term reflects how individual voxels fit into histograms of background and object. Providing that intensity distributions of object $Pr(I|\mathcal{O})$ and background $Pr(I|\mathcal{B})$ are known, corresponding region terms can be set as their negative log-likelihoods

$$\begin{aligned} R_p(\mathcal{O}) &= -\ln Pr(I_p|\mathcal{O}), \\ R_p(\mathcal{B}) &= -\ln Pr(I_p|\mathcal{B}), \end{aligned} \tag{3.35}$$

whereas a cost of a region term for a given segmentation A_p is

$$R(A) = \sum_{p \in \mathcal{P}} R_p(A_p). \tag{3.36}$$

A heuristic function

$$B_{p,q} \propto \exp\left(-\frac{(I_p - I_q)^2}{2\sigma^2}\right) \frac{1}{dist(p, q)} \tag{3.37}$$

suggested in [12] is used to evaluate cost of a boundary term. $B_{p,q}$ for a pair of voxels I_p and I_q with similar intensities (relatively according to standard deviation σ) is high and on the contrary low for voxels with dissimilar intensities; its value is also weighted by a distance between considered voxels. A cost of region term defined by

$$B(A) = \sum_{\{p,q\} \in \mathcal{N}} B_{p,q} \cdot \delta(A_p, A_q), \tag{3.38}$$

where

$$\delta\left(A_p, A_q\right) = \begin{cases} 1 & \text{if} A_p \neq A_q \\ 0 & \text{otherwise,} \end{cases} \tag{3.39}$$

thus, can be viewed as a sum of penalties for cutting n-links.

3.3 Airways segmentation

Prior to airways segmentation, lungs have to be segmented in order to define region of interest where the airways are located. Segmentation of lungs in CT data is relatively easy task thanks to a high contrast to surrounding tissue. A method based on thresholding with static predefined threshold followed by a morphological reconstruction based image filling (inclusion of lung vessels omitted during thresholding) and binary morphological opening (simplification of lung contour) was sufficient for raw lungs identification.

As airways segmentation is not a crucial part of this thesis, a method inspired by [5] which is easy to implement and gives satisfactory results is used. However, this method is slightly modified; morphological reconstruction is calculated directly in 3D space (instead 2D slice by slice calculation) and thresholding after morphological reconstruction (which produces airways candidates) is replaced by graph-cut segmentation.

The presented airways segmentation method is composed from three main steps; gray-scale morphological reconstruction is calculated several times with diverse sizes of structural element in order to enhance airways. Data after the enhancement are segmented by graph-cut method which produces binary airways candidates. The final segmentation is obtained by binary region growing with automatically determined seed.

3.3.1 Airways enhancement by gray-scale morphological reconstruction

Morphological reconstruction is a method for local extremes enhancement and detection which is widely used in image processing field. Besides airways segmentation in CT images [5], [55], an automatic detection of cell nuclei in microscope images [86], blood vessels segmentation in retinal images [73], [88] or coronary wall segmentation in ultrasound data[78] may be given as examples of its practical utilization in biomedical imaging. Underlying theory of gray-scale mathematical reconstruction can be found in [111] and [99].

Enhancement of a local minima in image data I, and, thus, airways which always have lower density than the surrounding tissue, by gray-scale mathematical morphology is, according to [5], based on following procedure. A so called marker image J is initially obtained by gray-scale morphological closing according to

$$J = \mathbf{E}_{\hat{H}1}[\mathbf{D}_{H1}(I)]. \tag{3.40}$$

Gray-scale reconstruction is an iterative process described by

$$J_{k+1} = \max\left(\mathbf{E}_{H2}(J_k), I\right), \tag{3.41}$$

where reconstructed image in k+1 iteration (J_{k+1}) is obtained by a voxel-by-voxel maximum computed between an original image and image resulting from previous iteration eroded with structural element H_2 (shape of H_2 is 4-connected binary diamond). The iterations are initialized by the marker image $J_0 = J$ and are repeated until idempotency; the resulting reconstructed image is denoted as J_∞. In the finally reconstructed image, local minima smaller than spatial extent of structural element $H1$ are filled by a value proportional to the difference between minimal and maximal value in the neighborhood (defined by spatial extent of $H1$) of local minimum. Finally, a difference image

$$D = J_\infty - I \tag{3.42}$$

is computed, where the regions corresponding to local minima in original data are highly enhanced.

Individual stages of gray-scale morphological reconstruction based airways enhancement of exemplary slice of CT data Fig. 3.15a are visualized in Fig. 3.14.

The choice of $H1$ fundamentally affects shape and size of objects which will be enhanced. A set of disc shaped structural elements with various diameters (21, 17, 13, 9, 5, 3) px are used in this application as majority of airways cross sections are circularly shaped and their diameters are gradually decreasing when they approach peripheral lungs parts. As can be observed in Fig. 3.15, where enhancements of airways with different sizes of structural elements are visualized, contrast of thin airways with respect to surrounding lung parenchyma is much higher when SE with lower diameter is used. A set of six three-dimensional matrices with differently enhanced airways is produced in this step.

3.3.2 Segmentation of airways candidates

The next step in airways segmentation is extraction of airways candidates. Instead of thresholding like in [5] and [55], graph-cut based method, described in Sec. 3.2.3, is used. Except the μ which represents mean value of Gaussian type probability

(a) (b) (c)

Obr. 3.14: Individual stages of gray-scale morphological reconstruction based airways segmentation of exemplary slice of CT data Fig. 3.15a; images are weighted by a binary mask of segmented lungs: (a) marker image, (b) gray-scale reconstruction, (c) airways enhancement.

(a) (b) (c)

Obr. 3.15: Demonstration of the effect of $H1$ structural element size to airways enhancement based on gray-scale morphological reconstruction: (a) exemplary slice of lung CT data, (b) airways enhancement with diameter $H1$ equal to 21, (c) airways enhancement with diameter $H1$ equal to 5.

functions $Pr\left(I|\mathcal{O}\right)$ and $Pr\left(I|\mathcal{B}\right)$ in Eq. 3.35, parameters needed for graph-cut segmentation are heuristically determined as $\sigma_A = 50$, $\sigma_B = 50$, $\lambda = 1$, $\sigma = 5$. As can be observed in Fig. 3.15, the enhancement with a different size of $H1$ produces a different contrast (with respect to surrounding tissues) for airways with different widths. Hence, it would be advantageous to determine μ parameter adaptively for each differently enhanced data. With decreasing size of $H1$, thinner airways are more enhanced which have lower overall spatial extent. Setting of μ parameter, thus, reflects this relation. For each size of $H1$, μ is determined as a gray level in

which normalized cumulative histogram of enhanced data reaches a certain value according to Tab. 3.3.

Tab. 3.3: Parameters for thresholding of moralized cumulative histograms of data enhanced by diverse diameters of $H1$, which are utilized for adaptive selection of μ parameter for graph-cut based generation of airways candidates.

Diameter of $H1$	21	17	13	9	5	3
Cum. Hist. Threshold	0.9500	0.9850	0.9875	0.9900	0.9900	0.9900

Six binary matrices containing candidates for airways are obtained after the graph-cut segmentation; a final matrix of the candidates is computed as their union, which, as is evident from volume rendering in Fig. 5.1a, contains many false detections.

3.3.3 Elimination of the false airways candidates

Falsely detected airways candidates are mostly formed by isolated objects not connected to a airways tree. This fact is used in their elimination; each airway candidate which is not spatially connected with detected trachea origin is considered a false detection and removed. The elimination is, thus, composed of two steps; the detection of trachea origin which is subsequently used as a seed point for following 3D region growing.

Trachea origin is detected by means of Hough transform for searching of circles used to first three slices of matrix containing airways candidates. As the most circular object in those three slices is always trachea, its origin is reliably detected. Following region growing is seeded by a binary object detected as a trachea origin which is also considered an origin of airways. Binary objects which are spatially overlapped in the following slice with the trachea origin are considered as candidates for airways continuation. A candidate is considered as airways part when two conditions are fulfilled. Firstly, overlapping area of both binary objects must be at least 10% of seed object area (10 % is relatively low value which is, however, necessary for proper connection of thin airways parts); area of an object to be connected must be, secondly, maximally 2,5 of area of seed object (due to prevention of leakage of algorithm to surrounding lung parenchyma). Each newly connected object is considered a new seed and algorithm continues until no object can be added while preserving locations of end-points of individual airways branches. In order to incorporate ascending branches, the algorithm is repeated in the opposite direction with the stored end-points used as seeds. Final airways segmentation of 80% and 20% scans are, in the further text, denoted as S_{80} and S_{20}, respectively.

4 EVALUATION OF NOISE PROPERTIES OF DATA RECONSTRUCTED BY IDOSE^4 METHOD

As stated already stated in Sec. 1.2.1, image noise is a crucial factor affecting image quality. Practically, two main types of image noise are dominant in CT data: radiological noise and streaking artifact. This study is focused only on evaluation of radiological noise in terms of its magnitude represented by standard deviation (presented in Sec. 4.2) and frequency properties represented by one-dimensional noise power spectrum (presented in Sec. 4.3). In order to evaluate radiological noise in real patient data, anatomical structures and areas where streaking artifact is dominant have to be removed (as i.e. standard deviation in locations of edges among individual tissues reflects rather the edge structure than the degree of image noise). A methodology for determination of areas of dominant radiological noise is presented in Sec. 4.1.

4.1 Determination of regions of dominant radiological noise

Data processing which leads to determination of areas with dominant radiological noise can be divided into two steps. The first step is subtraction of an image reconstructed by FBP from an image reconstructed by iDose^4 which eliminates majority of anatomical structures. Results of the subtraction are called residual noise images and their examples (which are results of subtraction of Fig. 4.1a and Fig. 4.1b - Fig. 4.1c) can be seen in Fig. 4.1e - Fig. 4.1g. The subtracted images are reconstructed by the different methods but from identical raw data, they are, thus, perfectly aligned and no registration is needed prior to the subtraction.

Majority of anatomical structures are removed in the residual noise images (e.g. in Fig. 4.1g), however streaking artifact is emphasized by the subtraction as well as edges among anatomical structures (it is obvious that iDose reconstruction changes properties of the edges compared to the FBP reconstruction). Areas where dominant streaking artifact are, as well as remaining rests of edges, in contrast to areas of dominant radiological noise, characteristic by directionality (e.g. possibility to determine direction of stripes in areas of dominant streaking artifact). The directionality is used as a feature for detection of areas of dominant radiological noise which utilizes cascade of continuous wavelet transform with directional Cauchy wavelet (described in Sec. 4.1.1) and filtering with bank of oriented anisotropic Gaussian fil-

ters (described in Sec. 4.1.2). Both methods have been sucesfully used for detection of edges, specific oriented features or corners e.g. in [115], [51], [51] and [105].

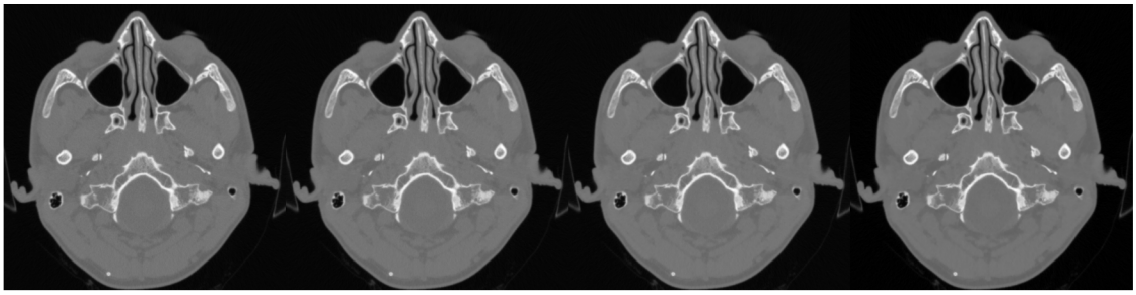

(a) (b) (c) (d)

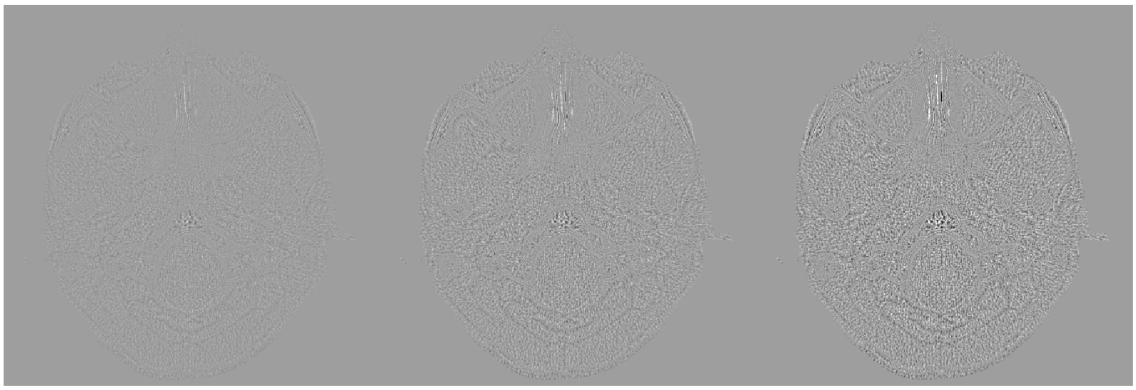

(e) (f) (g)

Obr. 4.1: Examples of residual noise images (depicted in the second row) resulting from subtraction of data reconstructed by the diverse methods (depicted in the first row): (a) slice of data reconstructed by FBP method, (b) slice of data reconstructed by iDose^4 method with level 30, (c) slice of data reconstructed by iDose^4 method with level 50, (d) slice of data reconstructed by iDose^4 method with level 70, (e) subtraction of iDose^4 level 30 and FBP reconstructions, (f) subtraction of iDose^4 level 50 and FBP reconstructions, (g) subtraction of iDose^4 level 70 and FBP reconstructions .

4.1.1 Measurement of the directionality by continuous wavelet transform with asymmetric Cauchy wavelet

One-dimensional continuous wavelet transform (CWT) is, according to [48], defined as a correlation integral between the analyzed function $s(x)$ and modified mother wavelet ψ

$$S(a,b)_{CWT} = \frac{1}{\sqrt{|a|}} \int_{-\infty}^{\infty} \psi^* \left(\frac{x-b}{a} \right) s(x) dx, \tag{4.1}$$

where * stands for complex conjugate, a for scaling parameter and b for translation parameter. Wavelets are usually designed as the fast oscillating functions of short finite support. A particular wavelet coefficient is, thus, influenced only by an interval of input signal limited by the wavelet's finite support which enables conservation of positional information after the transform. Basis of 1D CWT is formed by a family of wavelets derived from mother wavelet ψ using a translation parameter b (causes shift of a wavelet over processed signal) and a scaling parameter a (causes change of size of wavelet's support in time domain and naturally also wavelet's frequency properties in Fourier domain). Result of 1D CWT is a time-scale analysis (similar to a time-frequency analysis obtained by a short-time Fourier transform) which is suitable for processing and analysis of non-stationary signals [48], [3].

Two-dimensional CWT is a simple generalization of Eq. 4.1 with exactly the same properties [3]

$$S(a, \boldsymbol{b}) = \frac{1}{a} \int \psi^* \left(\frac{(\boldsymbol{x} - \boldsymbol{b})}{a} \right) s(\boldsymbol{x}) d^2\boldsymbol{x}, \tag{4.2}$$

where analyzing wavelet is translated by a vector $\boldsymbol{b}$ of translations in x and y directions [122]. Formula Eq. 4.2 applies only for two-dimensional rotation invariant wavelets, anisotropic wavelets requires additional parameter to be considered which is a rotation angle θ

$$S(a, \theta, \boldsymbol{b}) = \frac{1}{a} \int \psi^* \left(\frac{r_{-\theta}(\boldsymbol{x} - \boldsymbol{b})}{a} \right) s(\boldsymbol{x}) d^2\boldsymbol{x}, \tag{4.3}$$

where $r_{-\theta}$ is 2×2 rotation matrix Eq. 4.8. The transformation is now local in four parameters $a, \boldsymbol{b}, \theta$. Detection of the oriented structures requires utilization of a wavelet with directionally selective properties. A wavelet is directional if support of its Fourier transform is contained in a convex cone in spatial frequency domain with apex located in origin of coordinate system [1].

A family of directional Cauchy wavelets, introduced in [1], has been chosen to process residual noise images. Let $\mathcal{C} \equiv \mathcal{C}(\alpha, \beta)$ be the convex cone delimited by the unit vectors $\vec{e}_\alpha$ and $\vec{e}_\beta$, where $\alpha < \beta$, $\beta - \alpha < \pi$ with axis $\vec{\xi}_{\alpha\beta}$, and $\widetilde{\mathcal{C}}$ the dual cone with the identical axis. Fourier transform of two-dimensional Cauchy wavelet with support in $\mathcal{C}(\alpha, \beta)$ for any $\vec{k} \in \mathcal{C}$, $\vec{\eta} \in \widetilde{\mathcal{C}}$ and l, n is, according to [2], defined as

$$\widehat{\psi}_{lm}^{(\mathcal{C},\vec{\eta})}(\vec{k}) = \begin{cases} \left(\vec{k} \cdot \vec{e}_{\widetilde{\alpha}}\right)^l \left(\vec{k} \cdot \vec{e}_{\widetilde{\beta}}\right)^m e^{-\vec{k}\cdot\vec{\eta}}, & \vec{k} \in \mathcal{C}(\alpha, \beta), \\ 0, & \text{otherwise}, \end{cases} \tag{4.4}$$

and in spatial domain as

$$\psi_{lm}^{(\mathcal{C},\vec{\eta})}(\vec{x}) = \frac{i^{l+m+2}}{2\pi} l!m! \frac{\left[\sin(\beta - \alpha)\right]^{l+m+1}}{\left[(\vec{x} + i\vec{\eta}) \cdot \vec{e}_\alpha\right]^{l+1} \left[(\vec{x} + i\vec{\eta}) \cdot \vec{e}_\beta\right]^{m+1}}. \tag{4.5}$$

Tab. 4.1: Setting of parameters of graph-cut based segmentation of directional structures in residual noise data. The parameters are consistent with Tab. 3.2.

	μ	σ_A	σ_B	λ	σ
2D CWT (oriented Cauchy wavelet)	0.85	0.1	0.1	10	2
Oriented anisotropic Gaussian	5	2	2	10	0.5

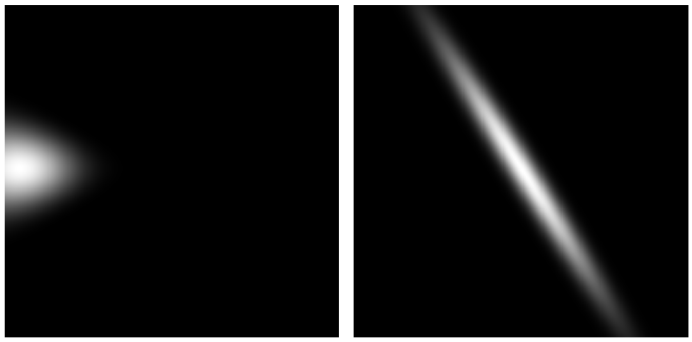

(a) (b)

Obr. 4.2: Examples of moduli of frequency characteristics of a directional Cauchy wavelet and an oriented anisotropic Gaussian filter: (a) modulus of frequency characteristic of Cauchy wavelet with parameters $\theta = 0$ and $a = 1$, (b) modulus of frequency characteristic of oriented anisotropic Gaussian filter with parameters $\sigma_u = 7$, $\sigma_v = 0.7$ and $\theta = 42/128\pi \approx 59°$.

2D CWT utilizing a Cauchy wavelet with a single dilatation $a = 1$ and 16 equally spaced orientations $\theta = \langle 0, \pi/16, \ldots, 14/16\pi, 15/16\pi \rangle$ is applied on each slice of residual noise data. 16 results are, thus, obtained in which differently oriented structures, correlating with the wavelet, are enhanced. Residual noise image Fig. 4.1g filtered by the oriented Cauchy wavelet (modulus of respective frequency characteristic can be seen in Fig. 4.2a) is depicted in Fig. 4.3a, where the structures oriented in parallel with y axis are, correctly, highly emphasized. A final parameter indicating whether the individual voxel belongs to a directional structure is calculated as a range of absolute values of 16 CWT coefficients representing results of filtering in all considered 16 directions. Obtained parametric map (depicted in Fig. 4.3b) is segmented by a graph-cut based method (described in Sec. 3.2.3) with heuristically adjusted priors summarized in Tab. 4.1; binary objects with size lower than 10 pixels are removed using morphological area opening.

A final detection of directional structures in residual noise image Fig. 4.1g is depicted in Fig. 4.3c where the voxles classified as parts of directional structures are labeled by zeros. Areas of dominant streaking artifact (located in the middle

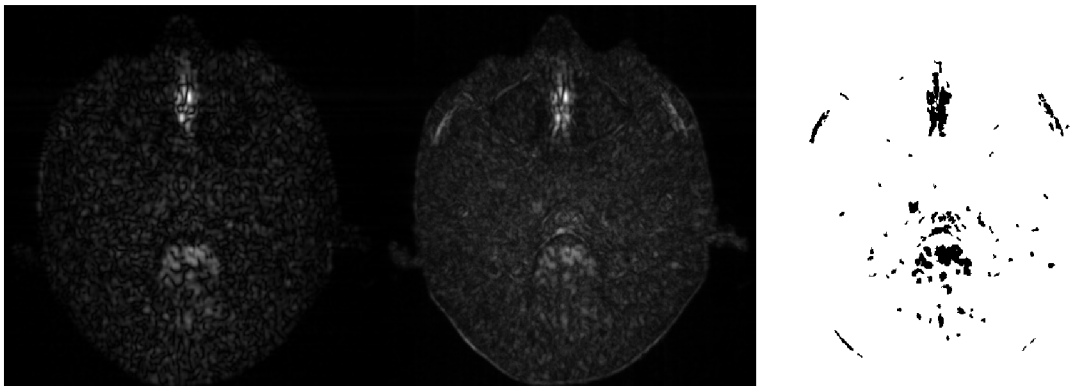

(a) (b) (c)

Obr. 4.3: Exemplary result of 2D CWT based detection of directional structures in residual noise image Fig. 4.1g: (a) 2D CWT coefficients resulting from filtering with Cauchy wavelet oriented in parallel with y axis, (b) range of absolute values of 2D CWT coefficients resulting from filtering with 16 differently oriented Cauchy wavelets, (c) graph-cut based segmentation of Fig. 4.3b; a final 2D CWT based detection of directional structured in residual noise data.

of Fig. 4.1g) and majority of distinct rests of edges are reliably detected. However, some directional structures, especially rests of edges between adipose and soft tissue, which are faintly correlated with oscillating character of Cauchy wavelet remains undetected. Detection of those directional structures must be performed by a different method (filtering by two-dimensional oriented anisotropic Gaussian filter described in Sec. 4.1.2).

4.1.2 Measurement of the directionality using oriented anisotropic Gaussian filters

Oriented two-dimensional anisotropic Gaussian filter which, according to [27], allows for generation of edge and ridge maps with high spatial and angular accuracy, is a generalization of classical isotropic Gaussian filter given by

$$g(x, y; \sigma) = \frac{1}{2\pi\sigma^2} \cdot \exp\left\{-\frac{1}{2}\left(\frac{x^2 + y^2}{\sigma^2}\right)\right\}, \tag{4.6}$$

where σ stands for standard deviation. Anisotropy of a Gaussian filter is forced by setting of different standard deviations σ_x, σ_y in x and y spatial coordinates, respectively. Hence, Eq. 4.6 can be rewritten to

$$g_{\perp}(x, y; \sigma_x, \sigma_y) = \frac{1}{2\pi\sigma_x\sigma_y} \cdot \exp\left\{-\frac{1}{2}\left(\frac{x^2}{\sigma_x^2} + \frac{y^2}{\sigma_y^2}\right)\right\} \tag{4.7}$$

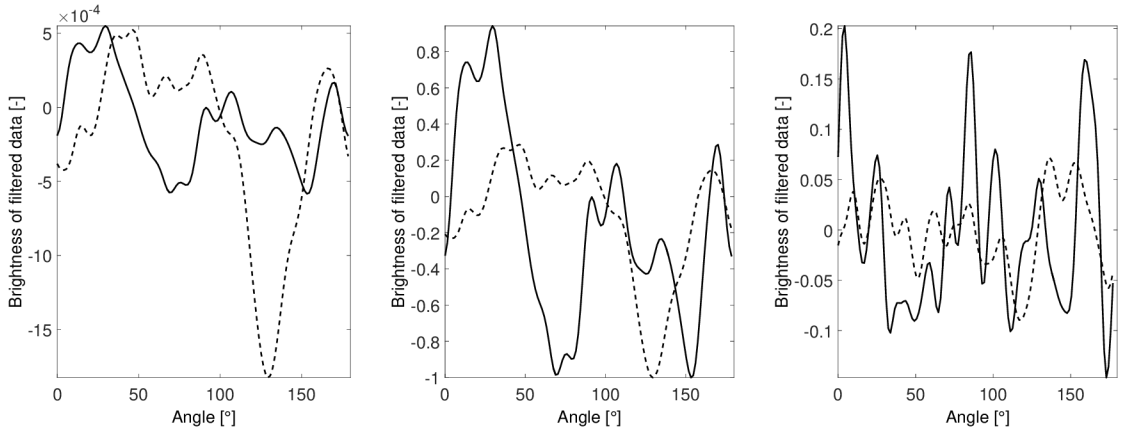

(a) (b) (c)

Obr. 4.4: Stages of directionality parameter derivation from results of filtering with bank of 128 oriented anisotropic Gaussian filters. Vectors derived from voxel which is a typical representative of directional structure are delineated by dashed lines (– – –) and vectors derived from voxel which is a typical representative of radiological noise are delineated by solid lines (——): (a) results of filtering with a bank of oriented anisotropic Gaussian filter, (b) result of normalization by the maximum of element's absolute values, (c) difference of (b).

[27]. Different σ_x, σ_y forces elliptical shape to a Gaussian with axes parallel to the coordinate system. Incorporation of rotation of coordinate system (x, y) over Θ,

$$\begin{pmatrix} u \\ v \end{pmatrix} = \begin{bmatrix} \cos\Theta & \sin\Theta \\ -\sin\Theta & \cos\Theta \end{bmatrix} \cdot \begin{pmatrix} x \\ y \end{pmatrix}, \tag{4.8}$$

results, according to [27], to a formula of general oriented anisotropic Gaussian filter

$$g_\Theta(u, v; \sigma_u, \sigma_v, \Theta) = \\ = \frac{1}{2\pi\sigma_u\sigma_v} \cdot \exp\left\{-\frac{1}{2} \cdot \left(\frac{(x\cos\Theta + y\sin\Theta)^2}{\sigma_u^2} + \frac{(-x\sin\Theta + y\cos\Theta)^2}{\sigma_v^2}\right)\right\}, \tag{4.9}$$

with u axis oriented in parallel with Θ and axis v oriented orthogonally.

A bank of oriented anisotropic Gaussian filters with constant parameters $\sigma_u = 7$, $\sigma_v = 0.7$ and variable orientation $\Theta = \langle 0, \pi/128, \ldots, 126/128\pi, 127/128\pi\rangle$ produces 128 parametric maps where differently oriented structures are enhanced. Residual noise image Fig. 4.1g filtered by the filter with $\Theta = 42/128\pi \approx 59°$, whose modulus of frequency characteristic is depicted in Fig. 4.2b, can be seen in Fig. 4.5a, where structures oriented perpendicularly to Θ are highly emphasized.

Each voxel is, thus, represented by a vector with 128 values depending on Θ and a single parameter describing the directionality needs to be derived. Examples

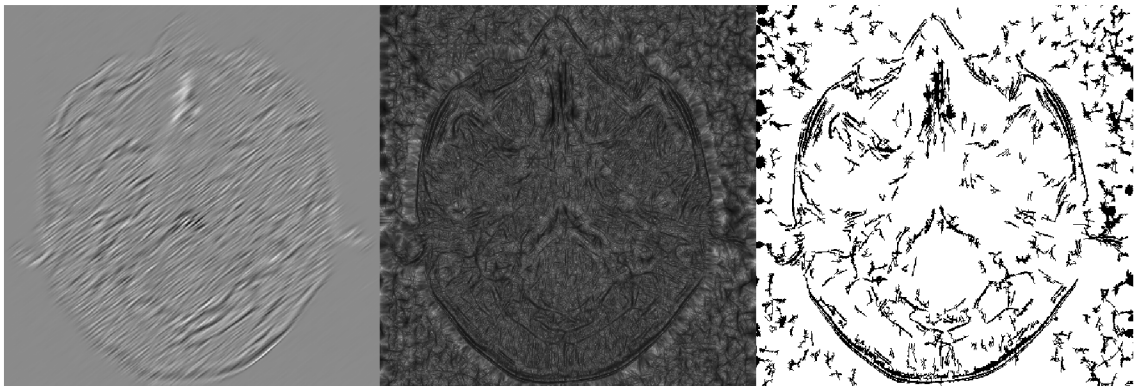

(a) (b) (c)

Obr. 4.5: Exemplary result of oriented anisotropic Gaussian filtering based detection of directional structures in residual noise image Fig. 4.1g: (a) the residual noise image filtered by anisotropic Gaussian filter with $\Theta = 42/128\pi \approx 59°$, (b) directionality map calculated from 128 results of the filtering, (c) final oriented anisotropic Gaussian filtering based detection of directional structures in residual noise data.

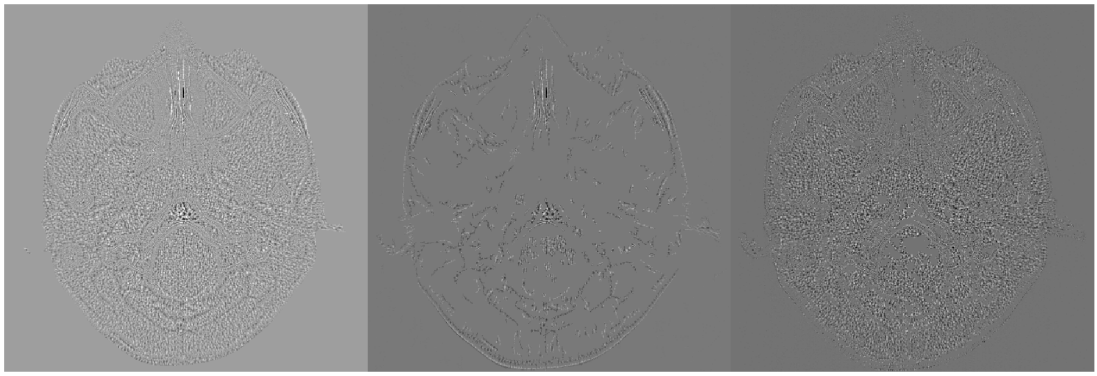

(a) (b) (c)

Obr. 4.6: Detection of area of dominant radiological noise in a residual noise image: (a) a residual noise image (identical with Fig. 4.1g repeated here for possibility of direct comparison), (b) detected directional structures, (c) detected areas of dominant radiological noise (images (b) and (c) are multiplied with the residual noise image).

of two vectors belonging to voxels which are typical representatives of directional structure (dashed line (− − −)) and radiological noise (solid line (——)) are depicted in Fig. 4.4a. Oriented structures have, naturally, a single distinctive response in a limited range of angles Θ, whereas responses of the filtering of radiological noise do not contain any distinctive peak and are highly fluctuating. The vectors are, firstly,

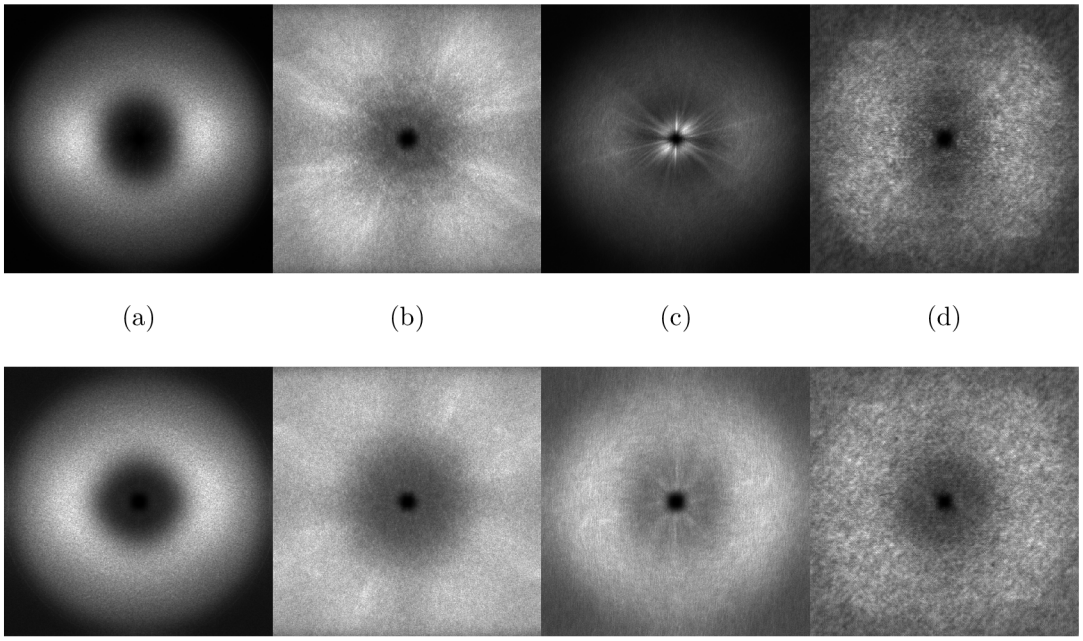

(a) (b) (c) (d)

(e) (f) (g) (h)

Obr. 4.7: Effect of detection of regions of dominant radiological noise to rotational symmetry of tissue 2D noise power spectra: First row: tissue 2D NPS of residual noise images. Second row: tissue 2D NPS of residual noise calculated only from detected areas of dominant radiological noise. (a), (e) 2D NPS of soft tissue, (b), (f) 2D NPS of bones, (c), (g) 2D NPS of adipose tissue, (d), (h) 2D NPS of air filled tissue.

normalized by the maximum of absolute values of their elements, which relatively decreases (due to presence of single distinctive peak) magnitudes in vectors representing directional structures and, on the other hand, emphasizes nearly steady values of vectors representing radiological noise (example vectors after the normalization are depicted in Fig. 4.4b). Normalized vectors are, subsequently, differentiated to enhance fluctuating character of vectors representing radiological noise (see result in Fig. 4.4c) and the final parameter describing the directionality is calculated as a sum of absolute values of the differences. Calculated directionality of the examples presented in Fig. 4.4 are 8.4 for voxel representing radiological noise and 3.8 for voxel representing a directional structure.

A resulting parametric map describing the directionality, see example in Fig. 4.5b, is finally segmented using graph-cut based method with settings summarized in Tab. 4.1. Binary objects with size lower than 25 pixels are, subsequently, removed using morphological area opening. A final binary segmentation which determines areas of dominant radiological noise in residual noise images is obtained as union of

the both partial results.

Detection of areas of dominant radiological noise turned out to be extremely useful for estimation of tissue noise power spectra. As already mentioned, radiological noise should have, theoretically, rotationally symmetric 2D NPS. 2D tissue noise power spectra, details about its calculation can be found in Sec. 4.3.1, of an exemplary residual noise image are depicted in the first row of Fig. 4.7, while 2D tissue NPS of identical data after elimination of the detected directional structures are depicted in the second row of Fig. 4.7. There is an evident improvement of 2D NPS rotational symmetry for each considered tissue when 2D NPS is calculated only from detected areas of dominant radiological noise.

4.2 Quality evaluation by standard deviation of residual noise

A basic parameter which can be extracted from residual noise images is their standard deviation which describes magnitude of statistical fluctuations caused by CT radiological noise. Because of necessary subtraction of differently reconstructed data, standard deviation of residual noise is not a direct measure of noise properties and it is interpreted using a following test performed on a subset of real patient data.

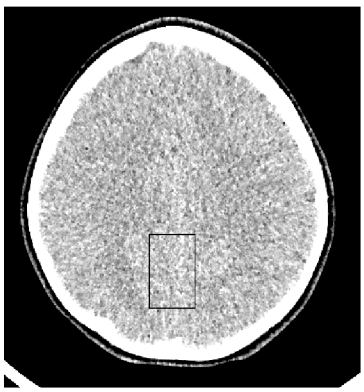

Obr. 4.8: Slice of brain scan reconstructed by iDose[4] level 70 with homogeneous part delineated by a black rectangle.

A region of interest (ROI) is manually selected in order to define an area of brain, which is considered homogeneous. Intensity changes in these ROIs are, therefore, considered being only random noise patterns, see sample in Fig. 4.8. Two parameters are computed from each ROI of iteratively reconstructed data, a cross covariance with the identical ROI selected from the FBP reconstruction ($C_{X,FBP}$) and a standard deviation (σ_X^2). The results are summarized in Tab. 4.2.

Subtraction of the two random variables FBP and X (X is meant as a particular iDose^4 reconstruction), having variances σ^2_{FBP} and σ^2_X and cross-covariance $C_{X,FBP}$, results in new random variable with a standard deviation equal to Eq. 4.10.

$$\sigma_{(X-FBP)} = \sqrt{\sigma^2_{FBP} + \sigma^2_X - 2.C_{X,FBP}} \tag{4.10}$$

Tab. 4.2: Comparisons of theoretically determined $\sigma_{(X-FBP)}$ and practically measured $\sigma_{E(X-FBP)}$ standard deviations of residual noise.

Recon. (X)	$C_{X,FBP}$	σ^2_X	$\sigma_{(X-FBP)}$	$\sigma_{E(X-FBP)}$
FBP	-	16.63	-	-
ID30	234.09	14.12	2.78	2.77
ID50	200.31	12.19	4.95	4.95
ID70	158.81	9.97	7.64	7.64

A standard deviation of residual noise in investigated ROIs $\sigma_{E(X-FBP)}$ is computed from real data and compared with values obtained from equation Eq. 4.10. The results summarized in Tab. 4.2 proves, as values $\sigma_{E(X-FBP)}$ and $\sigma_{(X-FBP)}$ are nearly identical, that Eq. 4.10 is applicable to analysis of standard deviation of residual noise images. The standard deviation of residual noise, therefore, depends only on a standard deviation of noise in image X and a cross-covariance between noise in images FBP and X.

According to Tab. 4.2, standard deviation of residual noise increases with decreasing cross-covariance $C_{FBP,X}$ and increasing difference between σ^2_{FBP} and σ^2_X. It, thus, can be considered a valuable measure indicating improvement of noise properties in images reconstructed by iDose^4 compared to images reconstructed by FBP. Advantage of this parameter lies in independence on an imaged object, therefore, it can be directly applicable to real patient data not only to imaged phantoms. On the other hand, it provides only relative improvement of noise properties with respect to by FBP reconstructed data.

4.3 Evaluation of stability of noise frequency properties among FBP and iDose reconstructions

As already mentioned, iDose^4 reconstruction method aims at lowering the level of image noise with preservation of look and feel of conventionally reconstructed images. Preservation of frequency properties of image noise in iteratively reconstructed images, compared with the conventionally reconstructed ones, is very important

for their conventional look and also for diagnostic purposes (radiologists are used to diagnose from images with FBP-like noise).

Hence, the objective of this study is to extract a parameter, which describes noise frequency properties, from real patient data and subsequently to assess how does the iDose^4 reconstruction method influence the noise spectral characteristics compared with FBP reconstruction. A 1D NPS is used, as it provides a complex spectral characteristic of radiological noise in CT data. A single parameter, center of gravity (CoG) of 1D NPS calculated according to

$$CoG = \frac{\sum xf(x)}{\sum f(x)}, \tag{4.11}$$

where x is a frequency axis normalized by a Nyquist frequency and $f(x)$ represents 1D NPS curve, is extracted from each 1D NPS. A final parameter $\overline{CoG}$ (called stability index), which serves as the measure of change of noise frequency properties among the reconstructions, is defined as

$$\overline{CoG}_{iDose} = 100\,|CoG_{FBP} - CoG_{iDose}| \tag{4.12}$$

and express percentage absolute difference between center of gravity of 1D NPS of noise in by FBP and iDose^4 reconstructed data.

Prior to evaluation of stability of noise frequency properties in real patient data, identical analysis is performed on homogeneous (water filled) areas of scanned standard CT calibration phantom where only a radiological noise is present (procedure of extraction of the phantom's homogeneous parts is described in Sec. 4.3.2). Results of the stability measurements performed on the phantom scans will be further used for validation of the results extracted from real patient data.

As stated in Sec. 4.1, subtraction of differently reconstructed data is an essential step in evaluation of noise properties in real patient CT data. An analysis of influence of the subtraction on the position of 1D NPS center of gravity is, thus, performed on the phantom scans. The 1D NPS CoGs are calculated from the original data (which is allowed by homogeneity of a water filled part of imaged phantom) and from subtracted data (reconstruction ID 70 is, this time, subtracted from rest of the reconstructions). Errors in CoG of 1D NPS estimation caused by subtraction of differently reconstructed noise matrices are, according to Tab. 4.3, approximately one percent of the considered frequency range.

A similar analysis is performed for stability indexes calculated according to Eq. 4.12 again for original and subtracted noise matrices. According to the results summarized in Tab. 4.4, subtraction of a noise matrix reconstructed by iDose^4 level 70 have low impact to accuracy of stability index calculation (maximal error is 0.07 %). Residual noise images, thus, can be used for evaluation of noise frequency properties stability in real patient data.

Tab. 4.3: CoGs of 1D NPS calculated from homogeneous parts of scanned phantoms reconstructed by diverse methods. The CoGs calculated from original data are in the first row, whereas the CoGs calculated from data when a scan reconstructed by iDose[4] level 70 is subtracted are in the second row.

	FBP	ID 30	ID 50	ID 70
COG_{Orig}	0.588	0.587	0.586	0.584
COG_{Sub}	0.597	0.597	0.596	-

Tab. 4.4: Stability indexes of iDose level 30 and 50 reconstructions computed from original (not subtracted) and subtracted noise matrices.

	ID 30	ID 50
$\overline{COG}_{Orig}[\%]$	0.28	0.43
$\overline{COG}_{Sub}[\%]$	0.21	0.46

Besides evaluation of errors introduced by subtraction of noise matrices, another influences have to be inspected. Firstly, equation of NPS computation Eq. 1.5 is adapted to be consistent with character of segmented residual noise images in Sec. 4.3.1. Secondly, estimation of 1D NPS in separate tissues is inevitably loaded by errors caused by spectral leakage. Magnitudes of those errors are evaluated in Sec. 4.3.3 and a methodology for their reduction is presented in Sec. 4.3.4.1.

4.3.1 Tissue noise power spectrum

Eq. 1.5 assumes that the noise matrix $\mathbf{D}(x, y)$ is fully filled with measured noise; however, this premise is not fulfilled in case of segmented residual noise images, since they contain many zero elements not contributing to computation of 2D NPS. Normalization of 2D NPS must therefore be reformulated and Eq. 1.5 is changed to

$$\mathbf{S}(f_x, f_y) = \frac{b_x b_y}{L_B} \cdot \left\langle \left| DFT_{2D} \left\{ \mathbf{D}(x, y) - \mathbf{D}_{filt}(x, y) \right\} \right|^2 \right\rangle, \tag{4.13}$$

where the normalization term L_B correspond to total sum of pixels contributing to computation of 2D NPS. L_B can be computed as sum of squared elements of the corresponding segmentation mask $\mathbf{B}$, which, as will be shown later, need not necessarily be binary

$$L_B = \sum_{x=1}^{L_x} \sum_{y=1}^{L_y} \mathbf{B}(x, y)^2 \tag{4.14}$$

Multiplying of residual noise images with segmentation masks and also with mask of detected areas of dominant radiological noise is necessary to evaluate noise properties in separate tissues; however it inevitably introduces errors to estimation of 1D NPS. According to convolutional property of Fourier transform (Eq. 4.15 [48]), multiplication of two signals in the original domain corresponds to convolution of their spectra in the frequency domain

$$FT\left\{f(x,y)g(x,y)\right\} = \frac{1}{4\pi^2}F(f_x,f_y)^*G(f_x,f_y). \tag{4.15}$$

The NPS of residual noise estimated by Eq. 4.13 is therefore a convolution of the sought noise power spectrum and the spectrum of a weighting segmentation mask, which causes errors in estimation of 2D- and consequently of radial 1D noise power spectrum.

Magnitudes of errors introduced by the segmentation (abbreviation SIE as a short for segmentation introduced error is introduced) must be evaluated prior to computation of 1D NPS of a real patient data. A matrices filled by simulated noise with exactly known noise power spectra, a process of CT noise simulation is described in Sec. 4.3.2, serves as gold standards needed for the errors evaluation. A methodology for evaluation of errors in 1D NPS estimation introduced by a tissue segmentation is described in Sec. 4.3.3.

4.3.2 Simulation of CT noise

To be able to compute errors of 1D NPS estimation caused by tissue segmentation, a matrices filled by simulated noise with exactly known 1D NPS must be created. A matrices sized $512 \times 512 \times X$ voxels (where X stands for number of slices in a considered data) filled with zero-mean white noise are generated. The statistical noise inherent to CT data is not typically white [11]; therefore, the generated noise need to be colored (its spectral envelope must be modulated). The function for spectral envelope modulation is extracted from homogeneous (water filled) area of the scanned standard CT calibration phantom, an example can be seen in Fig. 4.9a. The largest square fitted into the circle with lowest diameter (i.e. inner edge of phantom's case) detected by Hough transform [19] is selected from each slice, see example of selected area of pure radiological noise in Fig. 4.9b. The 1D noise power spectrum is subsequently computed from such selected homogeneous area and interpolated to a desired length of 512 samples. The one-dimensional spectral modulation function is, thus, known and subsequently rotationally extended to the two-dimensional modulation function MOD_{2D}. Coloring of the 3D white noise matrices is undertaken in frequency domain according to

$$N_{Col} = IDFT_{2D}\{DFT_{2D}\{N_{White}\} \cdot MOD_{2D}\} \tag{4.16}$$

applied slice by slice, where N_{White} stands for matrix filled by white noise. Finally, the required 3D colored noise matrix N_{Col}, a single slice is depicted in Fig. 4.9d, is obtained.

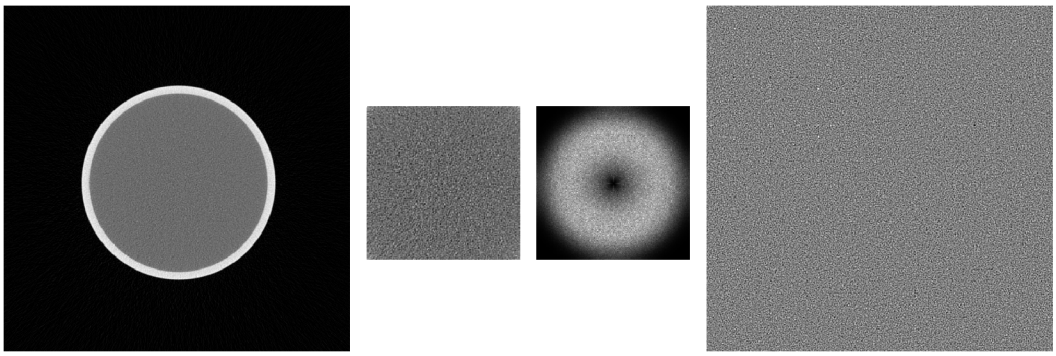

(a) (b) (c) (d)

Obr. 4.9: Simulation of radiological CT noise: (a) CT image of a standard water filled calibration phantom, (b) sub-figure cropped from (a) containing pure radiological noise, (c) 2D power spectrum of CT noise extracted from phantom's homogeneous parts, (d) matrix filled by noise with power spectrum typical for CT radiological noise.

4.3.3 Evaluation of errors in estimation of 1D NPS forced by tissue segmentation

As already mentioned, stability indexes of iDose[4] reconstructions will be evaluated using calculation of center of gravity of tissue noise power spectrum. The objective of this section is to evaluate how are CoGs of 1D NPS influenced by tissue segmentation. The noise matrices, simulated in the previous section, have their noise power spectra exactly defined by the modulation function and the segmentation introduced errors can, hence, be evaluated. As 1D NPS center of gravity of generated noise matrix CoG_{GS} is exactly known, it serves as a gold standard. 1D NPS CoG of identical noise matrix weighted by e.g. binary mask for bones segmentation is denoted as CoG_{Bones}. Segmentation introduced error expressed in percents (SIE_{Bones}) is than calculated by

$$SIE_{Bones} = 100\,|CoG_{GS} - CoG_{Bones}|\,. \tag{4.17}$$

Results of measuring of errors in CoGs of 1D NPS estimation introduced by segmentation of diverse tissues are summarized in Tab. 4.5. It can be concluded that tissue segmentation significantly influences precision of the CoGs estimation

Tab. 4.5: Means and standard deviations of errors in estimation of CoGs of 1D noise power spectra introduced by tissue segmentation calculated from a whole set of 33 scans.

	Soft tissue	Bones	Adipose tissue	Air filled structures
mean SIE [%]	0.204	0.404	0.959	0.973
std SIE [%]	0.035	0.106	0.403	0.375

especially considering tissues with relatively low spatial extent (i.e. adipose and air filled tissues) where mean SIE is aprroximatelly 1% of considered frequency range. A methodology for SIE lowering, which, as will be shown, can potentially be useful in other applications where a frequency spectrum has to be calculated from regions with irregular shape, is presented in Sec. 4.3.4.1.

4.3.4 Two-dimensional spatially adaptive windowing functions

The errors in 1D NPS estimation caused by tissues segmentation are predominantly caused by two effects. Noise power spectra are, firstly, calculated from substantially lower number of voxels, estimation, thus, can not be precise. The second effect is spectral leakage well known from one-dimensional signal processing where shortening of theoretically infinite signal by a rectangular window cause decrease of frequency resolution as spectrum of signal is convolved with spectrum of rectangular weighting window (i.e. sinc function). Undesirable effect of leakage in spectral domain is usually reduced either by prolonging a window length or using window with better spectral properties. Analogically, a binary segmentation mask can be, in this application, viewed as two dimensional rectangular weighting window with spatially adaptive shape. Shape of a binary segmentation mask is restricted by delineation of tissues in real patient data, prolonging of window length, therefore, can not be used. Problem of reduction of effect of spectral leakage is, hence, solved by design of two-dimensional windowing functions commonly used in signal processing (e.g. Hann or Hamming) whose shape is adaptable to a the shape of a segmented binary objects. Those functions are named two-dimensional spatially adaptive windowing functions (2D SAW).

4.3.4.1 Design of 2D SAW

Common one-dimensional weighting windows are real, even, non-negative and time limited functions of one variable n (index of sample in the window) and one para-

meter N (width of windowing function) such as e.g. Eq. 4.18 for computation of the Welch window [116].

$$w(n) = 1 - \left(\frac{n - \frac{N-1}{2}}{\frac{N-1}{2}} \right)^2 . \tag{4.18}$$

Situation is rather complicated in two dimensions especially due to locally varying width of binary objects, as e.g. binary object depicted in Fig. 4.10a which serves as an example for 2D SAW design demonstration. N is no longer a parameter in two-dimensional space and becomes a variable reflecting unequal shape of binary objects. The variable n can be, in two-dimensional case, easily represented by values of Euclidean distance map calculated according to [99] by

$$D(f)\Big|_{i,k} = \min \left\{ d_e \left((i,k), (m,n) \right) \Big| f_{m,n} = 0 \right\}, \tag{4.19}$$

which for each active (nonzero) pixel $f_{i,k}$ calculates Euclidean distance d_e to the nearest zero-valued pixel $f_{m,n}$. Example of an Euclidean distance map, which also represents distribution of n variable, of test binary object Fig. 4.10a is depicted in Fig. 4.10b. The problem is, thus, reduced to determination of the variable N. The two main approaches are presented, first utilizes map of local thicknesses of a binary object published in [42] and the second, proposed in this thesis, utilizes a binary object's medial axis. The latter, medial axis based, approach moreover allows for optimization of 2D SAW design.

N represented by distribution of local thicknesses

The first choice for determination of the variable N of a binary object is its distribution of local thicknesses proposed in [42] for measurement of trabercular thicknesses in a data acquired by 3D micro-computed tomography system. The method comprises two main steps, a medial axis transform (MAT) of a binary object under consideration is firstly determined which is subsequently utilized for determination of local thicknesses.

Medial axis transform $MAT(X)$ is, according to [9], a particular description of a shape defined as a set of ordered pairs of centers and radii of maximal disks in the planar shape X [16]

$$MAT(X) = \{(\mathbf{x}, r) \in F | B(\mathbf{x}, r) \in \text{MaxDisk}\,(X)\}, \tag{4.20}$$

where MaxDisk is a set of maximal disks in the planar shape X and $B(\mathbf{x}, r)$ denotes particular maximal disk with radius r centered at $\mathbf{x}$.

Disk B, inscribed into a object, is maximal if there is no other inscribed disk which contains disk B. In other words, maximal disk of object X, with center in

position $\mathbf{x}$, must touch object's border in two sufficiently distinct points $\mathbf{y_1}$ and $\mathbf{y_2}$. Minimum distance between the two contour points for considering a disk to be maximal is determined by a parameter ρ. Formally, a maximal disk of an object X with center in a point $\mathbf{x}$ (the part of medial axis $MAT(X)$) can be expressed by a formula

$$\begin{aligned} \mathbf{x} \in MAT(X) \Leftrightarrow \exists\, \mathbf{y_1}, \mathbf{y_2} \in \delta X \mid d_e(\mathbf{y_1}, \mathbf{y_2}) \geqslant \rho \text{ and} \\ d_e(\mathbf{x}, \delta X) = d_e(\mathbf{x}, \mathbf{y_1}) = d_e(\mathbf{x}, \mathbf{y_2}), \end{aligned} \tag{4.21}$$

where δX denotes the boundary of X and d_e expresses Euclidean distance [16], [99]. Local thicknesses at point $\mathbf{x} \in X$ is than defined by

$$Th(X)(\mathbf{x}) = 2 \max \{r | \mathbf{x} \in B(\mathbf{x}, r), \forall B(\mathbf{x}, r) \subseteq X\}, \tag{4.22}$$

hence, it is equal to diameter of the largest maximal disk centered at any point of medial axis that includes $\mathbf{x}$ [80]. Local thicknesses distribution of the exemplary binary object Fig. 4.10a is depicted in Fig. 4.10c.

The final 2D spatially adaptive window is calculated by substituting determined variables n and N into the one-dimensional formula calculating half (from ridge to border) of windowing function. One-dimensional Welch windowing function Eq. 4.18 is, thus, changed to

$$w(n) = 1 - \left(\frac{n - N}{N} \right)^2. \tag{4.23}$$

Resulting Welch type 2D SAW of the object Fig. 4.10a with the variable N represented by distribution of local thicknesses can be seen in Fig. 4.10d.

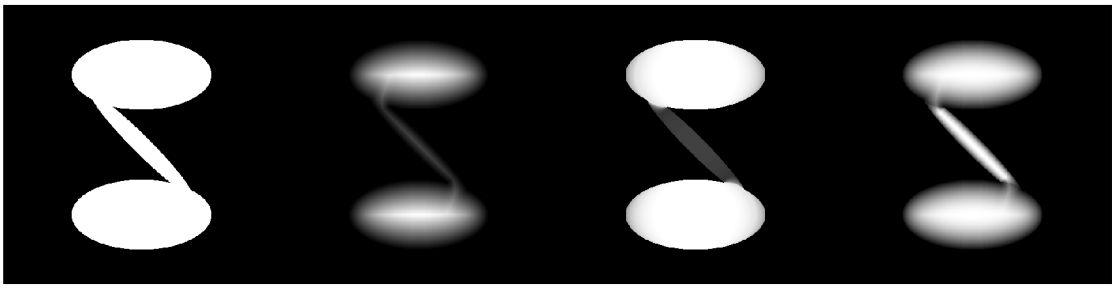

(a) (b) (c) (d)

Obr. 4.10: Local thickness based design of two-dimensional spatially adaptive windowing function: (a) test binary image formed by union of three binary ellipses, (b) Euclidean distance map of Fig. 4.10a, (c) maximal disks based distribution of local thicknesses, (d) two-dimensional spatially adaptive Welch type window with local thicknesses distribution substituted by N in Eq. 4.23.

Sharp transitions of local thicknesses in locations where objects of different sizes intersect evidently cause undesirable discontinuities in a final 2D SAW. Another approach to determination of the N variable, this time based on Euclidean distance maps and maximal disks based medial axis transform, is, thus, presented.

Medial axis transform based N determination

Another approach to N determination is based on the following assumption: for a given point $\mathbf{x} \in X$ half of its local thickness can be estimated as a sum of its distance to a closest contour point and distance to a closest point of object's medial axis, provided that medial axis describes only object's basic shape. Medial axis based approach to 2D SAW design is demonstrated on a binary object with a simple elliptic shape (lengths of major and minor axis are 384 px and 256 px, respectively, in 512×512 px sized image, see Fig. 4.11a) with heuristically determined medial axis (181 px long; centered on object's major axis, see Fig. 4.11b where the medial axis is indicated by a black line (i.e. without any information about diameters of maximal discs)). Distance to the closest contour point can be easily represented by classical Euclidean distance map according to Eq. 4.19; the result is depicted in Fig. 4.11c. Map of distances to the closest point of a medial axis can be effectively obtained by placing set of ones representing medial axis g onto a zero background and calculating inverse distance map (for each zero pixel calculate distance to closest active pixel) according to

$$\tilde{D}(g)\Big|_{i,k} = \min\left\{ d_e\left((i,k),(m,n)\right) \Big| g_{m,n} = 1 \right\}. \tag{4.24}$$

Corresponding map of distances to the closest points of a medial axis can be seen in Fig. 4.11d. Schematic representation of medial axis based local thickness calculation for the single pixel (marked by solid line circle) is depicted in Fig. 4.11b, where the local thickness is sum of two distances $D(f)\Big|_{i,k}$ and $\tilde{D}(g)\Big|_{i,k}$ marked by arrows. A final medial axis based map of local thicknesses can be seen in Fig. 4.11e and corresponding Welch type 2D SAW in Fig. 4.11f.

Sum of two linear functions with equal but mutually opposite slopes gives a constant function with magnitude equal to sum of their y-intercepts. Both considered distance functions have opposite slopes (see dashed and doted lines in Fig. 4.11g and Fig. 4.11h where cross-sections of figures from Fig. 4.11c to Fig. 4.11f are plotted), the resulting constant function, thus, correspond to a local thickness (see dash-dotted lines in Fig. 4.11g and Fig. 4.11h).

The classical maximal disks based local thickness calculation, as described in [42], tends to overestimate local thicknesses in several parts of binary objects. The local thickness of the considered point in Fig. 4.11b is, according to [42], a diameter

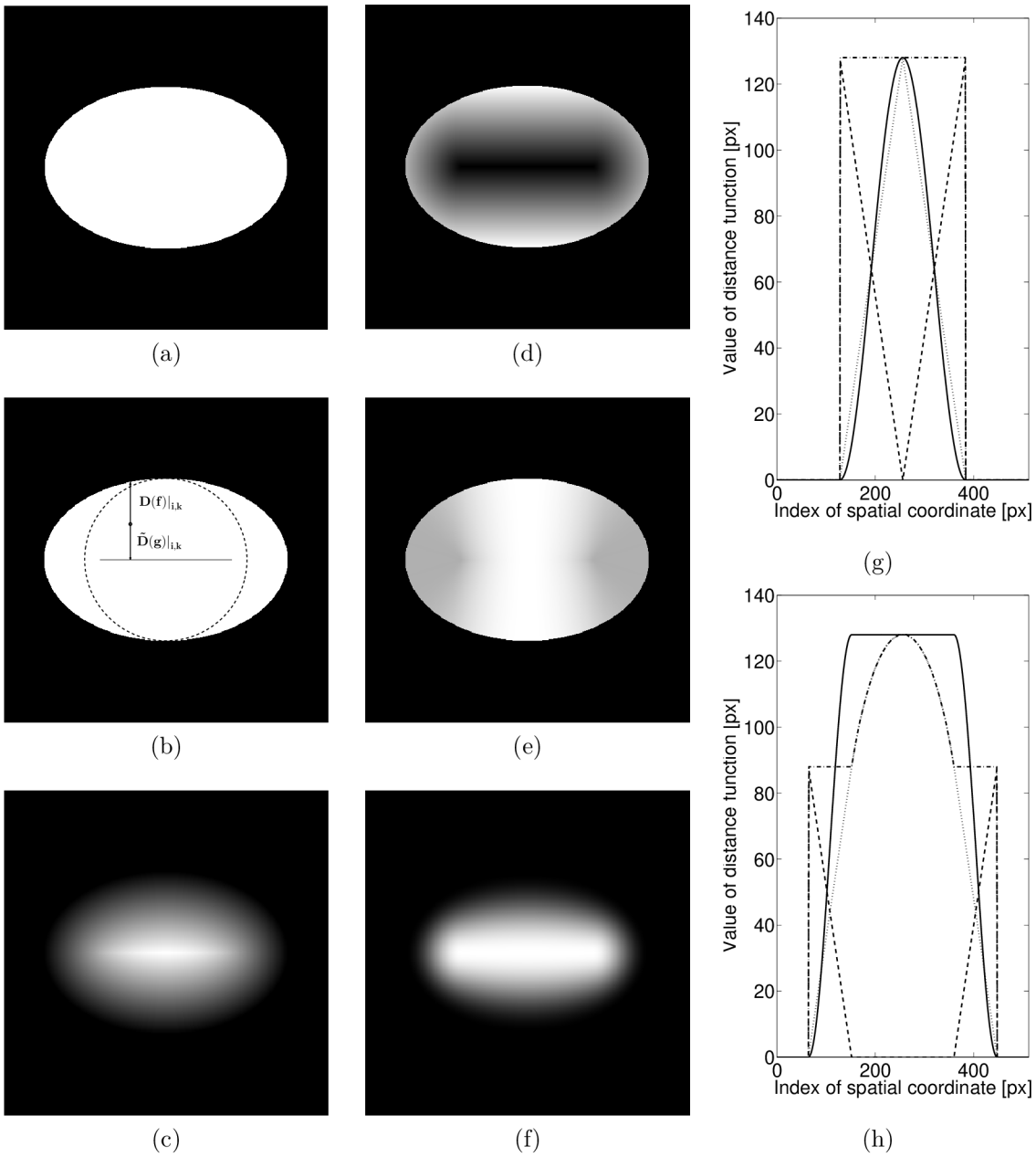

Obr. 4.11: Medial axis based design of 2D SAW demonstrated on a single elliptically shaped binary object: (a) original binary object, (b) heuristically determined medial axis of the object delineated by a solid line and schematic representation of calculation of local thickness for a single pixel, (c) distance map of the binary object, (d) map of distances to closest points of the medial axis, (e) distribution of local thicknesses, (f) final Welch type 2D SAW, (g) - (h) cross-sections of figures from Fig. 4.11c to Fig. 4.11f taken along minor (g) and major (h) axis: dotted line ($\cdots$) cross-section of the distance map; dashed line ($- - -$) cross-section of the map of distances to closest points of the medial axis; dash-dotted line ($\cdot - \cdot$) cross-section of the local thicknesses map; solid line (——) cross-section of the Welch type 2D SAW (in order to fit on axis of the plot multiplied with maximum of local thicknesses).

of maximal disk delineated by dashed line ($---$), which is obviously a greater value than intuitively expected. The proposed medial axis based local thickness estimation gives, for an objects with such a simple shape and properly determined medial axis, obviously more precise results.

The need for "properly" determined medial axis is the main disadvantage which complicates usage of the proposed method as a general local thickness estimator, however, it shows to be a very useful tool for design of 2D SAW. A maximal disks based method for determination of medial axis proposed in [16] (described above) has been chosen as it enables to control shape of generated medial axis by choice of the ρ parameter in Eq. 4.21. Effect of ρ parameter setting is demonstrated in Fig. 4.12 where two medial axes with different ρ (2 and 50) are visualized. Medial axis with low ρ contains many redundant branches which are not important for description of object's shape and may be removed by ρ increasing (as stated in [16], setting of the ρ parameter can be considered a simple pruning method).

Pixels included to the medial axis in Fig. 4.12a can be divided into three groups; examples of those pixels and corresponding maximal disks labeled by numbers from 1 to 3 can be seen in Fig. 4.12c. Maximal discs with ρ significantly lower than the their diameters are included into the first group; those discs are redundant for purposes of 2D SAW design. Maximal disks which are fundamental for description of object's shape have ρ equal to their diameters, i.e. are touching object's border on its opposite sites, and forms the second group. The third group is formed by maximal disks touching points on contour where two objects are intersecting.

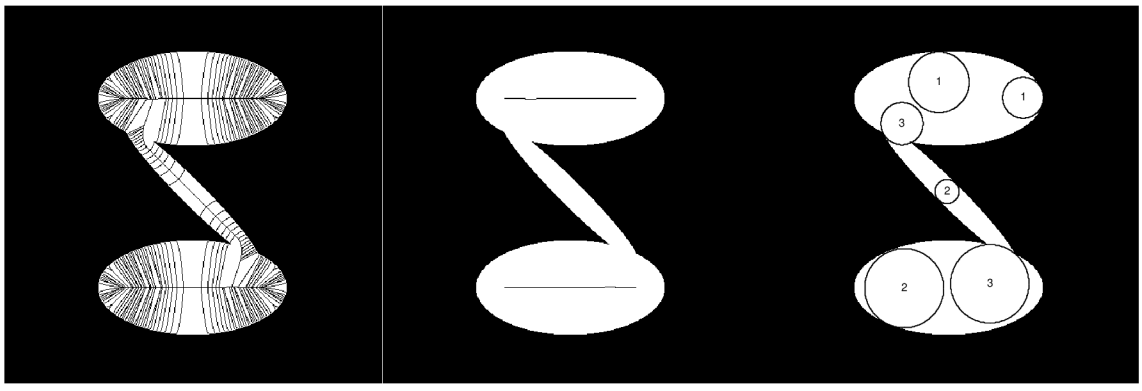

(a) (b) (c)

Obr. 4.12: Effect of parameter ρ setting to a maximal disks based medial axis transform: (a) medial axis with low ρ parameter ($\rho = 2$), (b) medial axis with high ρ parameter ($\rho = 50$), (c) examples of the three types of maximal disks which form medial axis of a given binary object.

Points of medial axis formed by redundant maximal disks are highly inappropri-

ate for 2D SAW design as they are located out of object's center parts and do not fit the idea of medial axis based local thickness calculation as visualized in Fig. 4.11b. Two approaches for medial axis determination, the first is formed only by maximal disks of second type and the second is formed by combination of maximal disks of second and third type, which are suitable for 2D SAW design are presented in the following paragraphs.

Generally, it is impossible to find a single global value of ρ which would produce a pruned medial axis with redundant branches eliminated. ρ, thus, should be spatially variable. A maximal disks based distribution of local thicknesses depicted in Fig. 4.10c is a suitable choice for ρ parameter distribution as the second type maximal disks are characteristic by ρ equal to the object's local thickness in their centers. The resulting medial axis, within this thesis called a local thickness limited medial axis, where only centers of second type maximal disks are included, can be seen in Fig. 4.13 as well as the corresponding map of distances to closest points of medial axis, the variable N and the resulting Welch type 2D SAW.

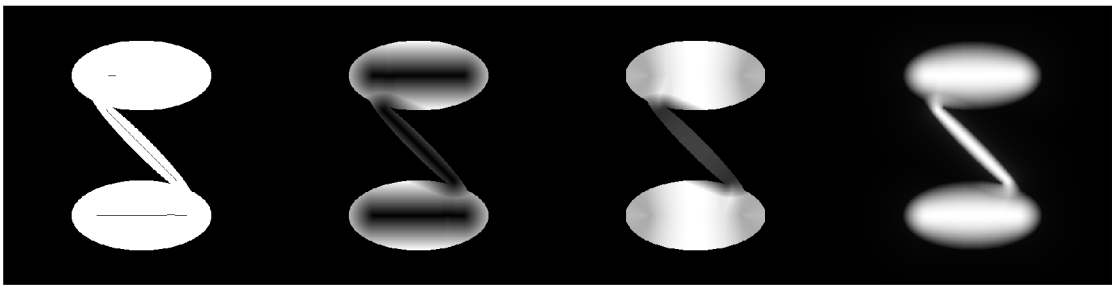

(a) (b) (c) (d)

Obr. 4.13: Stages of 2D SAW design based on local thickness limited medial axis: (a) local thickness limited medial axis subtracted from the testing binary object, (b) map of distances to closest points of medial axis, (c) spatial distribution of variable N, (d) Welch type 2D SAW designed using local thickness limited medial axis.

Local thickness limited medial axis does not necessarily have to be connected; another type of pruned medial axis called major medial axis is, thus, proposed. Computation of a major medial axis is initialized by a local thickness medial axis which is iteratively recalculated until a medial axis not changes its shape. In each iteration, end-points of medial axis are determined and value of local thickness in location of a given end-point is expanded to 3×3 neighborhood. Such modified distribution of local thicknesses is used as parameter ρ for calculation of medial axis in the next iteration.

The major medial axis of the testing binary object as well as the derived map of distances to closest points of medial axis, the variable N and the Welch type 2D

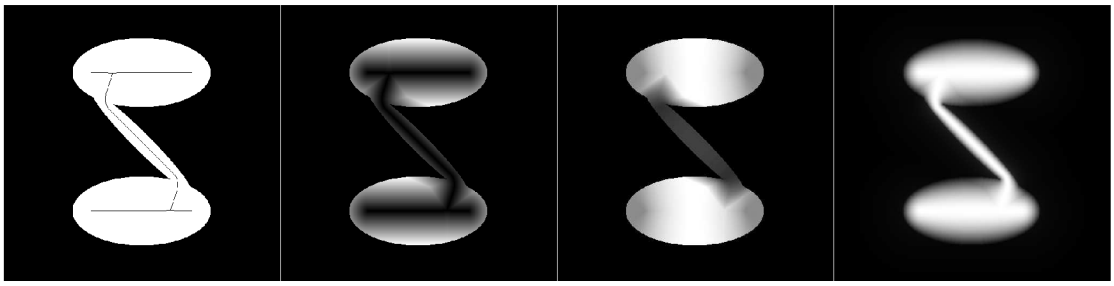

(a) (b) (c) (d)

Obr. 4.14: Stages of 2D SAW design based on major medial axis: (a) major medial axis subtracted from the testing binary object, (b) map of distances to closest points of medial axis, (c) spatial distribution of variable N, (d) Welch type 2D SAW designed using major medial axis.

SAW are depicted in Fig. 4.14. Comparing the results of all three 2D SAW design approaches, both medial axis based approaches produce much smoother windowing functions than the local thickness based one.

Optimization of 2D SAW design

Selection of a medial axis calculation type certainly influences frequency properties of a final windowing functions. Another aspect which influence frequency properties of the designed SAW is the fact how close are medial axis end-points to the object's border. This aspect is demonstrated on measurement and comparison of frequency properties of three versions of Welch spatially adaptive windowing functions derived from elliptically shaped binary object (length of major and minor axis are 128 px and 32 px, respectively, in 512 × 512 px sized image) with differently long medial axes (41 px, 81 px and 121 px centered on object's major axis). Two-dimensional Fourier transforms of considered 2D SAWs are computed and resulting spectra are reformatted to polar coordinates, see example in Fig. 4.15a. Two spectral parameters routinely used in analysis of one-dimensional windowing functions [25], [60] are computed for each column of a reformatted spectral matrix and subsequently visualized using graphs in polar coordinates in Fig. 4.15b and Fig. 4.15c.

The two selected spectral parameters are a maximum side lobe level (MSLL), a peak ripple value of the side lobes evaluated from log magnitude of window's spectrum, and selectivity, the frequency at which the main lobe drops to the peak ripple value of the side lobes [60].

According to polar plots in Fig. 4.15, shape of medial axis substantially influences window's spectral properties and thus have impact to its quality (i.e. suitability

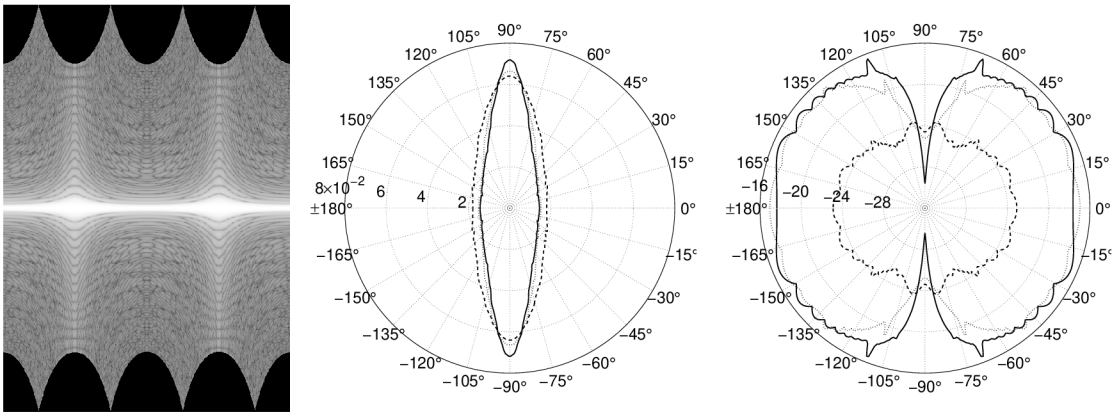

(a) (b) (c)

Obr. 4.15: Influence of shape of medial axis to frequency properties of 2D SAW demonstrated on three versions of Welch spatially adaptive windowing function derived from elliptically shaped binary object (length of major and minor axis are 128 px and 32 px, respectively, in 512 × 512 px sized image) with heuristically determined; 41 px (plotted by dashed line (− − −)), 81 px (plotted by dotted line (· · ·)) and 121 px (plotted by solid line (——)) long medial axes centered on object's major axis: (a) a spectrum of Welch type 2D SAW with design based on 41 px long medial axis reformatted to polar coordinates, (b) polar plots of selectivity parameters, (c) polar plots of MSLL parameters.

for a given specific application). Optimization of 2D SAW design by adaptation of medial axis would, therefore, provide better results than aforementioned approaches, provided that quality of the designed 2D SAW can be measured.

Proposed optimization is initialized either by a local thickness limited medial axis or a major medial axis on which branch points and end points, defined in [9], are detected. A medial axis is than decomposed into individual branches which are subsequently recognized as internal branches (terminated by two branch points), ending branches (terminated by end point and branch point) and isolated (terminated by end points). Lengths (from branch point to end point) of ending and isolated (length from branch's center to end points) branches are iteratively modified in order to obtain optimal 2D SAW design. Generally, any multidimensional optimization method can be used for 2D SAW design optimization; a stochastic gradient descent [56] with adaptive step size is used in this approach.

4.3.4.2 Quantitative comparison of 2D SAWs with binary masks

Two tests which demonstrate practical usage of 2D SAW and also serve to compare quality of designed 2D SAWs according to a quality of the rectangular one (testing binary object Fig. 4.10a is used) are described in the two following chapters.

Quality of phase part of normalized cross spectrum

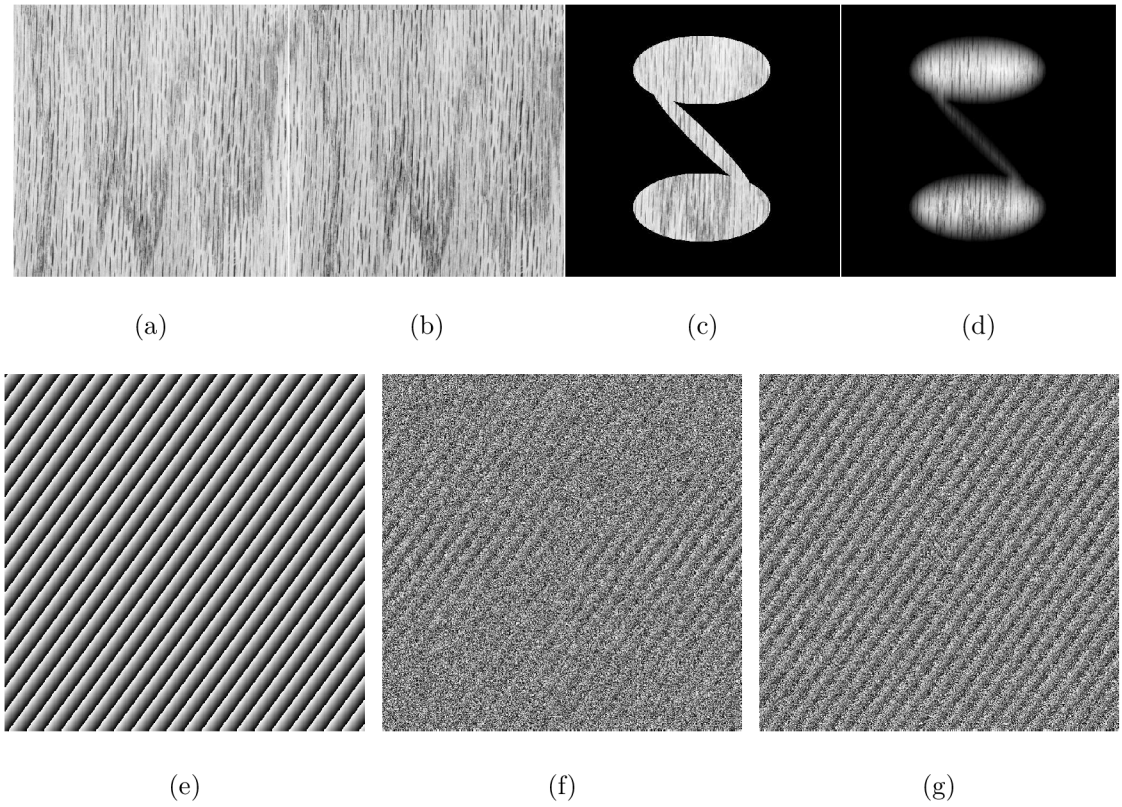

Obr. 4.16: Demonstration of 2D SAW quality measurement based on quality of phase part of normalized cross spectrum: (a) Test image of wood texture, (b) Translated test image, (c) Translated test image weighted by the binary mask, (d) Translated test image weighted by the Welch type 2D SAW with design based on optimized local thickness limited MAT, (e) $\arg(P(u,v))$ calculated from images (a) and (b) with quality -3.1532, (f) $\arg(P(u,v))$ calculated from images (a) and (c) with quality 0, (g) $\arg(P(u,v))$ calculated from images (a) and (b) with quality -0.102.

First test is based on measurement of quality of a phase part of normalized cross spectrum $\arg(P(u,v))$ of two mutually shifted images calculated according to Eq. 3.20 which is often used for a phase correlation based shift estimation. Normalized cross spectrum of two shifted versions of an image have ideally linear phase part

providing that no distortion by interpolation is introduced during a sub-pixel shift and identical bordering effect, imposed by periodicity of DFT, is present in both image's versions. Both conditions are fulfilled when images are shifted via frequency domain approach (i.e. spectrum of image to be shifted is modified by a linear phase with a slope corresponding to amount of shift in original domain; a shifted version is obtained after inverse DFT). Ideally linear phase part of such shifted pair of images (with exception of discontinuities caused by warping of phase around $\pm\pi$) can be seen in Fig. 4.16e.

Let us have an original image (Fig. 4.16a) and its shifted version (Fig. 4.16b) from which only a certain part, delineated by a binary mask Fig. 4.10a, is known (Fig. 4.16c). The task is to calculate $\arg(P(u,v))$ which will be as close as possible to the ideal one (when a full matrix of shifted image is known) and, thus, ensure the best possible input for algorithms of phase correlation based shift estimation. Spectrum of an image weighted by a binary mask is, according to convolution theorem, formed by convolution of spectrum of an image and spectrum of a binary mask. This enforces many imperfections to a phase part of resulting normalized cross spectrum, as can be seen in Fig. 4.16f.

Proposed criterion of 2D SAW quality (which is also used as a cost function in its optimized design) is mean of absolute values of $\arg(P(u,v))$ second differences calculated in x and y directions. As second difference of linear function is equal to zero, the quality criterion is, in case of two shifted versions of an image, equal to mean value of discontinuities caused by phase warping. Weighting of an image by a binary window causes additional imperfections which may, potentially, be lowered by replacement of a binary mask by a 2D SAW. The part of quality criterion caused by phase warping is depending on amount of shift between images (the shift influences slope of linear phase and thus a number of the discontinuities caused by phase warping). In order to suppress this dependence a quality of binary window is subtracted from quality of a 2D SAW; a negative values, thus, means quality improvement compared to a binary window and vice versa.

A Welch type 2D SAW with design based on an optimized local thickness limited MAT can be seen in Fig. 4.16d and a corresponding phase part of normalized cross spectrum in Fig. 4.16g. The $\arg(P(u,v))$ calculated using the 2D SAW has, not only numerically (-0.102), but also visually, better quality than the $\arg(P(u,v))$ calculated using the binary window. Hundred measurements of quality of phase part of normalized cross spectra are performed on the test binary object Fig. 4.10a. A randomly selected texture image[1] and its versions randomly shifted in x and y directions (random shifts are from uniform distribution $\mathcal{U}(1,10)$ px) are used.

[1]Ten test texture images are taken from The USC-SIPI Image Database created at Signal and Image Processing Institute, University of Southern California

Quality of one-dimensional noise power spectrum estimation

The second test is based on measurement of errors in 1D NPS estimation introduced by weighting of a noise matrix. Matrices filled by noise with known noise power spectra are generated similarly as in Sec. 4.3.2. In order to incorporate dependence of 2D SAW quality on noise frequency properties, Gaussian curves with variable mean are, this time, used as spectral modulation functions. The quality criterion is designed as sum of absolute values of differences between 1D NPS of the gold standard (i.e. matrix fully filled by noise) and 1D NPS calculated from matrix weighted by a 2D SAW or a binary window. In order to be consistent with the former criterion, a quality of binary window is subtracted from a quality of 2D SAW.

Example of 1D NPS of a matrix (sized $512 \times 512 \times 50$) fully filled by noise spectrally modulated by a Gaussian function $\mathcal{N}(0.5, 0.2)$, weighted by a binary window and by a corresponding 2D SAW with design based on an optimized local thickness limited MAT can be seen in Fig. 4.17. 1D NPS estimated from by the 2D SAW weighted matrix, with quality -0.916, is, evidently (see magnified sections), closer to the golden standard than the binary window weighted one.

Hundred test matrices sized $512 \times 512 \times X$ voxels (where X is randomly generated from $\mathcal{U}(10, 100)$) filled by noise spectrally modulated by Gaussian curves with random mean $\mathcal{U}(0.1, 0.7)$ and a standard deviation 0.2, are generated and serve as mentioned gold standard. Each slice of noise matrices is subsequently weighted by a binary window/2D SAW and 1D NPS are computed.

Tab. 4.6: Quality of variants of 2D SAWs designed from the test binary image Fig. 4.10a. Results for both proposed quality measurements (quality of phase part of normalized cross spectrum and precision of 1D NPS estimation) are presented in form of mean value $\pm$ standard deviation.

Window type/Quality Criterion	Phase Quality	1D NPS
Binary	0 ± 0	0 ± 0
SAW Local Thick.	-0.0800 ± 0.0250	-0.764 ± 0.271
SAW Local Thick. Limited MAT	-0.0845 ± 0.0262	-0.781 ± 0.261
SAW Major MAT	-0.0843 ± 0.0261	-0.785 ± 0.258
SAW Local Thick. Limited MAT Opt.	-0.1142 ± 0.0293	-0.820 ± 0.260
SAW Major MAT Opt.	-0.0864 ± 0.0258	-0.800 ± 0.251

Results of proposed quality tests of 2D SAW variants designed from the test binary image Fig. 4.10a are summarized in Tab. 4.6. Based on the presented results,

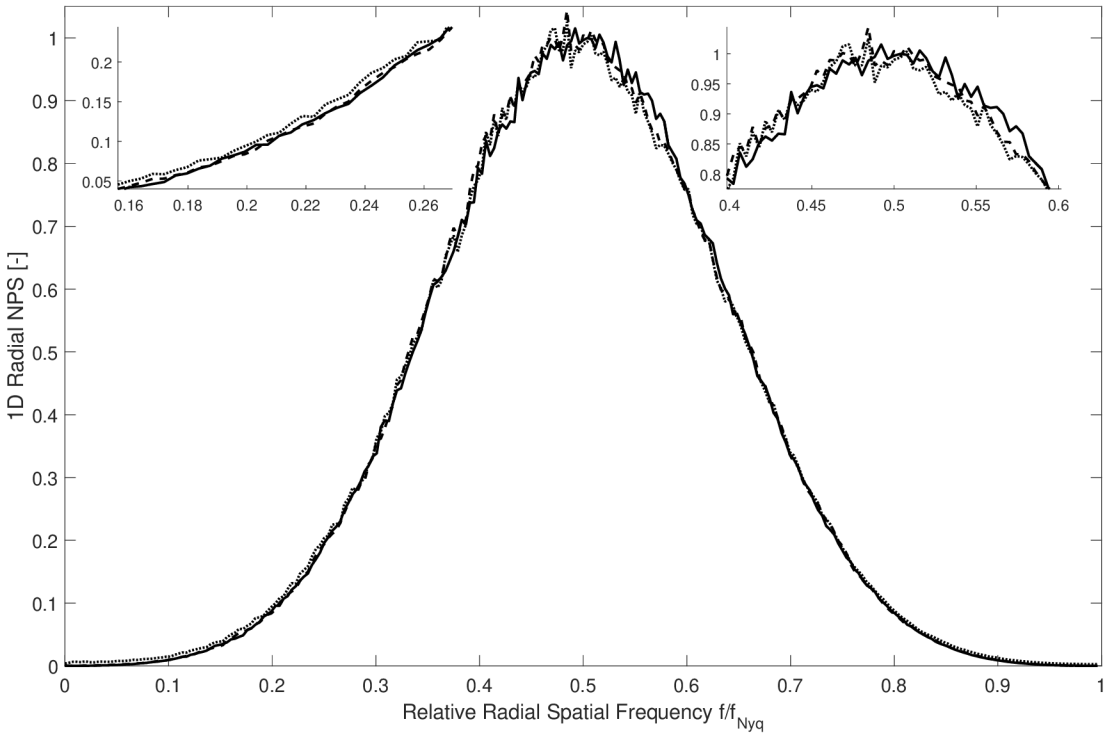

Obr. 4.17: Quality of the 2D SAW evaluated by precision of 1D noise power spectrum estimation: 1D NPS of the gold standard (plotted by solid line (——)), 1D NPS of noise matrix weighted by the binary mask (plotted by dotted line $(\cdots)$), 1D NPS of noise matrix weighted by the 2D SAW with design based on optimized local thickness limited medial axis transform (plotted by dashed line $(- - -)$).

it can be concluded that, for the given testing binary object, each 2D SAW variant produces more quality results than the binary mask and optimization of 2D SAW design helps to even more improve 2D SAW quality.

Evaluation of 2D SAW quality on a database of test binary objects

Quality of 2D SAWs was, so far, demonstrated on the test binary image. In order to capture their dependence on variable shape of binary objects, larger comparison performed on a database of artificially generated binary images is done. A testing database contains hundred 512×512 px sized images of binary objects which are unions of random number of ellipses from $\mathcal{U}(1, 10)$ with random center from $\mathcal{U}(192, 320)$ px, length of major and minor axis from $\mathcal{U}(4, 64)$ and orientation from $\mathcal{U}(0, \pi)$.

One of the optimized approaches always gives the best 2D SAW quality, however, generally it is impossible to predict which design of 2D SAW is the best for a given

specific problem. Quality of binary window is, thus, this time compared with the version of 2D SAW with the best quality (selected among versions proposed above).

Thousand measurements of both proposed 2D SAW quality criteria are performed similarly as in the previous sections, this time with randomly selected binary object from the database. The results are presented as mean value ± standard deviation calculated from the set of the thousand measurements. 2D SAW quality measured by precision of phase part of normalized cross spectra estimation is -0.0202 ± 0.0193 whereas 2D SAW quality measured by precision of 1D NPS estimation is -0.4537 ± 0.2432. It can, thus, be concluded that quality of 2D SAW windowing function, considering the two tested criteria, is generally superior to the quality of binary mask.

4.3.5 Improvement of segmentation introduced errors by 2D SAW application

Once the methodology for 2D SAW design is established, its impact to segmentation introduced errors in the same manner as in Sec. 4.3.3 can be evaluated. A cost function for an optimization based 2D SAW design can not be, for this application, defined as a gold standard (i.e. a curve of tissue 1D NPS unaffected by the tissue segmentation) can not be established due to lack of information about a shape of 1D NPS in real patient data. The design approach based on major medial axis transform without optimization is selected as it provided the best results during the testing on the database of artificial binary objects. An example of 2D SAW applied to a binary mask of segmented bones is visualized in Fig. 4.18.

Results of measurement of errors in 1D NPS center of gravity estimation introduced by segmentation of diverse tissues, when a Welch type 2D SAW with design based on major medial axis transform is used, are summarized in Tab. 4.7.

Tab. 4.7: Means and standard deviations of errors in estimation of center of gravity of 1D noise power spectra introduced by tissue segmentation after application of 2D spatially adaptive windowing functions.

	Soft Tissue	Bones	Adipose tissue	Air filled structures
mean SIE [%]	0.021	0.038	0.115	0.157
std SIE [%]	0.014	0.036	0.105	0.134

By comparison of Tab. 4.5 and Tab. 4.7 where means and standard deviations of segmentation introduced errors with and without 2D SAW utilization are shown, it is evident that, for each considered tissue, SIE rapidly decreases after 2D SAW

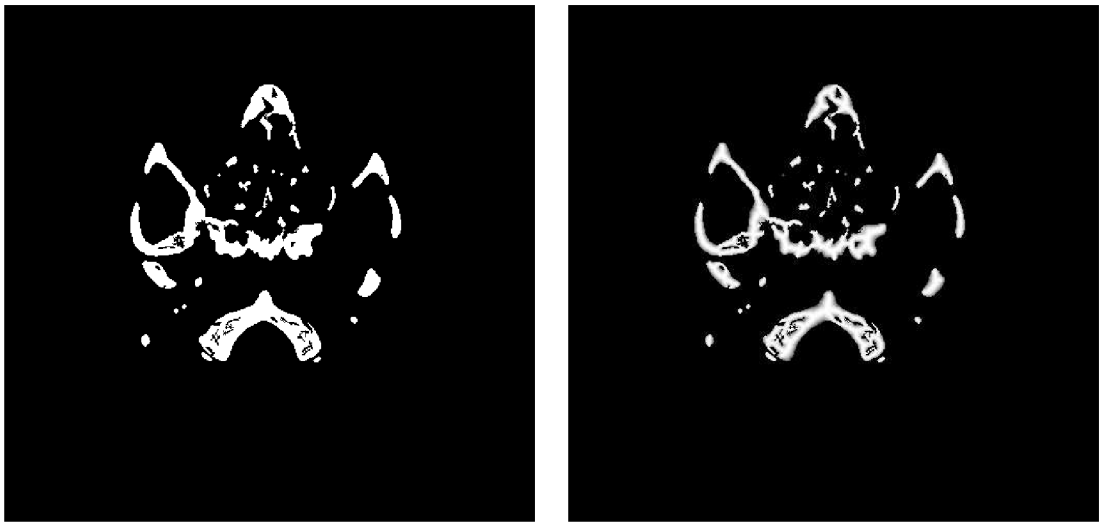

(a) (b)

Obr. 4.18: Example of the two-dimensional spatially adaptive windowing function applied to the binary image of segmented bones: (a) binary image of segmented bones, (b) derived Welch type 2D SAW.

application. Magnitudes of segmentation introduced errors are substantially lower than magnitudes of stability indexes evaluated on phantoms for soft tissue and bones (see the results in Tab. 4.4), however they are still relatively high for adipose and air filled tissues. It can, thus, be concluded that, after the 2D SAW application, measurement of stability indexes in separate tissues of real patient data is possible.

5 COMPARISON OF FBP, IDOSE^4 AND IMR METHODS BY FIDELITY OF ANATOMICAL STRUCTURES RECONSTRUCTION

As already stated, both tested iterative reconstruction methods (iDose^4 and IMR) should significantly reduce level of image noise. The main difference between them lies in fidelity of anatomical information reconstruction, which should be significantly improved by IMR method (compared to the results obtained by FBP reconstruction). The main goal of "The IMR project" is to design a CT image quality measure which would be able to assess fidelity of anatomical information reconstruction.

Evaluation of fidelity of anatomical information reconstruction in real patient data is problematic due to missing gold standard (i.e. exact and correct values of HU in tissues are not a priory known). The only exception may be represented by airways which contain only air (provided that no pathology is present) with exactly known density (-1000 HU). Another aspect which makes airways an ideal object for evaluation of fidelity of anatomical structures reconstruction is that they are composed of "tubes" with different diameters, a dependence of the quality of reconstruction on size of imaged detail may be also evaluated.

As a theoretical density inside airways is known, each positive deviation from that value is considered as decrease of image quality. A parameter describing image quality is, thus, simply mean of densities inside airways whereas the lower the mean is (closer to -1000 HU) the more quality the reconstruction method is. Airways segmentation represents an inevitably preprocessing step, which is presented in Sec. 3.3.

Once the quality measurement of anatomical structures reconstruction is established, mutual comparison among considered reconstruction methods can be performed. Comparison of data reconstructed by diverse methods from a single set of projections is not problematic as they are perfectly aligned and identical airways segmentation mask is used. Problem arises when the reconstructions of 80% and 20% dose scans have to be compared. Both scans are naturally displaced due to respiratory movements. Moreover, thanks to rapidly increased noise level in a 20% scan, some airways branches, which are correctly segmented in S_{80}, may remain unsegmented in S_{20}. Different voxels, thus, may enter quality measurement and comparison among reconstructions method would be inconsistent. Reliable methods for CT image registration are, of course, available, however, interpolation necessary for geometric transforms would negatively influence the quality measurements. A method which unifies both airways segmentations and allows for comparison of corresponding airways voxels in both scans is presented in Sec. 5.1. Image registration is, in

this method, used in such way that none image data are affected by interpolation.

Very interesting results may be obtained when quality of airways reconstruction is related to airways thickness. Ability of considered reconstruction methods to properly reconstruct details with different sizes may be revealed. A method which would be able to assign local thickness to each voxel of segmented airways is needed and is presented in Sec. 5.2.

Besides objective fully automatic evaluation of quality of airways reconstruction, a subjective medical quality evaluation was also performed. Four experienced radiologists independently evaluated and rated image quality of individual reconstruction methods in terms of four "technical" image quality parameters (image noise, image artifacts, anatomical details, sharpness) and four parameters related to medical diagnostic process (low-contrast resolution, total impression of the reconstructed image, possibility of influencing the description, and possibility of influencing the examination's conclusion). Only the "technical" image quality parameters are evaluated in this thesis. A methodology for statistical evaluation of subjective medical image quality assessments is presented in Sec. 5.3 and resulting findings are summarized in Sec. 6.

Objective assessment of quality of airways reconstruction can be considered as measurement of ability of imaging system to properly reconstruct image details. In order to validate the proposed objective method, it can be compared with subjective medical evaluation of a details parameter. The results of this comparison are summarized in Sec. 6.

5.1 Determination of corresponding voxes between segmentations of 80% and 20% dose scans

A proposed method for correction of inconsistencies between airways segmentation of 20% (S_{20}) and 80% (S_{80}) dose scans uses two fully automatic registration steps. Image registration is the technique frequently used in medical image processing. It targets to finding a best possible spatial relationships between two images. Among a number of published registration methods a group of methods utilizing optimization of intensity based cost functions are the most suitable for the given registration problem.

Intensity based registration of a fixed $I_F(\boldsymbol{x})$ and a moving image $I_M(\boldsymbol{x})$, where $\boldsymbol{x}$ represents vector of spatial coordinates, is an optimization problem where geometrical transformation of moving image $I_M(\boldsymbol{x})$, which minimizes a cost function C (a measure of similarity between the images to be registered), is iteratively searched.

The registration procedure is expressed by

$$\hat{\boldsymbol{\mu}} = \arg\max_{\boldsymbol{\mu}} C\left(\boldsymbol{T}_{\boldsymbol{\mu}}; I_F(\boldsymbol{x}), I_M(\boldsymbol{x})\right), \tag{5.1}$$

where $\boldsymbol{T}$ represents geometrical transform controlled by a parameter vector $\boldsymbol{\mu}$. $\hat{\boldsymbol{\mu}}$ denotes the optimal solution.

The proposed correction can be divided into four main steps as follows:

1. Flexible registration of data from single medical examination acquired with 80 % and 20% dose yielding parameter vector $\hat{\boldsymbol{\mu}}$ of geometric transform $\boldsymbol{T}_{\hat{\boldsymbol{\mu}}}$ such that transformed 20% scan is optimally (in a sense of used similarity measure) spatially identified with 80% scan.
2. An airways segmentation of 20% scan, obtained by an approach described in Sec. 3.3, is geometrically transformed by $\boldsymbol{T}_{\hat{\boldsymbol{\mu}}}$.
3. A voxel by voxel intersection of S_{80} and $\boldsymbol{T}_{\hat{\boldsymbol{\mu}}}(S_{20})$ according to

   $$S_{20\cap 80} = S_{80} \cap \boldsymbol{T}_{\hat{\boldsymbol{\mu}}}(S_{20}) \tag{5.2}$$

   is computed, hence, only voxels located on identical spatial coordinates which are active in both airways segmenations are preserved.
4. Another flexible registration is used to calculate inverse geometrical transform $\boldsymbol{T}_{\hat{\boldsymbol{\mu}}}^{-1}$ which cancels $\boldsymbol{T}_{\hat{\boldsymbol{\mu}}}$ and $S_{20\cap 80}$ is transformed to be spatially consistent with S_{20}.

Both registration steps are performed using a publicly available registration package Elastix described in [58] which is often used for registration of a medical image data. A large number of methods for medical image registration is available in literature, however there is no method which is universal (i.e. is suitable for any image registration problem). Elastix is a modular tool for intensity based image registration which includes many different algorithms and approaches (various types of geometrical transformations, cost functions, optimizers or sampling strategies) used in medical image registration which are optional and can be arbitrarily combined. The main advantage of Elastix is its modularity which enables to easily design registration approach tailored for a given specific application.

The registration method published in [76] which utilizes Elastix software package is used in this thesis. Though originally intended for registration of dynamic CT lung data, for a purpose of assessment of anatomical structures motion and evaluation of motion related pathologies, it also turned out to be a useful tool for registration of 80% and 20% dose CT lung scans (with focus on proper registration of airways). Based on subjective visual evaluation of airways registration, this method provides the best results among other tested registration approaches (which are also focused on registration of CT lung data and utilize the Elastix software) namely [82], [103], [18], [92].

A B-spline transformation model, according to [97], as $\boldsymbol{T}_{\boldsymbol{\mu}}$, mean squared differences as C and adaptive stochastic gradient descent, according to [57], as an optimizer are used in [76]. The registration method utilizes also multi-resolution pyramid approach (registration starts on sub-sampled and blurred data which determines raw solution further refined on successive more detailed pyramid levels) with four levels (used schedule of isotropic down-sampling factors is 8, 4, 2, 1) and random sampler (in each iteration, sampler selects a certain number of voxels from which a cost function is computed which leads to decreased computational requirements) which selects subset of 2000 data elements. The random samplers are especially useful in combination with adaptive stochastic gradient descent optimizer [56].

After the correction of inconsistencies between airways segmentations of 20% and 80% dose scans, $S_{20\cap 80}$ can be used for extraction of airways from 80% and $\boldsymbol{T}_{\hat{\boldsymbol{\mu}}}^{-\mathbf{1}}(S_{20\cap 80})$ from 20% dose scan, whereas locations of extracted airways voxels are, thanks to the proposed methodology, spatially corresponding.

5.2 Measurement of airways thicknesses

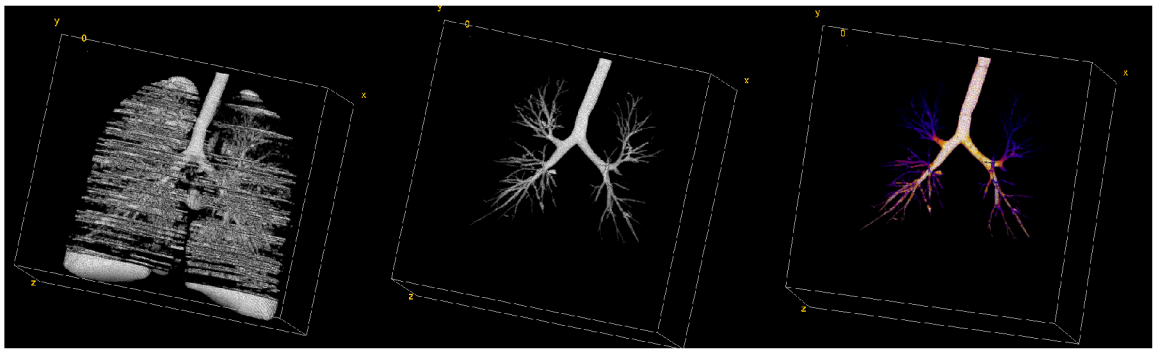

(a) (b) (c)

Obr. 5.1: Visualizations of stages of airways segmentation and local thickness measurement by volume rendering: (a) airways candidates produced by a graph-cut segmentation of data enhanced by gray-scale morphological reconstruction, (b) final airways segmentation after 3D region growing, (c) visualization of airways local thickness map.

Thanks to gradually decreasing thickness of individual airways tree branches as they are approaching peripheral lungs parts, ability of the considered reconstruction methods to faithfully reconstruct structures of different sizes (i.e. airways with different thickness) can be evaluated. Hence, a parametric map which assigns a value of airways local thickness to each voxel needs to be derived. A method for evaluation

of local thicknesses in two-dimensional binary images based on medial axis transformation was presented in Sec. 4.3.4.1. The generalization of this method to three dimensional space is straightforward, hence, it is used for evaluation of airways local thicknesses. Whole segmented airways tree is divided into three parts according to local thickness measured in millimeters (from 0 mm to 4 mm, from 4 mm to 8 mm and thicker than 8 mm) and objective image quality is evaluated separately in those parts.

5.3 Subjective medical image quality evaluation

Four experienced radiologists independently evaluated and rated four "technical" image quality parameters (i.e. parameters related to CT data acquisition process); image noise, image artifacts, anatomical details and sharpness. A modified 5-point Likert scale ranging from -5 points to +5 points were used. The value of image quality parameters of data reconstructed using FBP at a 80% dose always had a value of 0 points (FBP is reference reconstruction, other methods are, thus, evaluated relatively to quality of FBP). Improvement in an individually evaluated parameter was indicated by positive points while deterioration was shown by negative points. The points scale was defined as follows: FBP 80%: 0 points; -5 points: practically unevaluable; -4 points: difficult to evaluate; -3 points: noticeable parameter deterioration; -2 points: slight parameter deterioration; -1 point: very slight parameter deterioration; 1 point: very slight parameter improvement; 2 points: slight parameter improvement; 3 points: noticeable parameter improvement; 4 points: considerable parameter improvement; 5 points: highly considerable parameter improvement.

Statistical analysis requires a single value of the quality score for a given data reconstruction. Such value was obtained as the mean value calculated among the medical experts. Mean values of subjective evaluations in individual groups are visualized using heat maps (Fig. 5.2 and Fig. 5.3), where a value of 0 (reference quality of FBP reconstruction with 80% of applied dose) is indicated by white while negative or positive values (lower/higher image quality) are colored red or green, respectively, according to the color bars on the right-hand side of each heat map. Heat map visualization reveals relationships among types of reconstructions, patient groups, and evaluated quality parameters. The visualization helps to establish the hypotheses to be tested by the procedure described in the following paragraph.

Many statistical tests (e.g. among patient groups, depending on the particular hypothesis formulation) must be conducted to confirm that the mutual relationships revealed by visual inspection of the heat maps are statistically significant. Wilcoxon rank-sum test, which is suitable for testing a null hypothesis stating that two tested

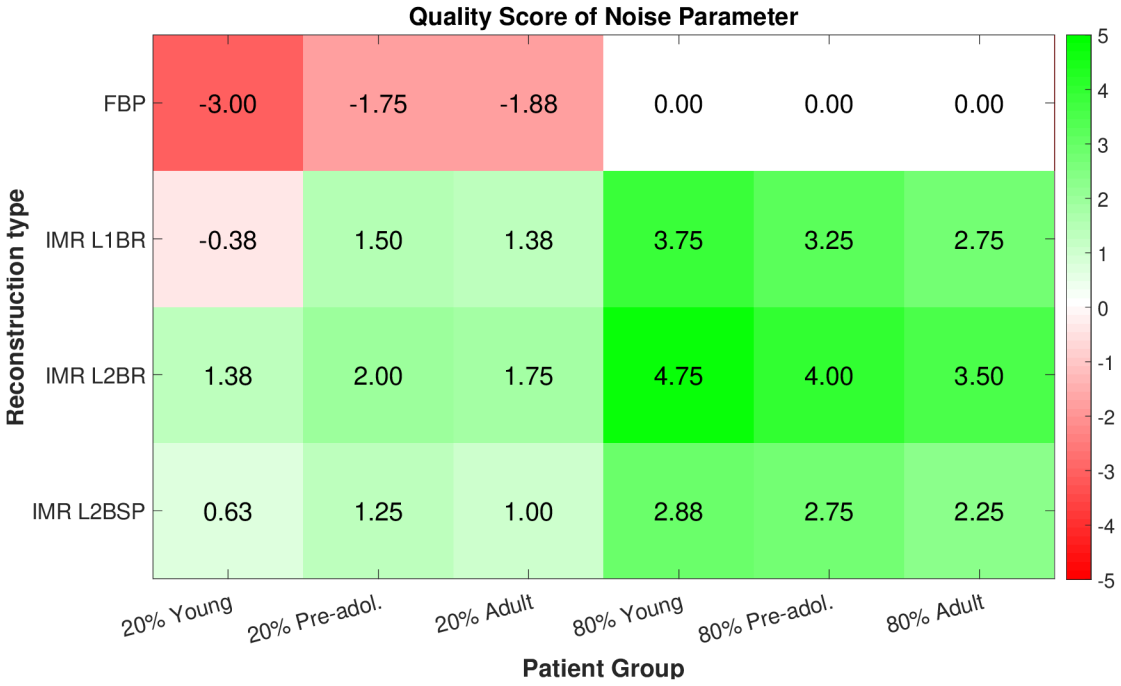

(a)

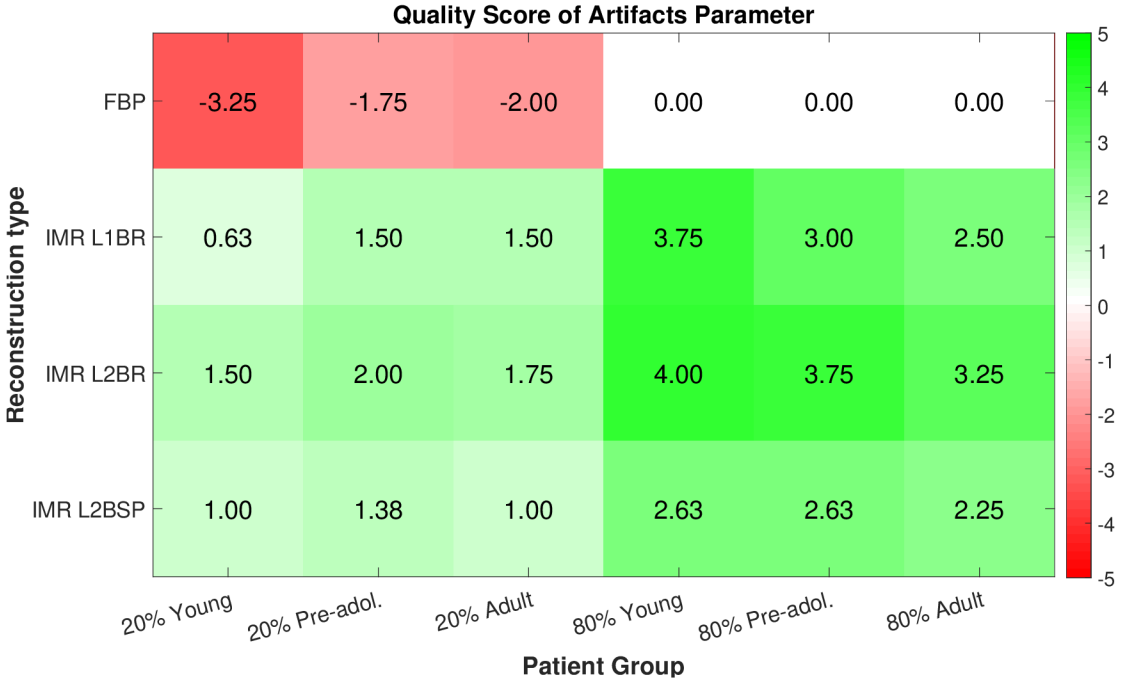

(b)

Obr. 5.2: Heat maps visualizing mean values of subjective medical quality evaluations in individual patient groups and reconstruction types for evaluated image quality parameters: (a) CT image noise, (b) image artifacts.

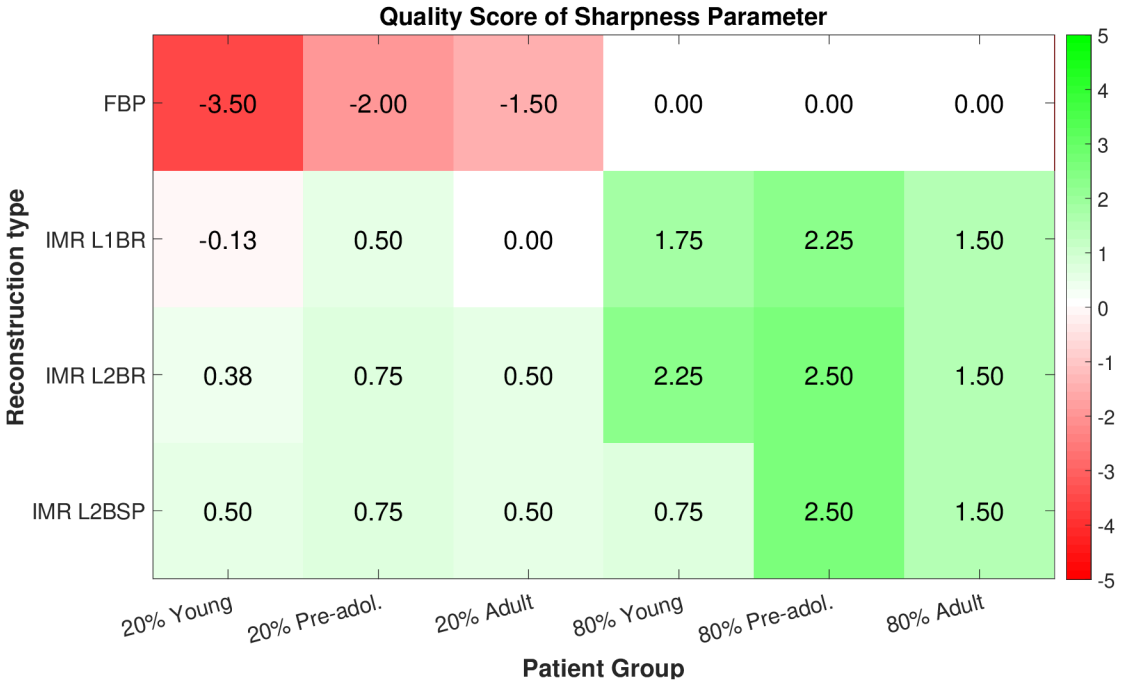

(a)

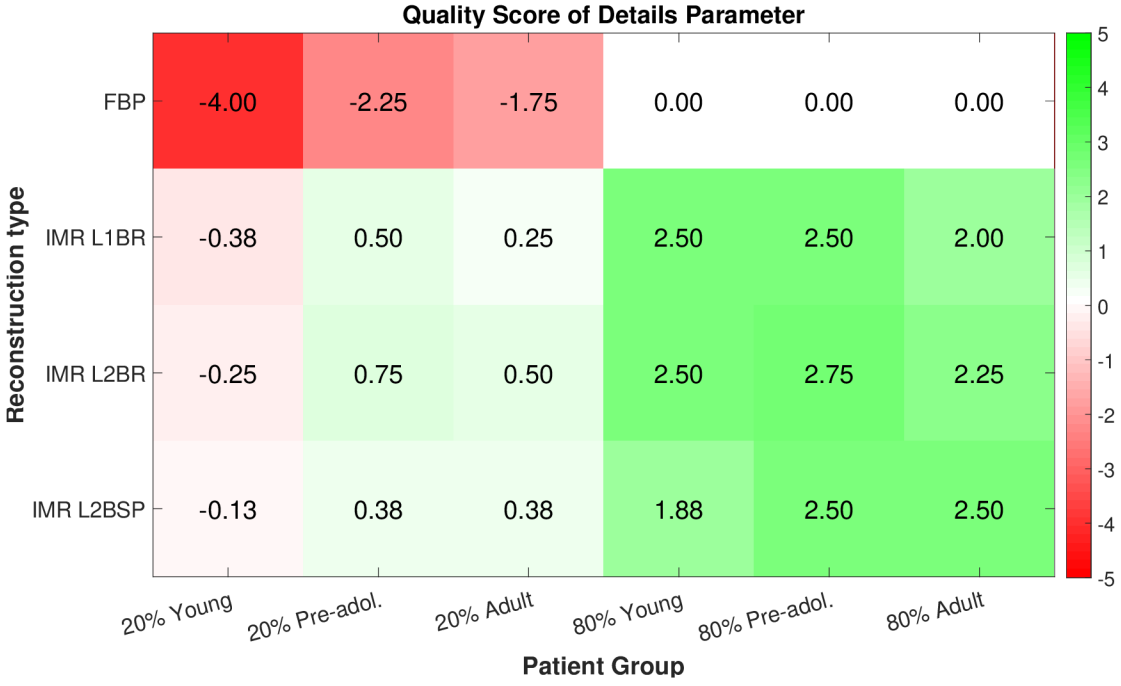

(b)

Obr. 5.3: Heat maps visualizing mean values of subjective medical quality evaluations in individual patient groups and reconstruction types for evaluated image quality parameters: (a) sharpness, (b) details.

groups of subjective evaluations are samples from a distribution with equal medians against the alternative that they are not, is used. A positive test result indicates rejection of the null hypothesis at the 5% significance level and acceptance of the alternative hypothesis (medians of the tested groups are not equal). A negative result indicates failure to reject the null hypothesis at the 5% significance level (medians of the tested groups are equal). When the difference between group medians is statistically significant, then the medians are compared. Whether the subjective quality evaluation in a certain group is significantly lower or higher than in another group is thus determined and a hypothesis can be rejected or accepted.

Based on visual inspection of Fig. 5.2 and Fig. 5.3, IMR L2BR reconstruction always provides data with the greatest improvement in image quality with respect to FBP reconstruction with a 80% dose. *Hypothesis 1* is thus formulated to be able mutually to compare subjective quality evaluations of IMR L2BR reconstruction with the other tested reconstruction types.

To accept or reject *Hypothesis 1*, subjective evaluations of data reconstructed using the IMR L2BR algorithm are tested against data for the other reconstruction types within corresponding patient groups and corresponding image quality parameters.

The goal of testing *Hypothesis 2* is to find out for which subjectively evaluated quality parameter IMR L2BR reconstruction has the best performance (i.e. for which subjective image quality parameter is the evaluation, and thus improvement in image quality with respect to FBP reconstruction with a 80% dose, highest). According to the presented heat maps, the IMR L2BR algorithm shows the best performance in reducing noise. Subjective evaluations are thus compared with evaluation of the noise parameter in a similar manner as in the previous case.

Hypothesis 2 states the following: IMR L2BR reconstruction has the best performance in noise suppression (tested against selected technical quality parameters for each patient group).

Results of the proposed hypotheses testing are summarized in Sec. 6.

6 RESULTS

Some of the minor results (such as the evaluation of precision and computational requirements of the stair-step error correction or the evaluation of positive effects of 2D SAW to the errors in 1D NPS estimation forced by tissues segmentation) were presented in the previous chapters. However, the results representing the crucial outcome of the thesis are presented in this section and are discussed in Sec. 7.

The results of analyzes undertaken in framework of the iDose[4] project are divided into two parts. Results of the analysis of standard deviation of residual noise are firstly presented followed by the results of analysis of noise frequency properties stability.

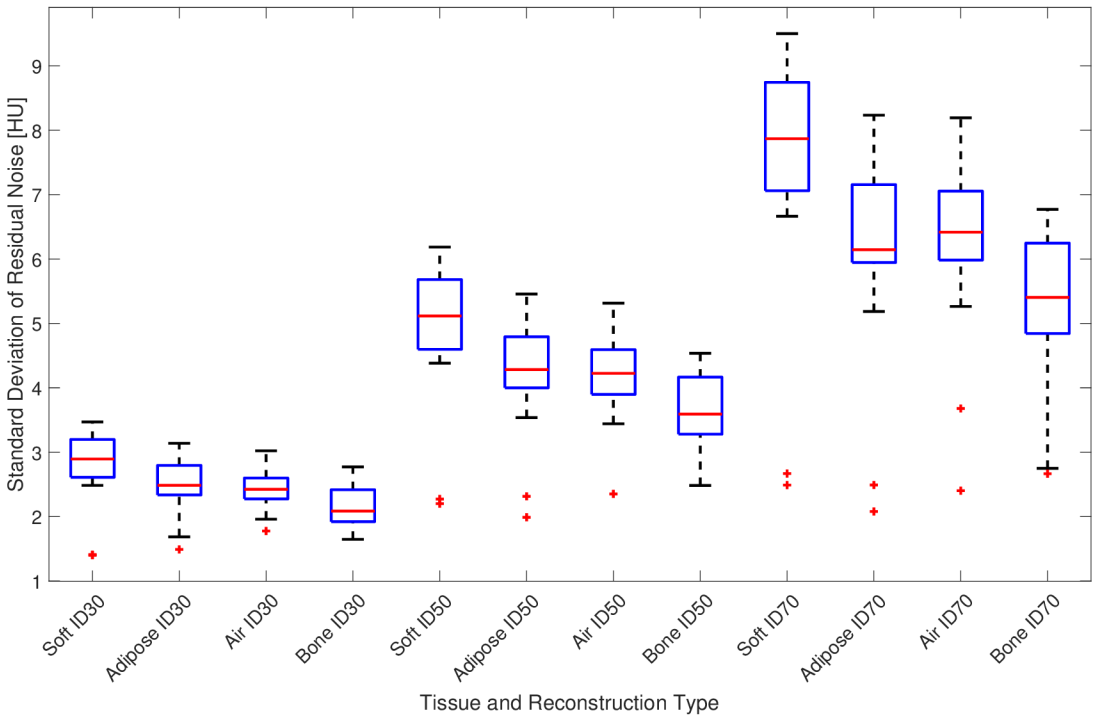

Obr. 6.1: Box plots of residual noise standard deviations computed from the whole set of patient data, in dependence on iDose[4] level and imaged tissue. The central red line is a median, blue horizontal edges of box are 25th and 75th percentiles, dashed lines cover extent of the most extreme points and red crosses indicate outliers.

A standard deviation of residual noise which is proportional to reduction of level of image noise in iteratively reconstructed data with respect to data reconstructed by FBP were established in Sec. 4.2. Box plots, calculated from the whole data set of differently reconstructed brain scans, showing standard deviations of residual noise as dependent on ID level and tissue type are depicted in Fig. 6.1. As already shown, higher standard deviation of residual noise indicates higher degree of image

noise reduction. A rising trend of residual noise standard deviations in dependence of ID levels can be observed, which indicates lover content of radiological noise in images reconstructed with higher ID level. A degree of improvement of radiological noise level in iteratively reconstructed data is evidently dependent on an imaged tissue type. For each iDose^4 level, the greatest improvement of the image noise level is achieved in soft tissue and, on the other hand, the level of image noise is least improved in bones.

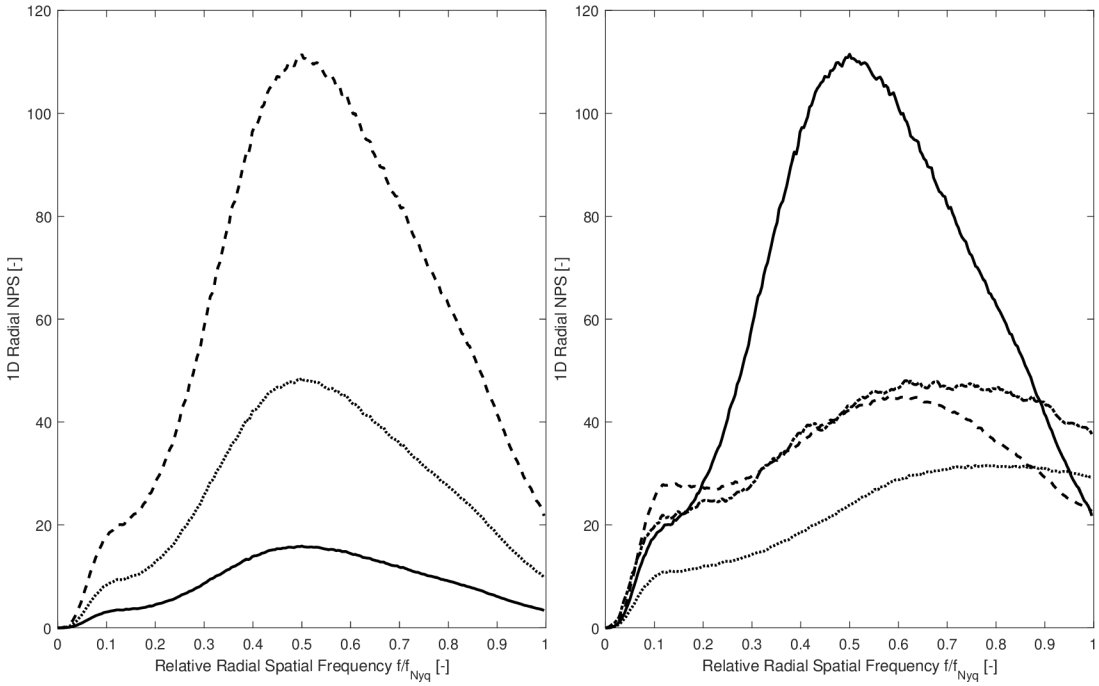

(a) (b)

Obr. 6.2: Examples of tissue 1D radial noise power spectra derived from a single patient data: (a) 1D NPS of soft tissue derived from data reconstructed by FBP (plotted by dashed line ($- - -$)), iDose^4 level 30 (plotted by dotted line ($\cdots$)) and iDose^4 level 50 (plotted by solid line (——)), (b) 1D NPS, derived from data reconstructed by iDose^4 level 30, typical for soft tissue (plotted by solid line (——)), air filled tissues (plotted by dash-dotted line ($\cdot - \cdot$)), adipose tissue (plotted by dashed line ($- - -$)) and bones (plotted by dotted line ($\cdots$)).

As already mentioned, iDose^4 method should not significantly change the spectral properties of noise in reconstructed data compared to FBP reconstruction. This statement was confirmed on the undertaken phantom study, see results in Tab. 4.4. However, thanks to the proposed methodology, 1D NPS, and thus the index of stability of noise frequency properties, can be evaluated in diverse tissues of real patient

data. Examples of tissue 1D NPS derived from soft tissue of data reconstructed by FBP (i.e. residual noise matrix FBP - ID70), iDose^4 level 30 and iDose^4 level 50 are depicted in Fig. 6.2a. Visually, centroids of 1D NPS curves in Fig. 6.2a are not significantly varying. Results of the evaluation of noise frequency properties stability in the real patient data, calculated according to the methodology proposed in Sec. 4.3, are summarized in Tab. 6.1. Their comparison with the stability indexes measured on the imaged phantom (summarized in Tab. 4.4) can be done. It can be concluded that the results measured on the imaged phantom are comparable with those calculated from real patient data (with exception of bones whose densities are, however, far from densities of water, where nonlinear iterative methods may have different properties). The proposed methodology is, thus, validated by phantom measurements for soft, adipose and air filled tissues.

Tab. 6.1: Results of analysis of 1D NPS center of gravity stability evaluated according to Eq. 4.12 separately for diverse tissues and iDose^4 levels.

	Soft	Bones	Adipose	Air Filled
iDose 30	0.198 ± 0.056	0.519 ± 0.181	0.345 ± 0.198	0.326 ± 0.205
iDose 50	0.513 ± 0.152	0.525 ± 0.172	0.659 ± 0.215	0.536 ± 0.235

Based on the presented results, it can be concluded that the stability of noise frequency properties measured on phantoms is worse for higher iDose^4 level. The identical effect can be observed when the stability is computed from real patient data (with exception of bones where the difference between stabilities of the considered iDose^4 levels is very small). Stability of noise frequency properties of data reconstructed by iDose^4 with level 50 are much less dependent on a tissue type than of data reconstructed by iDose^4 with level 30. Frequency properties of noise inherent to soft tissue are least influenced by iterative reconstruction compared to classical FBP method (i.e. have the best stability of noise frequency properties).

Tab. 6.2: Results of analysis of 1D NPS centers of gravity evaluated according to Eq. 4.11 separately for diverse tissues.

	Bones	Air Filled Tissue	Adipose Tissue	Soft Tissue
iDose 30	0.578 ± 0.018	0.546 ± 0.017	0.519 ± 0.011	0.520 ± 0.022

Besides evaluation of the stability of noise frequency properties among iDose^4 levels, proposed method enables also comparison of noise frequency properties among separate basic tissues. CoG of tissue 1D NPS calculated according to Eq. 4.11 are, rather than the stability indexes, this time compared. Examples of tissue 1D NPS

derived from diverse tissues of a single residual noise data (ID30 - ID70) are depicted in Fig. 6.2b. Based on its visual inspection, it is evident that noise in iteratively reconstructed CT data is "tissue dependent" i.e. its frequency properties are dependent on tissue type in which the noise is located. The results of CoG measurement of 1D NPS in diverse tissues of residual noise data ID 30 are summarized in Tab. 6.2. Based on the presented results, it can be concluded that noise in bones is composed of higher frequency components than noise in the rest of tested tissues. Comparing spectral properties of noise typical for adipose and soft tissue, it can be concluded that there is not a significant difference. This fact can be explained by similar character (they have very similar densities in CT scans) of both tissues.

Results of "The IMR project", which was focused on measurement of CT image quality in terms of fidelity of anatomical structures reconstruction via evaluation of mean density in segmented airways are depicted in Fig. 6.3 in form of box plots. The box plots express distribution of mean density (calculated for whole considered data set) in differently thick airways parts, in data reconstructed by diverse methods and acquired with different level of dose reduction. Based on the presented results,

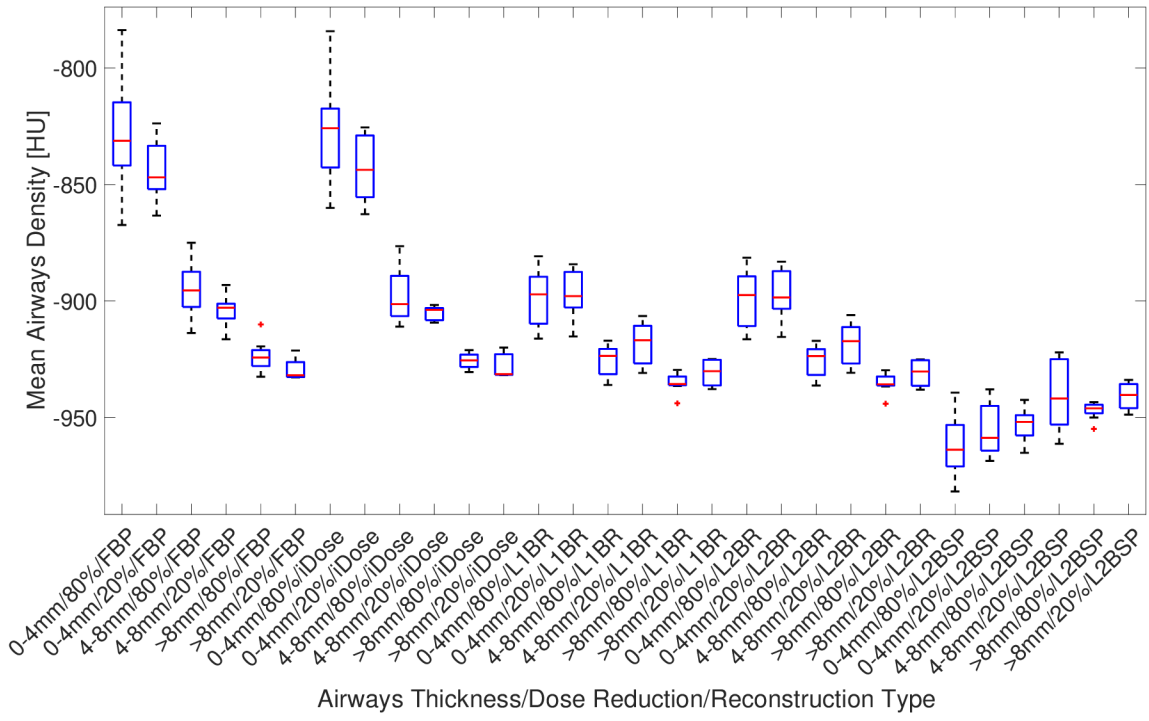

Obr. 6.3: Quality of differently reconstructed data evaluated via fidelity of airways tree reconstruction visualized in form of box plots. Each box plot express distribution of the image quality parameter for different airways thickness, reconstruction type and dose reduction.

several interesting conclusion are made. The qualities of anatomical structures reconstruction are nearly identical in data reconstructed by FBP and iDose^4 method for each airways thickness and level of dose reduction. This result is consistent with initial assumption that iDose^4 is pure statistical method which improves level of image noise (compared to the data reconstructed by FBP) and do not influence visualization of anatomical structures. On the other hand, model based iterative reconstruction types (labeled as L1BR, L2BR and L2BR) show significant increase of airways reconstruction quality (up to 130 HU lower mean density in L2BSP reconstructed data compared with by FBP reconstructed data). Those results support the initial assumption stating that model based iterative reconstruction positively influences fidelity of anatomical structures reconstruction. As data with different level of dose reduction are available, influence of applied dose can also be evaluated. No dramatic changes in fidelity of airways reconstruction can be observed, after reduction of applied dose from 80% to 20%. Considering FBP and iDose^4 reconstructions there is a slight improvement of image quality and, on the contrary, a slight decrease can be observed in data reconstructed by IMR. Analysis of airways based image quality measurements in dependence of airways thickness gives also very interesting results. Mean airways density increases (image quality decreases) with decreasing airways thickness for FBP, iDose^4 and also (though not so rapidly) for L1BR and L2BR reconstructions. Those reconstruction types are, hence, unable to maintain quality of reconstruction of small objects compared to larger ones. On the contrary, this trend is opposite in data reconstructed by L2BSP which provides data where quality of thin airways is even better than quality of the thicker ones. An interesting result is also that model based reconstruction types L1BR and L2BR provide for airways with large thickness (larger than 8 mm) similar quality data as FBP and iDose^4 but quality of those reconstructions (compared to FBP and iDose^4) rapidly increase in thinner branches.

A subjective medical evaluation of four image quality parameters was described in Sec. 5.3. Based on visualization of the quality evaluations in form of heat maps, two hypotheses were established and tested by Wilcoxon rank-sum test. As a result of this statistical analysis, it can be concluded that the greatest improvement in image quality with respect to quality of FBP reconstruction with 80% dose is always achieved with IMR L2BR reconstruction (nearly for each patient group and considered image quality parameter), which can, thus, be recommended as the optimal choice for the best quality CT image reconstruction among the tested algorithms. Considering the quality parameters Sharpness and Details, IMR L2BSP reconstruction type has, in several patient groups, slightly higher median than does IMR L2BR, but these differences are not statistically significant.

As a result of statistical testing of *Hypothesis 2*, it can be concluded that, there

are no statistically significant differences between subjective evaluations of the parameters Noise and Artifacts. Meanwhile, differences between the Noise parameter and the rest of the selected technical parameters are statistically significant (whereas subjective evaluation of the Noise parameter is higher by a statistically significant amount). It can be concluded that IMR L2BR reconstruction has the best performance among the tested image quality parameters in reducing image noise and artifacts.

A novel measure of image quality of anatomical structures reconstruction in terms of fidelity of airways reconstruction is presented in Sec. 5. As a subjective medical image quality evaluation of details in identical data set is also available, those two measures can be compared. The comparison may reveal whether the proposed objective image quality assessment (quality of the thinner airways are used to simulate evaluation of fine details) have potential to become a fully automatic method for evaluation of quality of anatomical details reconstruction in CT data.

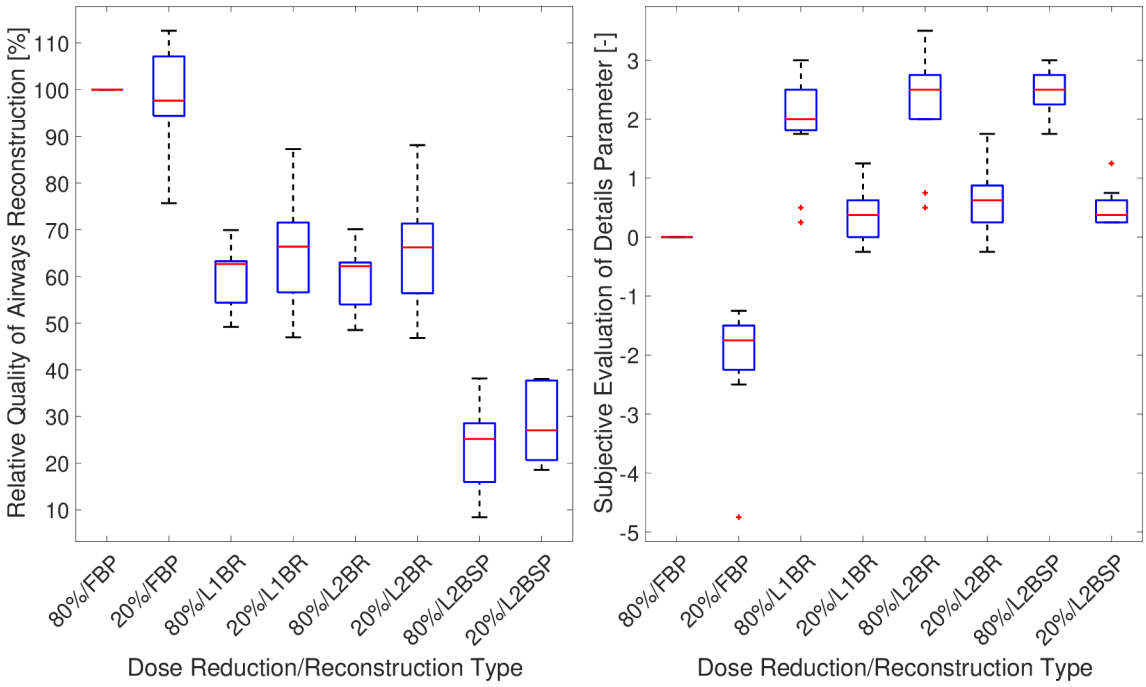

Obr. 6.4: Subjective and objective image quality measurements in form of box plots. Each box plot express distribution of image quality for different reconstruction of data acquired with diverse dose reduction: (a) Objective measurements of mean density of airways parts thinner than 4 mm expressed relatively with respect to quality of data acquired with 80% dose and reconstructed by FBP, (b) subjective medical evaluations of Details parameter.

In or order to be consistent with the objective medical image quality evaluation (described in Sec. 5.3) where quality of iteratively reconstructed data were assessed relatively compared to quality of by FBP reconstructed data acquired with 80% dose, objective evaluations are accordingly recalculated. Mean value of HU inside airways is recalculated as a percentage, taking the mean of HU inside airways in by FBP reconstructed data with a 80% dose as 100% of image quality. Hence, e.g. 50% of quality of airways reconstruction means that mean value of HU in airways is about 50% lower than in by FBP reconstructed data acquired with 80% dose.

Both compared quality measurements are visualized in form of box plots in Fig. 6.4. It is evident that objective and subjective quality measurements agree in the following facts. Increase of image quality in iteratively reconstructed data acquired with 80% dose is evident in both evaluations. Subjective evaluations of data acquired with 20% dose shows decrease of image quality (compared to correspondingly reconstructed 80% scans) as well as the objective ones (though not so dramatic). On the other hand, results of the subjective evaluations show no significant changes in image quality among different types of IMR reconstruction method (L1BR, L2BR, L2BSP), however, according to the objective evaluation, L2BSP reconstruction type provides much better image quality than the other two types.

7 DISCUSSION

The methodology for estimation of noise characteristics (namely standard deviation and noise power spectrum) from separate tissues of real patient data is established in the first part of this thesis. Though the proposed method provides, for computations of stability of noise frequency properties, similar results as on the phantom data (hence, it may be considered validated by phantom measurements), some issues have to be discussed. Firstly, the extraction method was not validated for bones, which may be caused by greatly different densities of bones and water in used homogeneous phantom. Nonlinear iterative method may have different properties while reconstructing densities of bones and water. It does not mean that the proposed method for tissue noise power spectrum estimation does not work well for bones. A phantom with homogeneous material which simulates densities of bones would be needed for its proper validation.

Secondly, for adipose and air filled tissues, segmentation introduced errors are too high to declare tissue noise power spectrum estimation reliable for purposes of measurement of noise frequency properties stability in real patient data reconstructed by iDose^4. It is supposed that low spatial extent of those tissue types is the limiting factor.

Subtraction of differently reconstructed data which moreover must have noise power spectra with similar shape (otherwise an error caused by the subtraction described in Sec. 4.3 would increase) is necessary, which is also an evident limiting factor for general utilization of the proposed method. However, it have a great potential in estimation of tissue noise power spectrum from data acquired by dual energy scanners. As dual energy scanners provide a couple of simultaneously scanned data with different noise realizations, anatomical structures may be, potentially, better suppressed by their subtraction and no errors caused by subtraction should occur.

Proposed detection of areas of dominant radiological noise, which is very sensitive to setting of parameters of graph-cut based segmentation, may be considered another limiting factor. The parameters are constant for a given data set, but they, probably, need to be tuned when e.g. different iterative reconstruction method is used. Fig. 4.7 shows that detection of areas of dominant radiological noise largely increases rotational symmetry of estimated 2D tissue noise power spectra, however perfect rotational symmetry is still not achieved. Better rotational symmetry would be achieved by tuning of the parameters of dominant radiological noise areas detection algorithm. Detection of more gentle directional structures will, on the other hand, produce the tissue segmentation masks with more complicated shape; this will lead to increased segmentation introduced errors. A compromise parameters tuning,

thus, have to be searched for each specific application.

According to the results in Tab. 6.1, an increasing trend of stability indexes (i.e. worse preservation of noise frequency properties) may be observed with increasing iDose^4 level. However, this dependence should be confirmed on a wider range of iDose^4 levels, which were, unfortunately, not available.

A novel CT image quality measure which evaluates quality of anatomical structures reconstruction via fidelity of airways reconstruction is proposed in the second part of this thesis. As stated in Sec. 6, results of this analysis performed on the set of real patient data are consistent with initial assumptions about capabilities of the considered reconstruction methods as provided by the vendor. From this point of view, it can be concluded that the proposed parameter is a valuable measure of image quality in terms of fidelity of high contrast anatomical structures reconstruction.

However, some discrepancies between subjective medical evaluation of Details parameter and objective measurement of fidelity of airways reconstruction were revealed. The objective measurements shows a rapid increase of image quality of by IMR L2BSP reconstructed data, which can not be observed in the objective evaluation. Medical experts may rather focus their attention to gentle structures which have low contrast to surrounding tissues, but airways are mostly well visible structures with good contrast to surrounding lung parenchyma. Moreover, medical experts evaluate details in whole volume of CT data and proposed objective image quality parameter is calculated only from airways.

Another discrepancy can be seen in evaluations of qualities of 20% dose scans which are much lower in subjective than in objective assessments. The subjective evaluations were not blinded which may cause that medical experts may intuitively falsely assign lower quality points to 20% dose scans. Another explanation may be, again, that medical experts focus their attention to structures with lower contrast to surrounding tissues than the airways have.

8 CONCLUSIONS

This thesis deals with measurement of image quality of iteratively reconstructed CT data and its comparison with the quality of data reconstructed by so far routinely used filtered back projection method. Recently published studies undertaken on special phantoms revealed that iteratively reconstructed data have some special properties (e.g. object dependent noise properties). Hence, some image quality measurements so far used in analysis of CT data have to be revised. Design of novel CT image quality parameters which respect specifics of iteratively reconstructed data and are fully automatically computed directly from real patient data is the main objective of this thesis. This thesis is divided into two main parts, in which data reconstructed by diverse methods are analyzed and different novel image quality parameters are proposed.

A novel methodology for estimation of tissue noise power spectrum which complexly describes frequency properties of noise inherent to separate tissues is presented in the first part; this methodology represents the crucial contribution of this thesis. It was demonstrated that noise in iteratively reconstructed data is object dependent in real patient data, which is the fact so far known only from phantom data. Frequency shift of 1D NPS center of gravity in by iDose^4 method reconstructed data (compared to 1D NPS center of gravity of the data reconstructed by FBP) was also evaluated. It was shown that iDose^4 method almost perfectly maintains spectral properties (and also texture) of image noise in all considered tissue types.

An extensive data processing was necessary for estimation of tissue noise power spectrum such as fully data driven gantry tilt correction, segmentation of cranial base and determination of areas of dominant radiological noise in residual noise images. All proposed data processing approaches may be, generally, utilized in other applications. Another important contribution of this thesis is represented by the methodology for design of two-dimensional spatially adaptive windowing functions, which are useful in applications where two-dimensional Fourier transform have to be calculated from a spatially limited subset of image data with irregular shape (e.g. from segmented data).

An approach for evaluation of quality of anatomical structures reconstruction via fidelity of airways reconstruction is presented in the second part. Results of the quality of airways reconstruction measured on real patient data are consistent with initial assumptions about the tested iterative reconstruction methods as provided by the vendor. However, some discrepancies between the proposed objective image quality measurement and subjective medical evaluation of details in corresponding set of CT data were revealed. Hence, it can be considered a valuable measure of quality of reconstruction of high contrast anatomical structures such as airways.

The proposed parameter, fidelity of airways reconstruction, therefore, can not be considered a general measure of quality of details reconstruction in CT data. It was shown that IMR reconstruction method rapidly increase quality of thin airways reconstruction compared to FBP and iDose^4 methods.

BIBLIOGRAPHY

[1] ANTOINE, J. P., R. MURENZI: Two-dimensional directional wavelets and the scale-angle representation. *Signal Processing*, 1996, Vol. 52, no. 3: pp. 259–281, ISSN 01651684.

[2] ANTOINE, J. P., R. MURENZI, P. VANDERGHEYNST: Directional Wavelets Revisited: Cauchy Wavelets and Symmetry Detection in Patterns. *Applied and Computational Harmonic Analysis*, 1999, Vol. 6: pp. 314–345, ISSN 10635203.

[3] ANTOINE, J. P., P. VANDERGHEYNST, R. MURENZI: Two-dimensional directional wavelets in image processing. *International Journal of Imaging Systems and Technology*, 1996, Vol. 7, no. 3: pp. 152–165, ISSN 0899-9457.

[4] ARAPAKIS, I., E. EFSTATHOPOULOS, V. TSITSIA, S. KORDOLAIMI, N. ECONOMOPOULOS, et al.: Using "iDose4"iterative reconstruction algorithm in adults' chest-abdomen-pelvis CT examinations: Effect on image quality in relation to patient radiation exposure. *British Journal of Radiology*, 2014, Vol. 87, no. 1036, ISSN 00071285.

[5] AYKAC, Deniz, Eric a HOFFMAN, Geoffrey MCLENNAN, Joseph M REINHARDT: Segmentation and analysis of the human airway tree from three-dimensional X-ray CT images. *IEEE transactions on medical imaging*, aug 2003, Vol. 22, no. 8: pp. 940–50, ISSN 0278-0062.

[6] BARRETT, Julia F., Nicholas KEAT: Artifacts in CT: recognition and avoidance. *Radiographics : a review publication of the Radiological Society of North America, Inc*, 2004, Vol. 24, no. 6: pp. 1679–91, ISSN 1527-1323.

[7] BEISTER, Marcel, Daniel KOLDITZ, Willi A. KALENDER: Iterative reconstruction methods in X-ray CT. *Physica medica : PM : an international journal devoted to the applications of physics to medicine and biology : official journal of the Italian Association of Biomedical Physics (AIFB)*, apr 2012, Vol. 28, no. 2: pp. 94–108, ISSN 1724-191X.

[8] BENÍTEZ, Ricardo Betancourt, Ruola NING, David CONOVER, Shaohua LIU: NPS characterization and evaluation of a cone beam CT breast imaging system. *Journal of X-ray science and technology*, jan 2009, Vol. 17, no. 1: pp. 17–40, ISSN 1095-9114.

[9] BLUM, Harry, Roger N. NAGEL: Shape description using weighted symmetric axis features. *Pattern Recognition*, jan 1978, Vol. 10, no. 3: pp. 167–180, ISSN 00313203.

[10] BOAS, F Edward, Dominik FLEISCHMANN: CT artifacts: causes and reduction techniques. *Imaging in Medicine*, apr 2012, Vol. 4, no. 2: pp. 229–240, ISSN 1755-5191.

[11] BOEDEKER, K. L., V. N. COOPER, M. F. MCNITT-GRAY: Application of the noise power spectrum in modern diagnostic MDCT: part I. Measurement of noise power spectra and noise equivalent quanta. *Physics in medicine and biology*, 2007, Vol. 52, no. 14: pp. 4027–46, ISSN 0031-9155.

[12] BOYKOV, Y.Y., M.-P. JOLLY: Interactive graph cuts for optimal boundary & region segmentation of objects in N-D images. In *Proceedings Eighth IEEE International Conference on Computer Vision. ICCV 2001*, Vol. 1, IEEE Comput. Soc, ISBN 0-7695-1143-0, pp. 105–112.

[13] CANNY, John: A computational approach to edge detection. *IEEE transactions on pattern analysis and machine intelligence*, jun 1986, Vol. 8, no. 6: pp. 679–98, ISSN 0162-8828.

[14] CERVINKOVA, Ivana, Petr WALEK, Igor JIRA: Possibilities of Reducing Radiation Dose in Computed Tomography Examinations in Various Age Groups Using an Iterative Model-Based Reconstruction Technique. *Pediatrics & Therapeutics*, 2016, Vol. 06, no. 04, ISSN 21610665.

[15] CHARBONNIER, Jean Paul, Eva M.van RIKXOORT, Arnaud A.A. SETIO, Cornelia M. SCHAEFER-PROKOP, Bram VAN GINNEKEN, et al.: Improving airway segmentation in computed tomography using leak detection with convolutional networks. *Medical Image Analysis*, 2017, Vol. 36: pp. 52–60, ISSN 13618423.

[16] CHOI, Wai-Pak, Kin-Man LAM, Wan-Chi SIU: Extraction of the Euclidean skeleton based on a connectivity criterion. *Pattern Recognition*, mar 2003, Vol. 36, no. 3: pp. 721–729, ISSN 00313203.

[17] CHOO, Ji Yung, Jin Mo GOO, Chang Hyun LEE, Chang Min PARK, Sang Joon PARK, et al.: Quantitative analysis of emphysema and airway measurements according to iterative reconstruction algorithms: Comparison of filtered back projection, adaptive statistical iterative reconstruction and model-based iterative reconstruction. *European Radiology*, 2014, Vol. 24, no. 4: pp. 799–806, ISSN 14321084.

[18] DELMON, V., S. RIT, R. PINHO, D. SARRUT: Registration of sliding objects using direction dependent B-splines decomposition. *Physics in medicine and biology*, 2013, Vol. 58, no. 5: pp. 1303–1314, ISSN 13616560.

[19] DUDA, Richard O., Peter E. HART: Use of the Hough transformation to detect lines and curves in pictures. *Communications of the ACM*, jan 1972, Vol. 15, no. 1: pp. 11–15, ISSN 00010782.

[20] EULER, André, Bram STIELTJES, Zsolt SZUCS-FARKAS, Reto EICHENBERGER, Clemens REISINGER, et al.: Impact of model-based iterative reconstruction on low-contrast lesion detection and image quality in abdominal CT: a 12-reader-based comparative phantom study with filtered back projection at different tube voltages. *European Radiology*, 2017: pp. 1–8, ISSN 14321084.

[21] FAULKNER, K., B. M. MOORES: Analysis of x-ray computed tomography images using the noise power spectrum and autocorrelation function. *Physics in medicine and biology*, nov 1984, Vol. 29, no. 11: pp. 1343–52, ISSN 0031-9155.

[22] FLEISCHMANN, Dominik, F. Edward BOAS: Computed tomography–old ideas and new technology. *European radiology*, mar 2011, Vol. 21, no. 3: pp. 510–7, ISSN 1432-1084.

[23] FOROOSH, H, J.B. ZERUBIA, M BERTHOD: Extension of phase correlation to subpixel registration. *IEEE Transactions on Image Processing*, mar 2002, Vol. 11, no. 3: pp. 188–200, ISSN 10577149.

[24] FUNAMA, Yoshinori, Katsuyuki TAGUCHI, Daisuke UTSUNOMIYA, Seitaro ODA, Yumi YANAGA, et al.: Combination of a low-tube-voltage technique with hybrid iterative reconstruction (iDose) algorithm at coronary computed tomographic angiography. *Journal of computer assisted tomography*, 2012, Vol. 35, no. 4: pp. 480–5, ISSN 1532-3145.

[25] GECKINLI, N., D. YAVUZ: Some novel windows and a concise tutorial comparison of window families. *IEEE Transactions on Acoustics, Speech, and Signal Processing*, dec 1978, Vol. 26, no. 6: pp. 501–507, ISSN 0096-3518.

[26] GERVAISE, Alban, Benoît OSEMONT, Sophie LECOCQ, Alain NOEL, Emilien MICARD, et al.: CT image quality improvement using Adaptive Iterative Dose Reduction with wide-volume acquisition on 320-detector CT. *European radiology*, feb 2012, Vol. 22, no. 2: pp. 295–301, ISSN 1432-1084.

[27] GEUSEBROEK, Jan Mark, Arnold W. M. SMEULDERS, Joost VAN DE WEIJER: Fast Anisotropic Gauss Filtering. *IEEE Transactions on Image Processing*, 2003, Vol. 12, no. 8: pp. 938–943, ISSN 10577149.

[28] GHADIMI, Sona, Hamid ABRISHAMI MOGHADDAM, Reinhard GREBE, Fabrice WALLOIS: Skull Segmentation and Reconstruction From Newborn CT Images Using Coupled Level Sets. *IEEE Journal of Biomedical and Health Informatics*, 2016, Vol. 20, no. 2: pp. 563–573, ISSN 21682194.

[29] GHETTI, C., O. ORTENZIA, G. SERRELI: CT iterative reconstruction in image space: A phantom study. *Physica medica : PM : an international journal devoted to the applications of physics to medicine and biology : official journal of the Italian Association of Biomedical Physics (AIFB)*, apr 2012, Vol. 28, no. 2: pp. 161–5, ISSN 1724-191X.

[30] GOLDMAN, Lee W.: Principles of CT: radiation dose and image quality. *Journal of nuclear medicine technology*, dec 2007, Vol. 35, no. 4: pp. 213–25; quiz 226–8, ISSN 0091-4916.

[31] GOO, Hyun Woo: CT Radiation Dose Optimization and Estimation: an Update for Radiologists. *Korean journal of radiology : official journal of the Korean Radiological Society*, jan 2012, Vol. 13, no. 1: pp. 1–11, ISSN 2005-8330.

[32] GOPAL, Arun, Sanjiv S. SAMANT: Use of a line-pair resolution phantom for comprehensive quality assurance of electronic portal imaging devices based on fundamental imaging metrics. *Medical physics*, 2009, Vol. 36, no. 6: pp. 2006–2015, ISSN 00942405.

[33] GORDIC, S., L. DESBIOLLES, P. STOLZMANN, L. GANTNER, S. LESCHKA, et al.: Advanced modelled iterative reconstruction for abdominal CT: Qualitative and quantitative evaluation. *Clinical Radiology*, 2014, Vol. 69, no. 12: pp. e497–e504, ISSN 1365229X.

[34] GRAHAM, Michael W., Jason D. GIBBS, Duane C. CORNISH, William E. HIGGINS: Robust 3-D airway tree segmentation for image-guided peripheral bronchoscopy. *IEEE Transactions on Medical Imaging*, 2010, Vol. 29, no. 4: pp. 982–997, ISSN 02780062.

[35] GUPTA, S. K.: Peak Decomposition using Pearson Type VII Function. *Journal of Applied Crystallography*, 1998, Vol. 31, no. 3: pp. 474–476, ISSN 00218898.

[36] HAGAN, Martin T., Mohammad B. MENHAJ: Training Feedforward Networks with the Marquardt Algorithm. *IEEE Transactions on Neural Networks*, 1994, Vol. 5, no. 6: pp. 989–993, ISSN 19410093.

[37] HANSON, K. M.: Detectability in computed tomographic images. *Medical physics*, 1979, Vol. 6, no. 5: pp. 441–51, ISSN 0094-2405.

[38] HARALICK ROBERT, M., G. LINDA, SHAPIRO: *Computer and robot vision*. Reading: Mass.: Addison-Wesley Pub. Co, second edition, 1992, ISBN 02015694342.

[39] HARRIS, F.J.: On the use of windows for harmonic analysis with the discrete Fourier transform. *Proceedings of the IEEE*, 1978, Vol. 66, no. 1: pp. 51–83, ISSN 0018-9219.

[40] HARTIGAN, J. A., M. A. WONG: A K-Means Clustering Algorithm. *Applied Statistics*, 1979, Vol. 28, no. 1: p. 100, ISSN 00359254.

[41] HELL, Michaela M., Daniel BITTNER, Annika SCHUHBAECK, Gerd MUSCHIOL, Michael BRAND, et al.: Prospectively ECG-triggered high-pitch coronary angiography with third-generation dual-source CT at 70 kVp tube voltage: Feasibility, image quality, radiation dose, and effect of iterative reconstruction. *Journal of Cardiovascular Computed Tomography*, 2014, Vol. 8, no. 6: pp. 418–425, ISSN 1876861X.

[42] HILDEBRAND, T., P. RUEGSEGGER: A new method for the model-independent assessment of thickness in three-dimensional images. *Journal of Microscopy*, jan 1997, Vol. 185, no. 1: pp. 67–75, ISSN 0022-2720.

[43] HOU, Yang, Shu XU, Wenli GUO, Mani VEMBAR, Qiyong GUO: The optimal dose reduction level using iterative reconstruction with prospective ECG-triggered coronary CTA using 256-slice MDCT. *European journal of radiology*, dec 2012, Vol. 81, no. 12: pp. 3905–11, ISSN 1872-7727.

[44] HU, X. H., X. F. DING, R. Z. WU, M. M. ZHANG: Radiation dose of non-enhanced chest CT can be reduced 40% by using iterative reconstruction in image space. *Clinical radiology*, nov 2011, Vol. 66, no. 11: pp. 1023–9, ISSN 1365-229X.

[45] IPPOLITO, Davide, Alessandra Silvia CASIRAGHI, Cammillo Talei FRANZESI, Davide FIOR, Franca MELONI, et al.: Low-dose computed tomography

with 4th-generation iterative reconstruction algorithm in assessment of oncologic patients. *World Journal of Gastrointestinal Oncology*, 2017, Vol. 9, no. 10: pp. 423–430, ISSN 1948-5204.

[46] JAFARIAN, Nassim, Kamran KAZEMI, Hamid ABRISHAMI MOGHADDAM, Reinhard GREBE, Marc FOURNIER, et al.: Automatic segmentation of newborns' skull and fontanel from CT data using model-based variational level set. *Signal, Image and Video Processing*, 2014, Vol. 8, no. 2: pp. 377–387, ISSN 18631703.

[47] JAN, Jiri: *Digital Signal Filtering, Analysis and Restoration*. Brno: VUTIUM, 2000, 407 pp., ISBN 0-8529-6760-8.

[48] JAN, Jiri: *Medical image processing, reconstruction and restoration: concepts and methods*. Boca Raton: Taylor & Francis, 2006, 730 pp., ISBN 0-8247-5849-8.

[49] JANC, K., J. TARASIUK, A. S. BONNET, P. LIPINSKI: Genetic algorithms as a useful tool for trabecular and cortical bone segmentation. *Computer Methods and Programs in Biomedicine*, 2013, Vol. 111, no. 1: pp. 72–83, ISSN 01692607.

[50] JIRA, Igor, Petr OUREDNICEK, Jarmila SKOTAKOVA, Petr WALEK, Tomas JATEL, et al.: První zkusenosti s hybridni iterativní technikou iDose pri CT vysetrovani mozku u deti, adolescentu a dospelych. *Česká radiologie*, 2012, Vol. 66, no. 1: pp. 18–22.

[51] KADOOKA, K., K. KUNOO, N. UDA, K. ONO, T. NAGAYASU: Strain analysis for moiré interferometry using the two-dimensional continuous wavelet transform. *Experimental Mechanics*, mar 2003, Vol. 43, no. 1: pp. 45–51, ISSN 0014-4851.

[52] KALMAR, Peter I., Franz QUEHENBERGER, Jürgen STEINER, Andre LUTFI, Dennis BOHLSEN, et al.: The impact of iterative reconstruction on image quality and radiation dose in thoracic and abdominal CT. *European Journal of Radiology*, 2014, Vol. 83, no. 8: pp. 1416–1420, ISSN 18727727.

[53] KANG, Yan, Klaus ENGELKE, Willi A. KALENDER: A new accurate and precise 3-D segmentation method for skeletal structures in volumetric CT data. *IEEE transactions on medical imaging*, may 2003, Vol. 22, no. 5: pp. 586–98, ISSN 0278-0062.

[54] KIJEWSKI, M. F., P. F. JUDY: The noise power spectrum of CT images. *Physics in medicine and biology*, may 1987, Vol. 32, no. 5: pp. 565–75, ISSN 0031-9155.

[55] KIRALY, Atilla P., William E. HIGGINS, Geoffrey MCLENNAN, Eric A. HOFFMAN, Joseph M. REINHARDT: Three-Dimensional Human Airway Segmentation Methods for Clinical Virtual Bronchoscopy. *Academic Radiology*, oct 2002, Vol. 9, no. 10: pp. 1153–1168, ISSN 10766332.

[56] KLEIN, S., M. STARING, J. P. W. PLUIM: Evaluation of Optimization Methods for Nonrigid Medical Image Registration Using Mutual Information and B-Splines. *IEEE Transactions on Image Processing*, 2007, Vol. 16, no. 12: pp. 2879–2890.

[57] KLEIN, Stefan, Josien P. W. PLUIM, Marius STARING, Max A. VIERGEVER: Adaptive Stochastic Gradient Descent Optimisation for Image Registration. *International Journal of Computer Vision*, aug 2008, Vol. 81, no. 3: pp. 227–239, ISSN 0920-5691.

[58] KLEIN, Stefan, Marius STARING, Keelin MURPHY, Max A. VIERGEVER, Josien P. W. PLUIM: Elastix: a Toolbox for Intensity-Based Medical Image Registration. *IEEE transactions on medical imaging*, jan 2010, Vol. 29, no. 1: pp. 196–205, ISSN 1558-0062.

[59] KRCAH, Marcel, Gabor SZEKELY, Remi BLANC: Fully automatic and fast segmentation of the femur bone from 3D-CT images with no shape prior. In *2011 IEEE International Symposium on Biomedical Imaging: From Nano to Macro*, IEEE, ISBN 978-1-4244-4127-3, pp. 2087–2090.

[60] KUMAR, Sanjay, Kulbir SINGH, Rajiv SAXENA: Analysis of Dirichlet and Generalized Hamming window functions in the fractional Fourier transform domains. *Signal Processing*, mar 2011, Vol. 91, no. 3: pp. 600–606, ISSN 01651684.

[61] LEIPSIC, Jonathon, Troy M. LABOUNTY, Brett HEILBRON, James K. MIN, G. B. John MANCINI, et al.: Adaptive statistical iterative reconstruction: assessment of image noise and image quality in coronary CT angiography. *AJR. American journal of roentgenology*, sep 2010, Vol. 195, no. 3: pp. 649–54, ISSN 1546-3141.

[62] LEUTZ-SCHMIDT, Patricia, Oliver WEINHEIMER, Bertram J. JOBST, Julien DINKEL, Jürgen BIEDERER, et al.: Influence of exposure parameters

and iterative reconstruction on automatic airway segmentation and analysis on MDCT - An ex vivo phantom study. *PLoS ONE*, 2017, Vol. 12, no. 8: pp. 1–14, ISSN 19326203.

[63] LI, Ke, Nicholas BEVINS, Joseph ZAMBELLI, Guang-Hong CHEN: Fundamental relationship between the noise properties of grating-based differential phase contrast CT and absorption CT: Theoretical framework using a cascaded system model and experimental validation. *Medical Physics*, 2013, Vol. 40, no. 2: p. 021908, ISSN 00942405.

[64] LI, Ke, John GARRETT, Yongshuai GE, Guang-Hong CHEN: Statistical model based iterative reconstruction (MBIR) in clinical CT systems. Part II. Experimental assessment of spatial resolution performance. *Medical Physics*, 2014, Vol. 41, no. 7: p. 071911, ISSN 00942405.

[65] LI, Q., H. YU, L. ZHANG, L. FAN, S-Y. LIU: Combining low tube voltage and iterative reconstruction for contrast-enhanced CT imaging of the chest-Initial clinical experience. *Clinical radiology*, feb 2013, Vol. 68: pp. 249–253, ISSN 1365-229X.

[66] LO, Pechin, Jon SPORRING, Haseem ASHRAF, Jesper J.H. PEDERSEN, M. DE BRUIJNE MARLEEN: Vessel-guided airway tree segmentation: A voxel classification approach. *Medical Image Analysis*, 2010, Vol. 14, no. 4: pp. 527–538, ISSN 13618415.

[67] LO, Pechin, Bram VAN GINNEKEN, Joseph M. REINHARDT, Tarunashree YAVARNA, Pim A. DE JONG, et al.: Extraction of airways from CT (EXACT'09). *IEEE Transactions on Medical Imaging*, 2012, Vol. 31, no. 11: pp. 2093–2107, ISSN 02780062.

[68] LÖVE, A., M.-L. OLSSON, R. SIEMUND, F. STÅLHAMMAR, I. M. BJÖRKMAN-BURTSCHER, et al.: Six iterative reconstruction algorithms in brain CT: a phantom study on image quality at different radiation dose levels. *The British Journal of Radiology*, 2013, Vol. 86, no. 1031: p. 20130388, ISSN 0007-1285.

[69] MARIN, Daniele, Rendon C. NELSON, Sebastian T. SCHINDERA, Samuel RICHARD, Richard S. YOUNGBLOOD, et al.: Low-tube-voltage, high-tube-current multidetector abdominal CT: improved image quality and decreased radiation dose with adaptive statistical iterative reconstruction algorithm–initial clinical experience. *Radiology*, jan 2010, Vol. 254, no. 1: pp. 145–53, ISSN 1527-1315.

[70] MARTIN, C. J., P. F. SHARP, D. G. SUTTON: Measurement of image quality in diagnostic radiology. *Applied radiation and isotopes : including data, instrumentation and methods for use in agriculture, industry and medicine*, jan 1999, Vol. 50, no. 1: pp. 21–38, ISSN 0969-8043.

[71] MARTINSEN, Anne Catrine Trægde, Hilde Kjernlie SÆTHER, Per Kristian HOL, Dag Rune OLSEN, Per SKAANE: Iterative reconstruction reduces abdominal CT dose. *European journal of radiology*, jul 2012, Vol. 81, no. 7: pp. 1483–7, ISSN 1872-7727.

[72] MCCOLLOUGH, Cynthia H., Andrew N. PRIMAK, Natalie BRAUN, James KOFLER, Lifeng YU, et al.: Strategies for reducing radiation dose in CT. *Radiologic clinics of North America*, jan 2009, Vol. 47, no. 1: pp. 27–40, ISSN 0033-8389.

[73] MENDONÇA, Ana Maria, Aurélio CAMPILHO: Segmentation of retinal blood vessels by combining the detection of centerlines and morphological reconstruction. *IEEE Transactions on Medical Imaging*, 2006, Vol. 25, no. 9: pp. 1200–1213, ISSN 02780062.

[74] MENG, Qier, Takayuki KITASAKA, Yukitaka NIMURA, Masahiro ODA, Junji UENO, et al.: Automatic segmentation of airway tree based on local intensity filter and machine learning technique in 3D chest CT volume. *International Journal of Computer Assisted Radiology and Surgery*, 2017, Vol. 12, no. 2: pp. 245–261, ISSN 18616429.

[75] METS, Onno M., Martin J. WILLEMINK, Freek P. L. DE KORT, Christian P. MOL, Tim LEINER, et al.: The effect of iterative reconstruction on computed tomography assessment of emphysema, air trapping and airway dimensions. *European radiology*, oct 2012, Vol. 22, no. 10: pp. 2103–9, ISSN 1432-1084.

[76] METZ, C. T., S. KLEIN, M. SCHAAP, T. VAN WALSUM, W. J. NIESSEN: Nonrigid registration of dynamic medical imaging data using nD + t B-splines and a groupwise optimization approach. *Medical image analysis*, apr 2011, Vol. 15, no. 2: pp. 238–49, ISSN 1361-8423.

[77] MIÉVILLE, Frédéric A., François GUDINCHET, Francis BRUNELLE, François O. BOCHUD, Francis R. VERDUN: Iterative reconstruction methods in two different MDCT scanners: physical metrics and 4-alternative forced-choice detectability experiments–a phantom approach. *Physica medica : PM : an international journal devoted to the applications of physics to medicine*

and biology : official journal of the Italian Association of Biomedical Physics (AIFB), jan 2013, Vol. 29, no. 1: pp. 99–110, ISSN 1724-191X.

[78] MORAES, Matheus Cardoso, Sergio Shiguemi FURUIE: Automatic Coronary Wall Segmentation in Intravascular Ultrasound Images Using Binary Morphological Reconstruction. *Ultrasound in Medicine and Biology*, 2011, Vol. 37, no. 9: pp. 1486–1499, ISSN 03015629.

[79] MORÉ, Jorge J.: The Levenberg-Marquardt algorithm: Implementation and theory. In *Numerical Analysis*, Springer Berlin Heidelberg, 1978, pp. 105–116.

[80] MORENO, Rodrigo, Magnus BORGA, Örjan SMEDBY: Estimation of trabecular thickness in gray-scale images through granulometric analysis. feb 2012: p. 831451.

[81] MOSCARIELLO, Antonio, Richard A. P. TAKX, U. Joseph SCHOEPF, Matthias RENKER, Peter L. ZWERNER, et al.: Coronary CT angiography: image quality, diagnostic accuracy, and potential for radiation dose reduction using a novel iterative image reconstruction technique-comparison with traditional filtered back projection. *European radiology*, oct 2011, Vol. 21, no. 10: pp. 2130–8, ISSN 1432-1084.

[82] MURPHY, K., B. VAN GINNEKEN, J. P. W. PLUIM, S. KLEIN, M. STARING: Semi-automatic reference standard construction for quantitative evaluation of lung CT registration. *Medical image computing and computer-assisted intervention : MICCAI ... International Conference on Medical Image Computing and Computer-Assisted Intervention*, 2008, Vol. 11, no. Pt 2: pp. 1006–13.

[83] NAGASHIMA, Sei, Takafumi AOKI, Tatsuo HIGUCHI, Koji KOBAYASHI: A Subpixel Image Matching Technique Using Phase-Only Correlation. In *2006 International Symposium on Intelligent Signal Processing and Communications*, IEEE, ISBN 0-7803-9732-0, pp. 701–704.

[84] NIEMANN, T., M. VAN STRATEN, C. RESINGER, T. BAYER, Georg BONGARTZ: Detection of urolithiasis using low-dose CT–a noise simulation study. *European journal of radiology*, nov 2011, Vol. 80, no. 2: pp. 213–8, ISSN 1872-7727.

[85] OTSU, Nobuyuki: A Threshold Selection Method from Gray-Level Histograms. *IEEE Transactions on Systems, Man and Cybernetics*, 1979, Vol. 9, no. 1: pp. 62–66.

[86] PLISSITI, Marina E., Christophoros NIKOU, Antonia CHARCHANTI: Automated detection of cell nuclei in pap smear images using morphological reconstruction and clustering. *IEEE transactions on information technology in biomedicine : a publication of the IEEE Engineering in Medicine and Biology Society*, 2011, Vol. 15, no. 2: pp. 233–241, ISSN 1558-0032.

[87] PONTANA, François, Julien PAGNIEZ, Thomas FLOHR, Jean-Baptiste FAIVRE, Alain DUHAMEL, et al.: Chest computed tomography using iterative reconstruction vs filtered back projection (Part 1): Evaluation of image noise reduction in 32 patients. *European radiology*, mar 2011, Vol. 21, no. 3: pp. 627–35, ISSN 1432-1084.

[88] POURREZA, Reza, Hamidreza POURREZA, Touka BANAEE: Segmentation of blood vessels in fundus color images by radon transform and morphological reconstruction. *3rd International Workshop on Advanced Computational Intelligence, IWACI 2010*, 2010: pp. 522–526.

[89] PRICE, W. L.: A controlled random search procedure for global optimisation. *The Computer Journal*, apr 1977, Vol. 20, no. 4: pp. 367–370, ISSN 0010-4620.

[90] PROTIK, Angjelina: Phantom study of the impact of adaptive statistical iterative reconstruction (ASiR) on image quality for paediatric computed tomography. *Journal of Biomedical Science and Engineering*, 2012, Vol. 05, no. 12: pp. 793–806, ISSN 1937-6871.

[91] PU, Jiantao, Carl FUHRMAN, Walter F. GOOD, Frank C. SCIURBA, David GUR: A differential geometric approach to automated segmentation of human airway tree. *IEEE Transactions on Medical Imaging*, 2011, Vol. 30, no. 2: pp. 266–278, ISSN 02780062, NIHMS150003.

[92] QIAO, Yuchuan, Baldur LEW, Boudewijn LELIEVELDT, Marius STARING: Fast Automatic Step Size Estimation for Gradient Descent Optimization of Image Registration. *IEEE transactions on medical imaging*, 2015, Vol. 35, no. 2: pp. 391–403, ISSN 1558-254X.

[93] RAMPADO, O., L. BOSSI, D. GARABELLO, O. DAVINI, R. ROPOLO: Characterization of a computed tomography iterative reconstruction algorithm by image quality evaluations with an anthropomorphic phantom. *European journal of radiology*, nov 2012, Vol. 81, no. 11: pp. 3172–7, ISSN 1872-7727.

[94] REN, Jinchang, Theodore VLACHOS, Jianmin JIANG: Subspace Extension to Phase Correlation Approach for Fast Image Registration. *2007 IEEE International Conference on Image Processing*, sep 2007, , no. 2: pp. I – 481–I – 484, ISSN 1522-4880.

[95] REN, Qingguo, Sheilesh Kumar DEWAN, Ming LI, Jianying LI, Dingbiao MAO, et al.: Comparison of adaptive statistical iterative and filtered back projection reconstruction techniques in brain CT. *European journal of radiology*, oct 2012, Vol. 81, no. 10: pp. 2597–601, ISSN 1872-7727.

[96] RIEDERER, S. J., N. J. PELC, D. A. CHESLER: The noise power spectrum in computed X-ray tomography. *Physics in medicine and biology*, may 1978, Vol. 23, no. 3: pp. 446–54, ISSN 0031-9155.

[97] RUECKERT, D., L. I. SONODA, C. HAYES, D. L. HILL, M. O. LEACH, et al.: Nonrigid registration using free-form deformations: application to breast MR images. *IEEE transactions on medical imaging*, aug 1999, Vol. 18, no. 8: pp. 712–21, ISSN 0278-0062.

[98] SIEWERDSEN, J. H., I. A. CUNNINGHAM, D. A. JAFFRAY: A framework for noise-power spectrum analysis of multidimensional images. *Medical Physics*, 2002, Vol. 29, no. 11: p. 2655, ISSN 00942405.

[99] SOILLE, Pierre: *Morphological image analysis*. Berlin: Springer Verlag, 2003, 391 pp., ISBN 3-540-42988-3.

[100] SOLOMON, Justin, Achille MILETO, Juan Carlos RAMIREZ GIRALDO, Ehsan SAMEI: Diagnostic Performance of an Advanced Modeled Iterative Reconstruction Algorithm for Multidetector CT Scanner : Potential for Radiation Dose Reduction in a Multireader Study 1. *Radiology*, 2015, Vol. 275, no. 3: pp. 735–745, ISSN 0033-8419.

[101] SOLOMON, Justin, Ehsan SAMEI: Are uniform phantoms sufficient to characterize the performance of iterative reconstruction in CT? *Medical Imaging 2013: Physics of Medical Imaging, edited by Robert M. Nishikawa, Bruce R. Whiting, Christoph Hoeschen, Proc. of SPIE Vol. 8668, 86684M*, 2013, Vol. 8668, no. March: pp. 86684M–86684M–6, ISSN 16057422.

[102] SOLOMON, Justin, Ehsan SAMEI: Quantum noise properties of CT images with anatomical textured backgrounds across reconstruction algorithms: FBP and SAFIRE. *Medical Physics*, aug 2014, Vol. 41, no. 9: p. 091908, ISSN 00942405.

[103] STARING, Marius, Stefan KLEIN, Johan H. C. REIBER, Wiro J. NIESSEN, Berend C. STOEL: Pulmonary Image Registration with elastix using a Standard Intensity-Based Algorithm. *MICCAI2010 Workshop: Medical Image Analysis For The Clinic - A Grand Challenge*, 2010: pp. 73–79.

[104] STEGER, Sebastian, Matthias KIRSCHNER, Stefan WESARG: Articulated atlas for segmentation of the skeleton from head & neck CT datasets. In *2012 9th IEEE International Symposium on Biomedical Imaging (ISBI)*, IEEE, ISBN 978-1-4577-1858-8, pp. 1256–1259.

[105] SU, Ran, Changming SUN, Chao ZHANG, Tuan D. PHAM: A new method for linear feature and junction enhancement in 2D images based on morphological operation, oriented anisotropic Gaussian function and Hessian information. *Pattern Recognition*, 2014, Vol. 47, no. 10: pp. 3193–3208, ISSN 00313203.

[106] SUI, Xin, Felix G. MEINEL, Wei SONG, Xiaoli XU, Zixing WANG, et al.: Detection and size measurements of pulmonary nodules in ultra-low-dose CT with iterative reconstruction compared to low dose CT. *European Journal of Radiology*, 2016, Vol. 85, no. 3: pp. 564–570, ISSN 18727727.

[107] SUZUKI, Shigeru, Haruhiko MACHIDA, Isao TANAKA, Eiko UENO: Measurement of vascular wall attenuation: comparison of CT angiography using model-based iterative reconstruction with standard filtered back-projection algorithm CT in vitro. *European journal of radiology*, nov 2012, Vol. 81, no. 11: pp. 3348–53, ISSN 1872-7727.

[108] TAKITA, Kenji, Takafumi AOKI, Yoshifumi SASAKI, Tatsuo HIGUCHI, Koji KOBAYASHI: High-Accuracy Subpixel Image Registration Based on Phase-Only Correlation. *IEICE TRANSACTIONS on Fundamentals of Electronics, Communications and Computer Sciences*, 2003, , no. 8: pp. 1925–1934.

[109] TRUC, Phan T.H., Tae Seong KIM, Sungyoung LEE, Young Koo LEE: A study on the feasibility of active contours on automatic CT bone segmentation. *Journal of Digital Imaging*, 2010, Vol. 23, no. 6: pp. 793–805, ISSN 08971889.

[110] TSCHIRREN, Juerg, Eric A. HUFFMAN, Geoffrey MCLENNAN, Milan SONKA: Intrathoracic airway trees: Segmentation and airway morphology analysis from low-dose CT scans. *IEEE Transactions on Medical Imaging*, 2005, Vol. 24, no. 12: pp. 1529–1539, ISSN 02780062, NIHMS150003.

[111] VINCENT, L.: Morphological grayscale reconstruction in image analysis: Applications and efficient algorithms. *IEEE Transactions on Image Processing*, 1993, Vol. 2, no. 2: pp. 633–635, ISSN 1057-7149.

[112] WALEK, Petr, Jiri JAN: Segmentation of basic tissues for assessing noise in iteratively reconstructed MDCT data. In *Advances in Sensors, Signals, Visualization, Imaging and Simulation*, WSEAS Press, ISBN 9781618041197, pp. 211–216.

[113] WALEK, Petr, Jiri JAN, Petr OUREDNICEK, Jarmila SKOTAKOVA, Igor JIRA: Preprocessing for Quantitative Statistical Noise Analysis of MDCT Brain Images Reconstructed Using Hybrid Iterative (iDose) Algorithm. In *Journal of WSCG*, Vol. 20, Pilsen, pp. 73–80.

[114] WANG, Liping Ingrid, Michael GREENSPAN, Randy ELLIS: Validation of bone segmentation and improved 3-D registration using contour coherency in CT data. *IEEE transactions on medical imaging*, mar 2006, Vol. 25, no. 3: pp. 324–34, ISSN 0278-0062.

[115] WANG, Zhaoyang, Jun MA, Minh VO: Recent progress in two-dimensional continuous wavelet transform technique for fringe pattern analysis. *Optics and Lasers in Engineering*, 2012, Vol. 50, no. 8: pp. 1052–1058, ISSN 01438166.

[116] WELCH, P.: The use of fast Fourier transform for the estimation of power spectra: A method based on time averaging over short, modified periodograms. *IEEE Transactions on Audio and Electroacoustics*, jun 1967, Vol. 15, no. 2: pp. 70–73, ISSN 0018-9278.

[117] WILLEMINK, Martin J., Pim A. DE JONG, Tim LEINER, Linda M. DE HEER, Rutger A.J. NIEVELSTEIN, et al.: Iterative reconstruction techniques for computed tomography Part 1: Technical principles. *European Radiology*, 2013, Vol. 23, no. 6: pp. 1623–1631, ISSN 09387994.

[118] WINKLEHNER, Anna, Christoph KARLO, Gilbert PUIPPE, Bernhard SCHMIDT, Thomas FLOHR, et al.: Raw data-based iterative reconstruction in body CTA: evaluation of radiation dose saving potential. *European radiology*, dec 2011, Vol. 21, no. 12: pp. 2521–6, ISSN 1432-1084.

[119] WU, Jie, Pavani DAVULURI, Kevin WARD, Charles COCKRELL, Rosalyn HOBSON, et al.: A new hierarchical method for multi-level segmentation of bone in pelvic CT scans. *Proceedings of the Annual International Conference of the IEEE Engineering in Medicine and Biology Society, EMBS*, 2011: pp. 3399–3402, ISSN 1557170X.

[120] XU, Ziyue, Ulas BAGCI, Brent FOSTER, Awais MANSOOR, Jayaram K. UDUPA, et al.: A hybrid method for airway segmentation and automated

measurement of bronchial wall thickness on CT. *Medical Image Analysis*, aug 2015, Vol. 24, no. 1: pp. 1–17, ISSN 13618415, 15334406.

[121] YANG, Kai, Alexander L. C. KWAN, Shih-Ying HUANG, Nathan J. PACKARD, John M. BOONE: Noise power properties of a cone-beam CT system for breast cancer detection. *Medical Physics*, 2008, Vol. 35, no. 12: p. 5317, ISSN 00942405.

[122] YANG, Young Jun, Sun Hong KWON, Seung Geun PARK, Jun Soo PARK: Remote sensing of wave directionality by two-dimensional directional wavelets: Part 1. the detection tools of directionality in signals. *Brodogradnja*, 2014, Vol. 65, no. 3: pp. 1–15, ISSN 0007215X.

[123] YAO, W., P. ABOLMAESUMI, M. GREENSPAN, R. E. ELLIS: An estimation/correction algorithm for detecting bone edges in CT images. *IEEE transactions on medical imaging*, aug 2005, Vol. 24, no. 8: pp. 997–1010, ISSN 0278-0062.

[124] YAZDI, Mehran, Luc BEAULIEU: Artifacts in Spiral X-ray CT Scanners : Problems and Solutions. *World Academy of Science, Engineering and Technology*, 2007, Vol. 11, no. 11: pp. 96–100, ISSN 20103840.

[125] ZHANG, Dengsheng, Guojun LU: Study and evaluation of different Fourier methods for image retrieval. *Image and Vision Computing*, 2005, Vol. 23, no. 1: pp. 33–49, ISSN 02628856.

[126] ZHANG, J., C. H. YAN, C. K. CHUI, S. H. ONG: Fast segmentation of bone in CT images using 3D adaptive thresholding. *Computers in Biology and Medicine*, 2010, Vol. 40, no. 2: pp. 231–236, ISSN 00104825.

[127] ZIZKA, Jan: Iterative reconstruction of CT image - A revolutionary milestone in computed tomography? *Czech Radiology*, 2011, Vol. 65, no. 3: pp. 169–176.